INFORMATION TO USERS

This manuscript has been reproduced from the microfilm master. UMI films the text directly from the original or copy submitted. Thus, some thesis and dissertation copies are in typewriter face, while others may be from any type of computer printer.

The quality of this reproduction is dependent upon the quality of the copy submitted. Broken or indistinct print, colored or poor quality illustrations and photographs, print bleedthrough, substandard margins, and improper alignment can adversely affect reproduction.

In the unlikely event that the author did not send UMI a complete manuscript and there are missing pages, these will be noted. Also, if unauthorized copyright material had to be removed, a note will indicate the deletion.

Oversize materials (e.g., maps, drawings, charts) are reproduced by sectioning the original, beginning at the upper left-hand corner and continuing from left to right in equal sections with small overlaps.

Photographs included in the original manuscript have been reproduced xerographically in this copy. Higher quality 6" x 9" black and white photographic prints are available for any photographs or illustrations appearing in this copy for an additional charge. Contact UMI directly to order.

Bell & Howell Information and Learning
300 North Zeeb Road, Ann Arbor, MI 48106-1346 USA
800-521-0600

THEORETICAL MODELING OF LARGE-SCALE ELECTROMAGNETIC PROBLEMS USING A HYBRID MoM/FEM METHOD, WAVELETS, AND HIGH-PERFORMANCE COMPUTING

by

Donghoon Chun

A dissertation submitted in partial fulfillment
of the requirements for the degree of
Doctor of Philosophy
(Electrical Engineering)
in The University of Michigan
2000

Doctoral Committee:

Professor Linda P. B. Katehi, Chair
Professor Edward S. Davidson
Professor Tony England
Associate Professor Kamal Sarabandi
Rainee Simons, Senior Engineer, NASA

This thesis is dedicated to my father and mother, my wife Haeshin,
my daughter Yujin, my son Minjoon,
and my brother Dongyell.
For their sacrifice, encouragement, and great love.

ACKNOWLEDGEMENTS

In the end of this long journey, many people come to mind who have helped me to complete my doctoral study and this dissertation successfully. I wish to remember all those people and to share this success with them in these acknowledgements.

First and foremost, I greatly appreciate my advisor, Professor Linda Katehi, for recognizing my potential and helping me to realize that potential throughout my graduate study. Her passion toward the research and her broad and deep technical experience have significantly contributed to this work. In addition, her encouragement, endurance, and understanding have enabled me to overcome all the difficulties I have faced during the past five years and to successfully proceed with my research.

I thank my committee members for their support and time: Professor Edward Davidson for his guidance on the chapter of high performance computing, Professor Kamal Sarabandi for technical discussions on the application of wavelet theory, Professor Tony England for his interest and suggestions on my dissertation, and Dr. Rainee Simons for his pleasant collaboration during the research on high-frequency antenna design.

Since my research was a continuation of Dr. Jui-Ching Cheng's work, I would like to thank him for helping me to understand his previous work and for his valuable technical advice. Dr. George Ponchak at NASA's Glenn Research Center and Dr. Jong-Gwan Yook have to be recognized for their encouragement and assistance during the packaging study.

My gratitude also goes to Professor Jeong-Ki Pack who introduced me to the electromagnetic area for the first time and advised me to pursue a doctoral degree in this wonderful university. I always thank his warm-hearted humanity he has always shown to me.

I owe many Rad Lab friends useful comments on my dissertation: Mark Fischman, James Becker, Kevin Buell, Sarris Konstantinos, Lee Harle, Bill Chappell, and Ron Reano. I thank all Rad Lab and KEECS friends including previous members for their friendship and good time; their names are too many to mention in this short page.

The army Research Lab (ARL) had sponsored me for almost five years. I appreciate their support and interest in my research.

No words can express my gratitude to the members of my wife's family for their inspiration and support, which I will never forget. I would like to give my sincere appreciation to them by listing all their names in this limited space: Dr. Jaesoo Park, Haesung Park, Dr. Sangwook Park, Dr. Youngju Chun, Hyungsaek Park, Jaeyeon Park, Haejun Park, Chisang Ji, and Yunsae Ji. I also wish to share the joy of completing this study with my mother-in-law who made her best wishes and watches me in the glory of God all of the time.

Even a single achievement or success in my entire career can not be described without mentioning my parent. I do acknowledge all of their enormous time and effort dedicated toward raising me and nurturing my abilities. I wish this small accomplishment can partially return their devotion and endless love I have received during all of the years of my life. My trustful brother, Dongyell, deserves my special thanks for always believing in my success and taking care of my parents and family matters while I am away from home. I thank the family members of my sister

for supporting me during my graduate years: Jungrean Chun. Taeyong Gwak, and Soyoung Gwak.

Finally, I would like to express my deep appreciation to my beloved wife, Haeshin, for her unfailing love, trustfulness, and sacrifice on my behalf. She has been the source of my strength with which I can survive all challenges I have to face everyday. I thank her for enriching my life with the greatest joy and happiness of being the father of a lovely daughter, Yujin, and a sweet little son, Minjoon.

I truly believe it will be remembered as one of the greatest moments in my life.

TABLE OF CONTENTS

LIST OF FIGURES

Figure

LIST OF TABLES

Table

LIST OF APPENDICES

Appendix

CHAPTER I

INTRODUCTION

1.1 Motivation and Objectives

The development of high-frequency MMICs (monolithic microwave integrated circuits) has been driven by the demands for portability and increased functional efficiency of wireless communication systems. In advanced communication systems, MMICs are required to include a large number of circuit components, lines and interconnections between circuits in a compact space. The complexity imposed by these large numbers of components and connections is extremely challenging for the design of efficient simulators that are necessary tools for MMIC development. Because of the large amount of memory and long computation time required, conventional computational methods prove to be insufficient means of addressing certain types of problems. The goal of the study reported here is to formulate a practical way of numerical modeling and characterization of such complex and large-scale electromagnetic circuits.

A number of full-wave frequency and time domain methods have been developed based on the integral and partial differential representation of Maxwell's equations. They are: the Method of Moments (MoM), the Finite Element Method (FEM), and the Finite Difference Time Domain (FD-TD) method.

MoM [1] is a frequency domain technique, which uses a Green's function-based integral formulation for the solution of Maxwell's equations. Due to the use of Green's function, MoM is the most preferred and efficient method of the three. However, the analytic effort to derive the complete Green's function proves to be a very difficult task for a large complex circuit geometry. It needs a long computation time and significant memory resources to solve large-scale electromagnetic problems. For this reason, MoM is limited to problems of a moderate size and complexity.

As a computer aided analysis and design technique, FEM [2, 3] has been employed in several areas of engineering. In electromagnetic field computation, FEM discretizes the differential form of wave equation in the frequency domain and solves the equation without a priori analytic effort. Hence, FEM is particularly suitable for arbitrarily shaped electromagnetic problems: a definite advantage over MoM. The application of the FEM does, however, lead to a large linear system that has to be solved and unfortunately needs large amounts of memory and high computation time. Moreover, in open boundary problems, the incorporation of absorbing boundary conditions (ABCs) or artificial absorbers in the FEM often proves to be a source of numerical inaccuracy for the method.

Unlike the previous two methods, the FD-TD technique [4, 5] solves the time-domain Maxwell's equations, which makes it simple and easy to formulate the system equation. Furthermore, FD-TD can be applied to arbitrarily inhomogeneous geometries, just as FEM does. The main advantage of FD-TD, which clearly is its simplicity in implementation, is obtained at the expense of computational resources and execution time. However, this technique provides a wideband characterization of the simulated structure, since Fourier-transforming the time domain data provides frequency domain quantities over a typically large bandwidth. Nevertheless, it is

important to point out that the transformation itself can introduce numerical errors. Implementation of open boundary conditions again constitutes one more source of inaccuracy.

As mentioned previously, MoM is an efficient method but requires analytical effort to derive a complete Green's function, which is a very difficult task for complex geometries, making this method impractical. Unlike MoM, FEM can be applied to an arbitrarily shaped structure without the need for a Green's function, but requires large amounts of memory and high computational time. While FD-TD has demonstrated its ease in implementation for any shape of geometry, it demands similar computational resources when compared with FEM. All three methods need significantly large computational resources for the extraction of accurate and convergent solutions. To circumvent the existing theoretical obstacles and the limitation of computational resources for the treatment of large-scale electromagnetic problems, the author has developed the hybrid MoM/FEM method and introduced the use of multiresolution analysis (MRA) and high-performance computing (HPC).

The hybrid MoM/FEM method [6, 7] aims for combining the advantages of MoM and FEM. In this method, FEM is applied in modeling the complex geometries and inhomogeneous materials in one domain, while MoM is implemented in the open space radiation domain using the available Green's function. By doing so, we can reduce the heavy computational load and avoid the analytical difficulties of deriving the required Green's functions.

The application of MRA theory [8, 9, 10] in the hybrid MoM/FEM technique enhances the overall computational efficiency of the hybrid MoM/FEM linear system. Since MRA diagonalizes the hybrid linear system, we can achieve highly sparse matrices by discarding small, off-diagonal terms. This threshold process can occur

without significantly affecting the solution. As a result, we can significantly reduce memory requirement and achieve short computational time. Furthermore, we can employ adaptive discretization schemes in computation domains.

Parallel computing [11, 12] is an efficient alternative for addressing the need for large computational resources, often arising in complex electromagnetic problems related to state of the art microwave applications. To achieve maximum performance improvement in parallel computing, an effective parallelization scheme has to be deployed for each computation step of the hybrid MoM/FEM method. Task parallelization and domain decomposition are important parallelization schemes which can be directly implemented in this numerical calculation. In the hybrid method, FEM has to be applied repeatedly for different frequencies and excitations. Therefore, parallel task computation is an efficient method when the required size of memory for the FEM calculation does not exceed the allocated memory size of a single processor. The FEM computation, though, requires not only task parallelization but also domain decomposition. In the latter method, several processors are used to store and solve a large FEM linear system. The task parallelization scheme can also be utilized in MoM calculation where a sequence of numerical integrations is the dominant process. In particular, MoM numerical integration tasks can be divided among processors and performed in each processor independently.

In the last stage of this numerical method, the matrix decomposition method can be used to solve the large hybrid linear system when it becomes too large to be stored in a single processor. It is a critical part of parallel computing to measure its efficiency in terms of scalability and determine the size of the problem that can be solved.

The final two stages of this research first verified the hybrid MoM/FEM method

and then applied it to an antenna array structure. By solving a single aperture-coupled patch antenna and comparing the computed results with the published measurement data, the hybrid MoM/FEM method was validated along with the integration of multi-resolution analysis. Finally, the hybrid MoM/FEM method, MRA theory, and HPC were employed for the solution of an antenna array structure.

CHAPTER II

HYBRID METHOD OF MOMENT (MoM) / FINITE ELEMENT METHOD (FEM)

A basic theory of a hybrid MoM/FEM method is presented in this chapter, with a specific focus on electromagnetic scattering problems involving aperture-coupled geometries (for example, aperture-coupled patch antennas). After providing a brief background of this method, we describe the formulation of hybrid MoM/FEM equations, including the combining process of MoM and FEM solutions.

2.1 Background

Hybrid methods were developed in the early 1970's by Mei [13], Silvester [14], and McDonald [15] to solve unbounded problems involving localized inhomogeneous media. Their basic concept was to utilize the advantages of two methods: (1) a partial differential-equation method, such as FEM, in localized inhomogeneous or anisotropic regions, where the integral equation method is disadvantageous; (2) an integral equation method in the remaining unbounded region utilizing simple free-space Green's function. By doing so, they could solve the problems after combining local solutions using boundary conditions between regions. This idea of hybridization soon became popular in the electromagnetic computational community because we can independently choose an efficient computation method for each sub-divided

computational domain. The hybrid method has been used frequently in various types of electromagnetic problems, such as scattering problems [16]-[20], the characterization of microwave circuits [21, 22], and printed circuit boards (PCBs) [23], whose solutions are difficult or very costly to perform with a single computational method.

The hybridization of FEM and integral equation method has been implemented in two different ways: (1) Finite Element - Boundary Integral (FE-BI) method; (2) hybrid Method of Moment and Finite Element Method (MoM/FEM) technique. Both methods share the same hybridization idea that has been mentioned earlier, but the way of configuring the problem is different when they are applied in electromagnetic scattering/radiation problems. In FE-BI method, all scatterers/radiators are included in FEM domain along the boundary between FEM and boundary integral regions such that only the scattered or radiated electromagnetic field is considered in boundary integral regions to satisfy the Sommerfeld radiation condition. In addition, in the boundary of two regions, the existing FE-BI method shares the same bases for both FEM and boundary integral computations to model and interpolate the electromagnetic field in this boundary. Unlike FE-BI method, hybrid MoM/FEM technique not only can include scatterers/radiators in MoM domain but also allows the use of different bases in MoM and FEM computations at the boundary of two regions. With these features in hybrid MoM/FEM technique, we can reduce FEM domain and further utilize the available Green's function in scatterers/radiators. Moreover, various types of basis function (such as roof-top scaling functions and wavelets) can be employed in scatterers/radiators and the boundary region in MoM computation, while we can utilize other basis functions (such as node basis or edge vector basis function) in FEM domain including the boundary of FEM and MoM domains for FEM computation. For this reason, hybrid MoM/FEM technique proves to be more

efficient in electromagnetic scattering/radiation problems that involve multi-layered MMICs/antenna structure. Most importantly, only hybrid MoM/FEM technique can incorporate Multi-Resolution Analysis (MRA) theory in that any type of basis function can be employed in MoM domain that we will discuss in later chapters.

2.2 Method of Moment (MoM)

Consider an electromagnetic scattering problem shown in Fig. 2.1(a). An electromagnetic field is excited by a source in domain Ω_2 and coupled to domain Ω_1 through an aperture printed on a perfect electric conductor (PEC). The coupled electromagnetic field is finally scattered by an PEC scatterer in domain Ω_1. To apply hybrid MoM/FEM method to this problem, we first bound the domain Ω_2 by some combination of PEC, perfect magnetic conductor (PMC), and absorbing boundary condition (ABC) while we leave the domain Ω_1 unbounded. Using the equivalence principle [24], the problem can be redefined as in Fig. 2.1(b): (1) the aperture is closed with the PEC; (2) an equivalent magnetic current is inserted just above and under the PEC; (3) the scatterer is replaced by a fictitious surface electric current. With this newly defined problem, we formulate a hybrid MoM/FEM equation. The total electromagnetic field in Ω_1 is generated by a fictitious electric current, $\overline{J}^b$, and an equivalent magnetic current, $-\overline{M}_s$. Therefore,

$$\overline{E}^1 = \overline{E}^1(\overline{J}^b) + \overline{E}^1(-\overline{M}_s) \tag{2.1}$$

$$\overline{H}^1 = \overline{H}^1(\overline{J}^b) + \overline{H}^1(-\overline{M}_s) \tag{2.2}$$

Similarly, the total electromagnetic field in Ω_2 can be expressed as

$$\overline{E}^2 = \overline{E}^2(\overline{M}_s) + \overline{E}^2(\overline{M}_f) \tag{2.3}$$

$$\overline{H}^2 = \overline{H}^2(\overline{M}_s) + \overline{H}^2(\overline{M}_f) \tag{2.4}$$

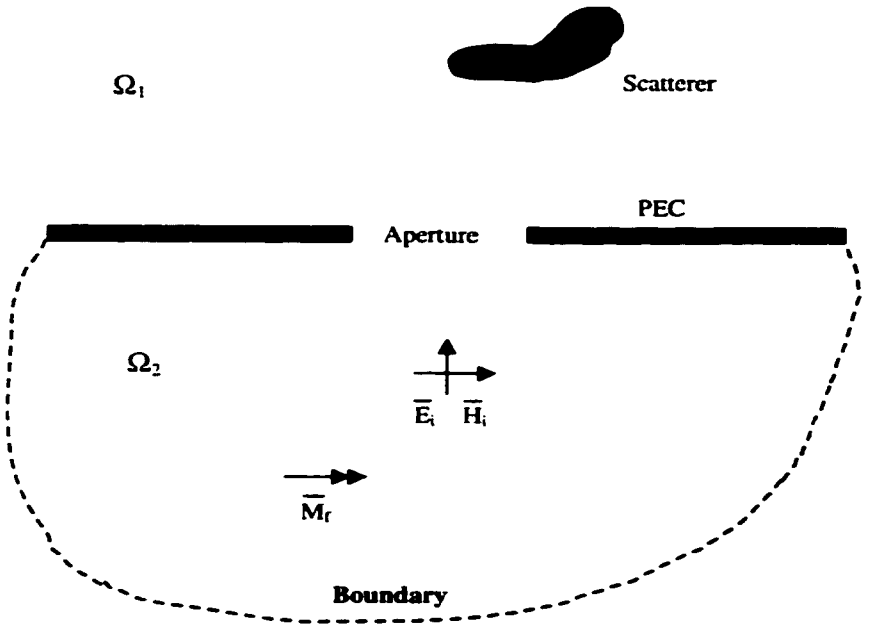

(a)

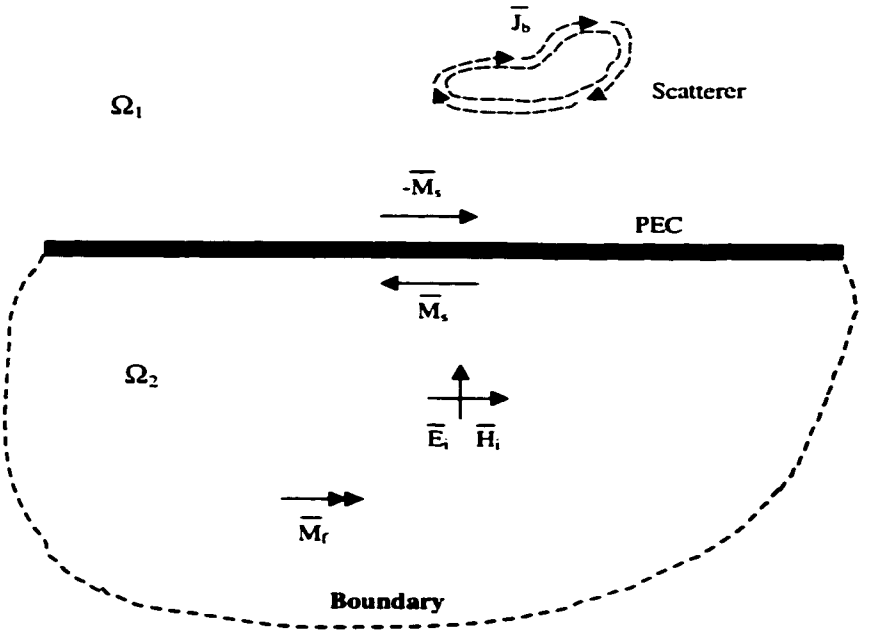

(b)

Figure 2.1: (a) Original Problem (b) Equivalent Problem. The boundary of domain Ω_2 is closed by some combination of PEC, PMC, and ABC

The electromagnetic fields in two separate domains can be coupled through the boundary conditions imposed on the aperture and the PEC scatterer: (1) the tangential magnetic field is continuous through the aperture; (2) the tangential electric field vanishes on the surface of the PEC scatterer.

$$\hat{n} \times \overline{H}^1 = \hat{n} \times \overline{H}^2 \tag{2.5}$$

$$\hat{n} \times \overline{E}^1 = 0 \tag{2.6}$$

By substituting Eqs. (2.1) – (2.4) into Eqs. (2.5) – (2.6), we can obtain the following coupled equations.

$$\overline{H}_t^1(\overline{J}^b) + \overline{H}_t^1(-\overline{M}_s) = \overline{H}_t^2(\overline{M}_s) + \overline{H}_t^2(\overline{M}_f) \tag{2.7}$$

$$\overline{E}_t^1(\overline{J}^b) + \overline{E}_t^1(-\overline{M}_s) = 0 \tag{2.8}$$

The unknowns in this problem are the equivalent magnetic currents, $\overline{M}_s$, over the aperture and the fictitious electric current, $\overline{J}^b$, on the PEC scatterer. Thus, we expand the unknown magnetic and electric currents as

$$\overline{M}_s^a = \sum_{n=1}^{N_a} m^a{}_n \overline{M}^a{}_n \tag{2.9}$$

$$\overline{J}^b = \sum_{n=1}^{N_b} j^b{}_n \overline{J}^b{}_n \tag{2.10}$$

where $\overline{M}^a{}_n$ and $\overline{J}^b{}_n$ are basis functions, $m^a{}_n$ and $j^b{}_n$ are unknown coefficients, N_a is the number of basis $\overline{M}^a{}_n$, and N_b is the number of basis $\overline{J}^b{}_n$.

Now, Galerkin's moment method [1] is applied to Eqs. (2.7) – (2.8) with the expansions in Eqs. (2.9) – (2.10) and the inner product defined as

$$(\overline{A}, \overline{B})_s = \int\int_s \overline{A} \cdot \overline{B}\, dS \tag{2.11}$$

The resulting equations are expressed by

$$(\overline{M}^a_m, \overline{H}^1_t(\overline{J}^b_n))[J^b] + (\overline{M}^a_m, \overline{H}^1_t(-\overline{M}^a_n))[M^a] = (\overline{M}^a_m, \overline{H}^2_t(\overline{M}^a_n))[M^a] + (\overline{M}^a_m, \overline{H}^2_t(\overline{M}_f)) \tag{2.12}$$

$$(\overline{J}^b_m, \overline{E}^1_t(\overline{J}^b_n))[J^b] + (\overline{J}^b_m, \overline{E}^1_t(-\overline{M}^a_n))[M^a] = 0 \tag{2.13}$$

Using the following notations,

$$y^a_{mn} = (-\overline{M}^a_m, \overline{H}^1_t(\overline{M}^a_n)) \quad \mathrm{N}_a \times \mathrm{N}_a \text{ matrix} \tag{2.14}$$

$$z^b_{mn} = (-\overline{J}^b_m, \overline{E}^1_t(\overline{J}^b_n)) \quad \mathrm{N}_b \times \mathrm{N}_b \text{ matrix} \tag{2.15}$$

$$t^b_{mn} = (\overline{J}^b_m, \overline{E}^1_t(\overline{M}^a_n)) \quad \mathrm{N}_b \times \mathrm{N}_a \text{ matrix} \tag{2.16}$$

$$c^b_{mn} = (\overline{M}^a_m, \overline{H}^1_t(\overline{J}^b_n)) \quad \mathrm{N}_a \times \mathrm{N}_b \text{ matrix} \tag{2.17}$$

$$y^c_{mn} = (-\overline{M}^a_m, \overline{H}^2_t(\overline{M}^a_n)) \quad \mathrm{N}_a \times \mathrm{N}_a \text{ matrix} \tag{2.18}$$

$$V_{inc,m} = (-\overline{M}^a_m, \overline{H}^2_t(\overline{M}_f)) \quad \mathrm{N}_a \times 1 \text{ column vector} \tag{2.19}$$

Eqs. (2.12) – (2.13) can be simply written as

$$[C^b][J^b] + [Y^a][M^a] = -[Y^c][M^a] - [V_{inc}] \tag{2.20}$$

$$-[Z^b][J^b] - [T^b][M^a] = 0 \tag{2.21}$$

Finally, the unknown coefficients of the magnetic and electric currents can be solved as

$$[M^a] = \frac{[V_{inc}]}{[C^b][Z^b]^{-1}[T^b] - [Y^a] - [Y^c]} \tag{2.22}$$

$$[J^b] = -[Z^b]^{-1}[T^b][M^a] \tag{2.23}$$

For large-scale problems, however, the size of the sub-matrices in Eqs. (2.21) – (2.22) become so large that the equations (Eqs. (2.21) – (2.22)) cannot be solved with the

direct inversion method. Therefore, we solve the following form of the linear equation with iterative and domain decomposition methods instead.

$$\begin{bmatrix} [Z^b] & [T^b] \\ [C^b] & [Y^a]+[Y^b] \end{bmatrix} \begin{bmatrix} [J^b] \\ [M^a] \end{bmatrix} = \begin{bmatrix} 0 \\ -[V_{inc}] \end{bmatrix} \tag{2.24}$$

The sub-matrices $[Y^a]$, $[Z^b]$, $[T^b]$, and $[C^b]$ contain information about the fields generated by the electric and magnetic currents in domain Ω_1, which can be calculated using the available Green's function. On the other hand, $[Y^c]$ and $[V_{inc}]$ concern field characteristics in domain Ω_2, where the required Green's function is not available or is difficult to derive. Thus, we apply FEM in domain Ω_2 to obtain the necessary sub-matrices. Detailed FEM computational procedures are provided in the following sections.

2.3 Finite Element Method (FEM)

In this section, we present the finite element method to obtain the sub-matrices, $[Y^c]$ and $[V_{inc}]$, in domain Ω_2.

The time-harmonic electromagnetic fields in Ω_2 are characterized by Maxwell's equations

$$\nabla \times \overline{E} = -j\omega\overline{B} - \overline{M} \tag{2.25}$$

$$\nabla \times \overline{H} = j\omega\overline{D} + \overline{J} \tag{2.26}$$

$$\nabla \cdot \overline{D} = \rho_e \tag{2.27}$$

$$\nabla \cdot \overline{B} = \rho_m \tag{2.28}$$

and the appropriate constitutive relations

$$\overline{D} = \epsilon\overline{E} \tag{2.29}$$

$$\overline{B} = \mu\overline{H} \tag{2.30}$$

where

$\overline{E}$: electric field [V/m]

$\overline{H}$: magnetic field [A/m]

$\overline{D}$: electric flux density [C/m^2]

$\overline{D}$: magnetic flux density [Weber/m^2]

$\overline{M}$: impressed magnetic current [V/m^2]

$\overline{J}$: impressed electric current [A/m^2]

ρ_e : electric charge density [C/m^3]

ρ_m : magnetic charge density [Weber/m^3]

ω : angular frequency [rad/sec]

ϵ : permittivity [F/m]

μ : permeability [H/m]

The wave equation for the magnetic field, $\overline{H}_2$, in domain Ω_2 can be obtained from Eqs. (2.25) – (2.26) with the aid of the constitutive relations in Eqs. (2.29) – (2.30).

$$\nabla \times (-\frac{1}{j\omega\epsilon_2}\nabla \times \overline{H}_2) = j\omega\mu_2\overline{H}_2 + \overline{M} \tag{2.31}$$

Now, the wave equation is discretized with vector edge bases in a tetrahedral element (Fig. 2.2). By doing so, we can approximate the electromagnetic field as

$$\overline{H}_2 = \sum_{i=1}^{N_\phi} \phi_{ij}\overline{\phi}_i \tag{2.32}$$

where $\overline{\phi}_i$ and ϕ_{ij} are the vector edge basis and the coefficient of the basis, respectively. In this stage, ϕ_{ij} is the unknown element for which FEM will eventually solve. Applying Galerkin's method with the expansion in Eq. (2.32), Eq. (2.31) is discretized as

$$\sum_{i=1}^{N_\phi} \phi_{ij}\langle \nabla \times (-\frac{1}{j\omega\epsilon_2}\nabla \times \overline{\phi}_i) - j\omega\mu_2\overline{\phi}_i, \overline{\phi}\rangle = \int_s \overline{M} \cdot \overline{\phi}\, dS \tag{2.33}$$

where the inner product $\langle \overline{A}, \overline{B}\rangle$ is defined as follows:

$$\langle \overline{A}, \overline{B}\rangle = \int\int_v\int \overline{A} \cdot \overline{B}\, dv \tag{2.34}$$

Equation (2.33) can be reformulated with Green's identity as

$$\sum_{i=1}^{N_\phi} \phi_{ij}\{\langle \frac{1}{\omega\epsilon_2}\nabla \times \overline{\phi}_i, \nabla \times \overline{\phi}\rangle - \langle \omega\mu_2\overline{\phi}_i, \overline{\phi}\rangle\} = -j\int_s \overline{M} \cdot \overline{\phi}\, dS \tag{2.35}$$

Therefore, we obtain the following simple linear equation:

$$[A][\Phi] = [B] \tag{2.36}$$

where the elements of the matrices are given as

$$a_{ij} = \langle \frac{1}{\omega\epsilon_2}\nabla \times \overline{\phi}_i, \nabla \times \overline{\phi}_j \rangle - \langle \omega\mu_2 \overline{\phi}_i, \overline{\phi}_j \rangle \quad \mathrm{N}_\phi \times \mathrm{N}_\phi \text{ matrix} \tag{2.37}$$

$$b_{ij} = -j \int_s \overline{M}_j^a \cdot \overline{\phi}_i \, dS \quad \mathrm{N}_\phi \times \mathrm{N}_a \text{ matrix} \tag{2.38}$$

$$\Phi_{ij} = \phi_{ij} \quad \mathrm{N}_\phi \times \mathrm{N}_a \text{ matrix} \tag{2.39}$$

Another form of Eq. (2.37) can be given in terms of the nodes and vectors associated with the edge bases in a tetrahedral element (Fig. 2.2) [25]:

$$\begin{aligned} a_{ij} &= \langle \frac{1}{\omega\epsilon_2}\nabla \times \overline{\phi}_i, \nabla \times \overline{\phi}_j \rangle - \langle \omega\mu_2 \overline{\phi}_i, \overline{\phi}_j \rangle \\ &= \frac{4}{\omega\epsilon_2}\Omega_2(\overline{g_i} \cdot \overline{g_j}) - \omega\mu_2(P_1 + P_2 + P_3) \end{aligned}$$

where

$$\overline{\phi}^e_{7-i} = \begin{cases} \overline{f}_{7-i} + \overline{g}_{7-i} \times \overline{r} & \overline{r} \in \Omega_e \\ 0 & \overline{r} \notin \Omega_e \end{cases}$$

$$\overline{f}_{7-i} = \frac{c_{7-i}}{6\Omega_e}\overline{r}_{i1} \times \overline{r}_{i2}$$

$$\overline{g}_{7-i} = \frac{c_i c_{7-i}}{6\Omega_e}\overline{e}_i$$

$$\overline{e}_i = \frac{\overline{r}_{i2} - \overline{r}_{i1}}{c_i}$$

$$c_i = |\overline{r}_{i2} - \overline{r}_{i1}|, \quad \text{for } i = 1 \sim 6$$

$$\Omega_e = \text{volume of an element.}$$

$$P_1 = \langle \overline{f}_i, \overline{f}_j \rangle$$

$$P_2 = \langle \overline{f}_i, \overline{g}_j \times \overline{r} \rangle + \langle \overline{g}_i \times \overline{r}, \overline{f}_j \rangle$$

$$P_3 = \langle \overline{g}_i \times \overline{r}, \overline{g}_j \times \overline{r} \rangle$$

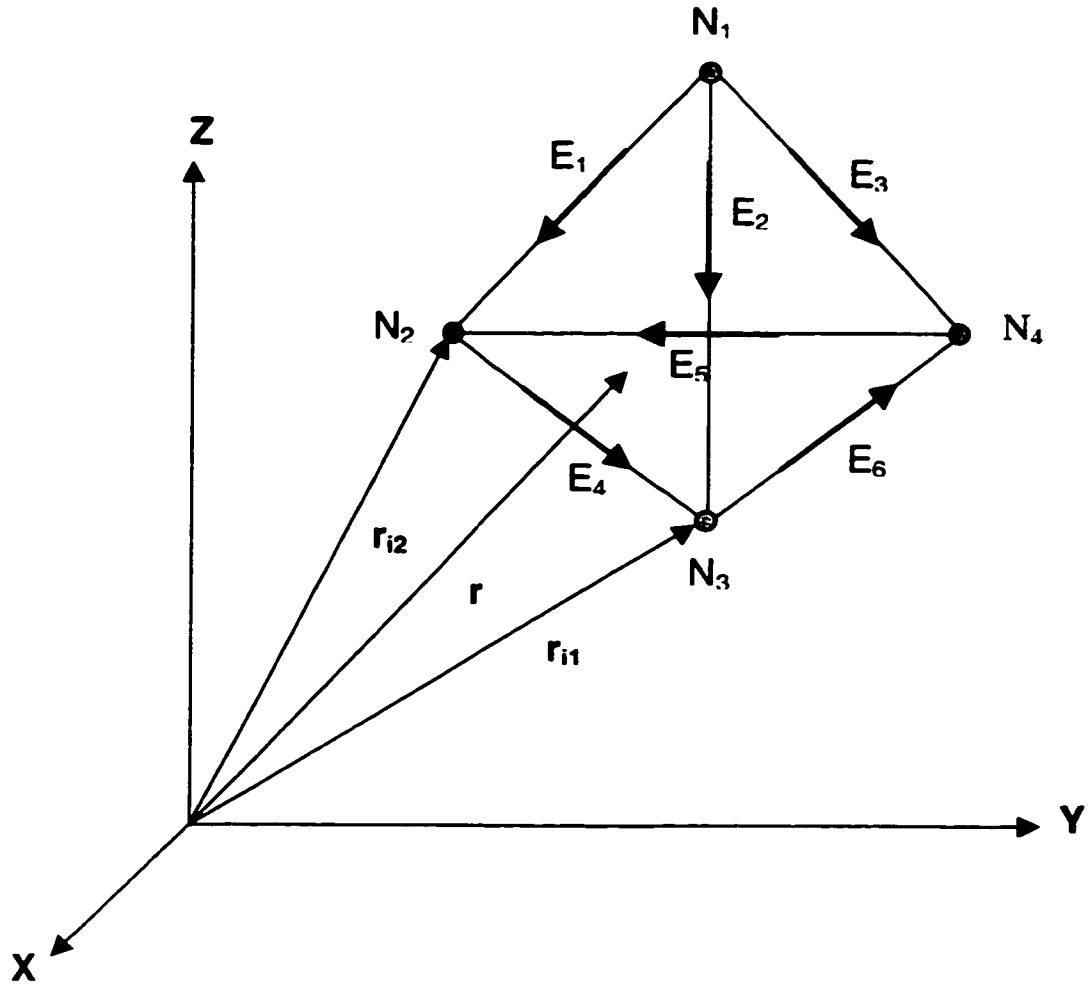

Figure 2.2: Tetrahedral element and associated nodes and edges. $N_1 \sim N_4$: node numbers. $E_1 \sim E_6$: edge numbers. $\bar{r}_{i1}$ and $\bar{r}_{i2}$: vectors associated with *ith* edge. $\bar{r}$ is an arbitrary vector which lies in the tetrahedral element.

2.4 Integration of FEM solutions into MoM Formulations

Once the FEM linear equation (Eq. (2.36)) is solved, we can incorporate FEM solutions into MoM formulations. Specifically, the sub-matrices, $[Y^c]$ and $[V_{inc}]$ can be computed with the obtained coefficient, ϕ_{ij}, as follows

$$y^c_{mn} = (-\overline{M}^a_m, \overline{H}^2_t(\overline{M}^a_n)) = \sum_{k=1}^{N_\phi} \phi_{kn}(-\overline{M}^a_m, \overline{\phi}_k) \tag{2.40}$$

$$V_{inc,m} = (-\overline{M}^a_m, \overline{H}^2_t(\overline{M}_f)) = \sum_{k=1}^{N_\phi} \phi_{kf}(-\overline{M}^a_m, \overline{\phi}_k) \tag{2.41}$$

where $\overline{M}$ is the basis function for the magnetic current, $\overline{\phi}$ is the edge vector basis, and N_ϕ is the number of $\overline{\phi}$. Therefore, Eq. (2.24) is finally solved with the known sub-matrices in Eqs. (2.40) – (2.41).

CHAPTER III

MULTI-RESOLUTION ANALYSIS (MRA) THEORY

The hybrid MoM/FEM method developed in Chapter II can more efficiently solve aperture-coupled electromagnetic problems than other existing methods. Nevertheless, as the scale of the problems is increased to some degree, this method essentially suffers from the demand for large amounts of memory and high computational time. To overcome these difficulties, we propose the incorporation of multiresolution analysis (MRA) theory into the hybrid MoM/FEM method.

In this chapter, we present MRA theory with an emphasis on the application to the hybrid MoM/FEM method. Starting with a brief historical review of MRA, we provide detailed explanations of MRA, including a simple example with one dimensional Harr basis functions. Next, we present wavelet basis functions for the aperture-coupled electromagnetic problem described in Fig. 2.1. Lastly, we discuss the computational efficiency achieved by MRA.

3.1 Background

Wavelets are a special group of basis functions originated from approximation theory in mathematics [26]. Since MRA theory was established in the early 1980's with the pioneer work of such mathematicians as Meyer, Daubechies, Chui, and others, MRA theory has been widely applied not only in the mathematical field but

also in other areas such as signal processing [27], image processing [28], and computer graphics [29]. An interest in wavelets also occurred in the electromagnetic community when Beylkin *et al.* [30] first proposed the use of wavelets in solving integral equations, and Alpert *et al.* [31] used "wavelet-like" basis functions to solve second-kind integral equations in the early 1990's. Fortunately, it did not take long for them to recognize the potential utility of wavelets in the electromagnetic area. Beginning with the application to the method of moments in electromagnetic wave interaction problems [32], a variety of electromagnetic problems have been explored using this special basis function. Particularly, various types of electromagnetic circuits are efficiently characterized utilizing wavelets: printed circuit antenna arrays [33], microstrip open stubs [34], dielectric resonators [35], waveguides [36], microstrip floating line structures [37], multiconductor transmission lines [38], microstrip patch antennas [39], and loop antenna arrays [40]. In addition, efforts have been made to develop faster and more efficient algorithms using wavelets in numerical electromagnetic computation. The developed techniques, as a result, include: (1) application of MRA theory to electromagnetic integral equations with oscillatory kernels for sparsely populated matrices [41]; (2) use of adaptive wavelet packet transforms for fast solutions of oscillating integral equations in electrodynamics and for maximum sparsity of system matrices [42]; (3) development of the impedance matrix compression (IMC) methods for adaptive selection of wavelets and better sparsity of system matrices [43]; (4) use of adaptive wavelets for non-uniform grids [44] and high sparsity. Interestingly, all the developed wavelet techniques have demonstrated a common powerful feature in their EM applications, namely, the generation of highly sparse linear systems [32]-[44]. In fact, the resultant matrix is dense, even with wavelets, because of the nature of the integral operator. However, primarily because of the local

support and vanishing moment properties of wavelets, many of the matrix elements are very small compared to the largest element, and therefore they can be tailored without significantly affecting the solution [45]. With the resultant sparse linear system, we can achieve: (1) significant savings in memory using a sparse matrix storage scheme, and (2) short computation time.

3.2 Wavelets and Multi-resolution Analysis (MRA)

A multiresolution analysis (MRA) of $\mathbf{L}^2(\mathbf{R})$ is defined as a nested sequence of subspaces $\{S_k\}_{k\in\mathbf{Z}}$, with the following properties [46], [47]:

1. $S_k \subset S_{k+1}, \qquad \forall k \in \mathbf{Z}$
2. $\bigcup_{k\in\mathbf{Z}} S_k$ is dense in $\mathbf{L}^2(\mathbf{R})$
3. $\bigcap_{k\in\mathbf{Z}} S_k = 0$
4. For any $f(x) \in \mathbf{L}^2(\mathbf{R})$ and any $k \in \mathbf{Z}$, $f(x) \in S_k \Leftrightarrow f(2x) \in S_{k+1}$
5. For any $f(x) \in \mathbf{L}^2(\mathbf{R})$ and any $k \in \mathbf{Z}$, $f(x) \in S_k \Leftrightarrow f(x - 2^{-k}m) \in S_{k+1}$

where $\mathbf{Z}$ denotes the set of integers. In MRA, an arbitrary square-integrable function $f(x) \in \mathbf{L}^2(\mathbf{R})$ can be approximated by a function that belongs to any of the subspaces S_k which can be derived from a central space S_o through dilation by integral powers of 2.

It has been shown that there exists a scaling function $\phi \in \mathbf{L}^2(\mathbf{R})$, such that $\{\phi_{k,m}(x)\}_{m\in\mathbf{Z}} = \{2^{k/2}\phi(2^k x - m)\}_{m\in\mathbf{Z}}$ is an orthogonal basis of S_k. Therefore, using the scaling function ϕ, the function $f(x)$ can be approximated onto the subspace S_k, at a resolution of 2^{-k}, by the projection operator defined as:

$$P_k(f)(x) = \sum_{m\in\mathbf{Z}} \phi_{k,m}(x)\langle \phi_{k,m}\ , f\rangle \quad \in V_k \tag{3.1}$$

where $\langle a, b \rangle$ denotes the inner product of $a(x)$ and $b(x)$. Note that the fine details smaller in resolution than 2^{-k} will be lost during the approximation. These lost fine details may be thought of as resting in the orthogonal complement of S_k, say W_k, in S_{k+1} defined as

$$S_{k+1} = S_k \oplus W_k \tag{3.2}$$

It has been shown that there exists a function $\psi(x)$, referred to as the wavelet function, such that the set

$$\{\psi_{k,m}\}_{m \in \mathbf{Z}} = \{2^{k/2}\, \psi(2^k x - m)\}_{m \in \mathbf{Z}} \tag{3.3}$$

is an orthogonal basis of subspace W_k and the set $\{\psi_{k,m}\}_{k,m \in \mathbf{Z}}$ is a complete orthogonal basis of $\mathbf{L}^2(\mathbf{R})$:

$$\mathbf{L}^2(\mathbf{R}) = \bigoplus_{k \in \mathbf{Z}} W_k$$

Therefore, the wavelet functions can be used in preserving the lost fine details for the next higher-level approximation subspace. From Eqs. (3.1) – (3.3), a function $f(x)$ in subspace S_{k2} can be obtained from the crude approximation of $f(x)$ in S_{k_1} and the wavelets of the intermediate subspaces as follows:

$$P_{k_2}(f)(x) = P_{k_1}(f)(x) + \sum_n \sum_{m=k_1}^{k_2-1} \psi_{m,n}(x) \langle \psi_{m,n}\, f \rangle, \quad k2 > k1 \tag{3.4}$$

Another form of Eq. (3.4) can be written as

$$S_{k_2} = S_{k_1} \bigoplus_{k_1 \le k \le k_2 - 1} W_k \tag{3.5}$$

Schematic view of Eq. (3.5) is shown in Fig. 3.1.

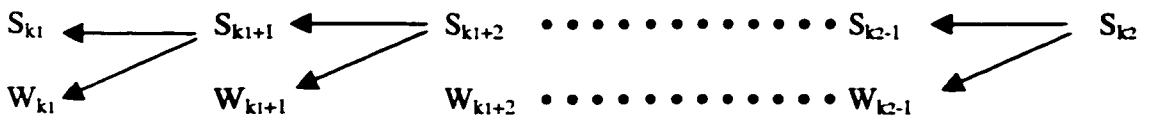

Figure 3.1: Multiresolution Analysis

An example of multi-resolution analysis (MRA) is shown in Fig. 3.2 using Harr scaling functions and wavelets. When the highest level scaling function is projected into lower resolution levels using MRA, the averages and derivatives of the highest scaling function are preserved in the lower level scaling functions and wavelets, respectively. Note that averages of Harr wavelets are zero in all resolution levels. The highest level scaling function can be constructed from its lower level scaling function and wavelets by the relation

$$\phi_3 = \phi_2 + \psi_2 + \psi_1 + \psi_0 \tag{3.6}$$

One-dimensional B-spline linear scaling functions and wavelets are shown in Fig. 3.3. Zero degree scaling function and wavelet, often called Harr bases, are used to model the transverse profile of current. The first-degree bases are used to expand the horizontal profile of current. We can directly employ the first-degree bases to an aperture-coupled electromagnetic problem in Fig. 2.1 that includes infinitely extended scatterers and apertures. On the other hand, for finite scatterers and apertures, the first-degree bases have to be modified accordingly to meet certain boundary conditions imposed on the scatterers and apertures. For instance, the edge currents in a patch antenna have to vanish along the normal direction of the current. The modification of the first-degree bases can be accomplished by: (1) removing the edge bases (half triangulars) in the first-degree scaling function, and (2) forcing both ends of the first-degree edge wavelet to zero. Other bases, zero-degree bases

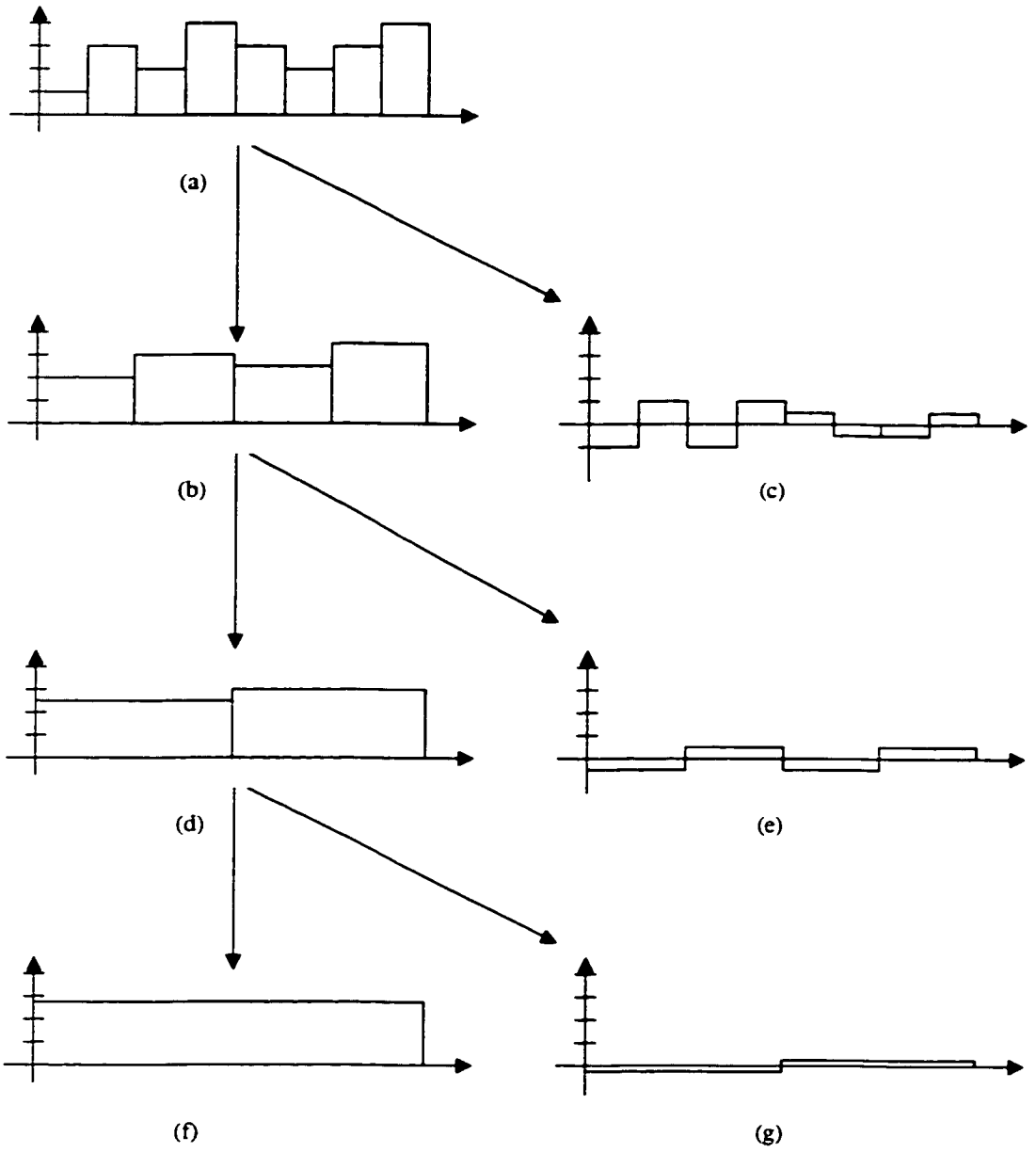

Figure 3.2: Multiresolution Analysis for Harr Scaling Function and Wavelet. (a) ϕ_3 Scaling function, (b) ϕ_2 Scaling function, (c) ψ_2 Wavelet, (d) ϕ_1 Scaling function, (e) ψ_1 Wavelet, (f) ϕ_0 Scaling function, (g) ψ_0 Wavelet.

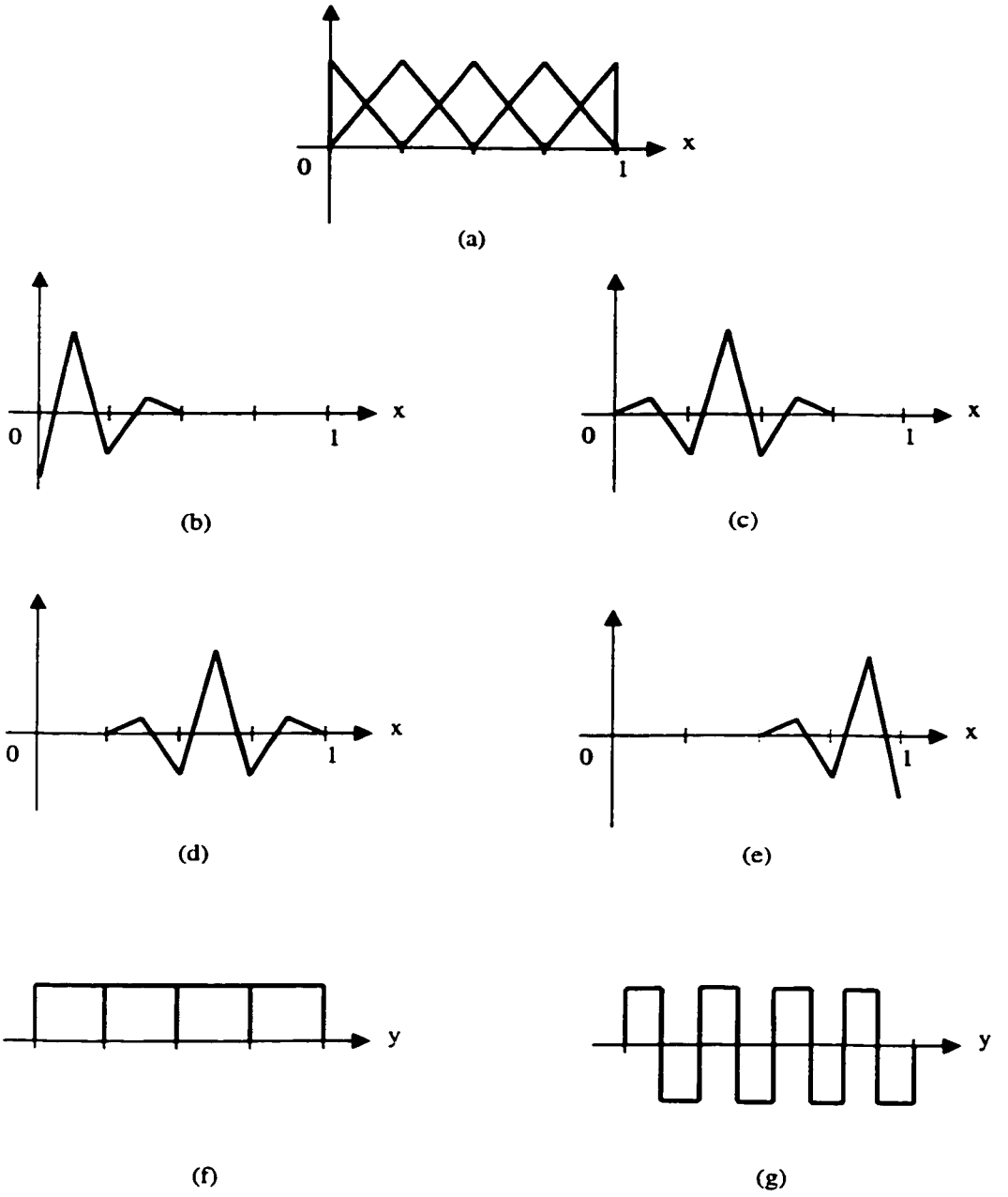

Figure 3.3: B-Spline Scaling and Wavelet Bases: (a) First-Degree Scaling Function, (b) First-Degree Right Edge Wavelet (c)–(d) First-Degree Normal Wavelet, (e) First-Degree Left Edge Wavelet (f) Zero-Degree Scaling Function, (g) Zero-Degree Wavelet

and first-degree wavelets, can be used without any modification. The modified one-dimensional B-spline linear scaling functions and wavelets are depicted in Fig. 3.4.

Since most practical electromagnetic problems include various types of two-dimensional finite structures, it is desired to produce two-dimensional scaling and wavelet bases for the application of MAR theory to arbitrary shaped plannar geometries. To this end, we construct two-dimensional bases from the modified one-dimensional bases in Fig. 3.4 by multiplying:

- zero-degree with first-degree scaling function – Fig. 3.5(a)
- first-degree scaling function with zero-order normal wavelet – Fig. 3.5(b)
- zero-order scaling function with zero-order normal wavelet – Fig. 3.5(c)
- first-order wavelet with zero-order wavelet – Fig. 3.5(d)
- zero-order scaling function with first-order edge wavelet – Fig. 3.5(e)
- zero-degree wavelet with first-degree wavelet – Fig. 3.5(e)

The edge wavelets (Fig. 3.5(e) and (f)) and their mirror images are used at the left and right end of the terminating boundaries, respectively.

Now, using these two-dimensional scaling and wavelet bases, we consider the incorporation of MRA into the aperture-coupled electromagnetic problem described earlier in Fig. 2.1. In the hybrid MoM/FEM method, we expanded the unknown magnetic and electric currents as

$$\overline{M}_s^a = \sum_{n=1}^{N_a} m^a{}_n \overline{M}^a{}_n$$

$$\overline{J}^b = \sum_{n=1}^{N_b} j^b{}_n \overline{J}^b{}_n$$

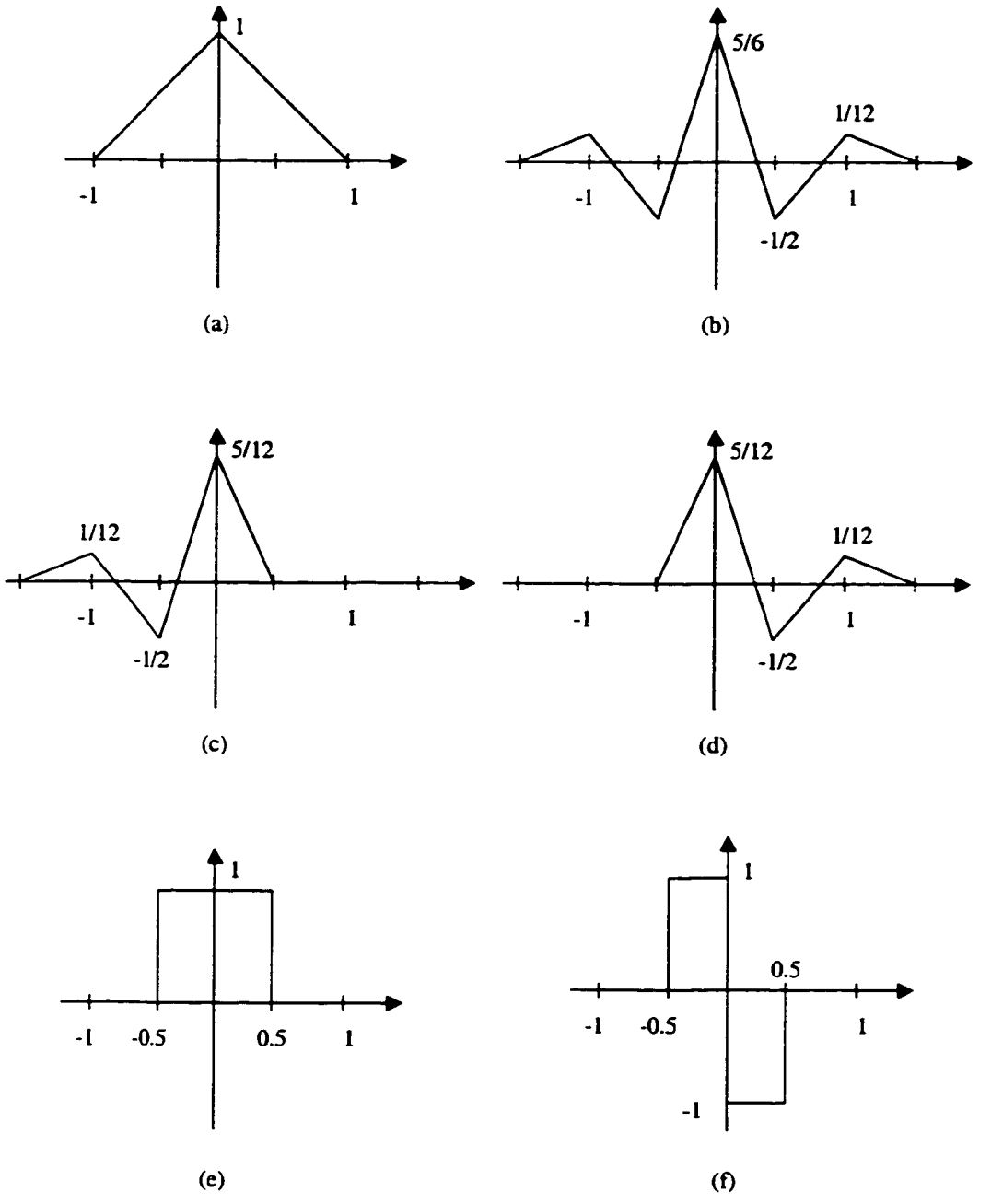

Figure 3.4: Modified B-Spline Scaling and Wavelet Bases: (a) First-Degree Scaling Function, (b) First-Degree Normal Wavelet (c) First-Degree Left Edge Wavelet, (d) First-Degree Right Edge Wavelet (e) Zero-Degree Scaling Function, (f) Zero-Degree Wavelet

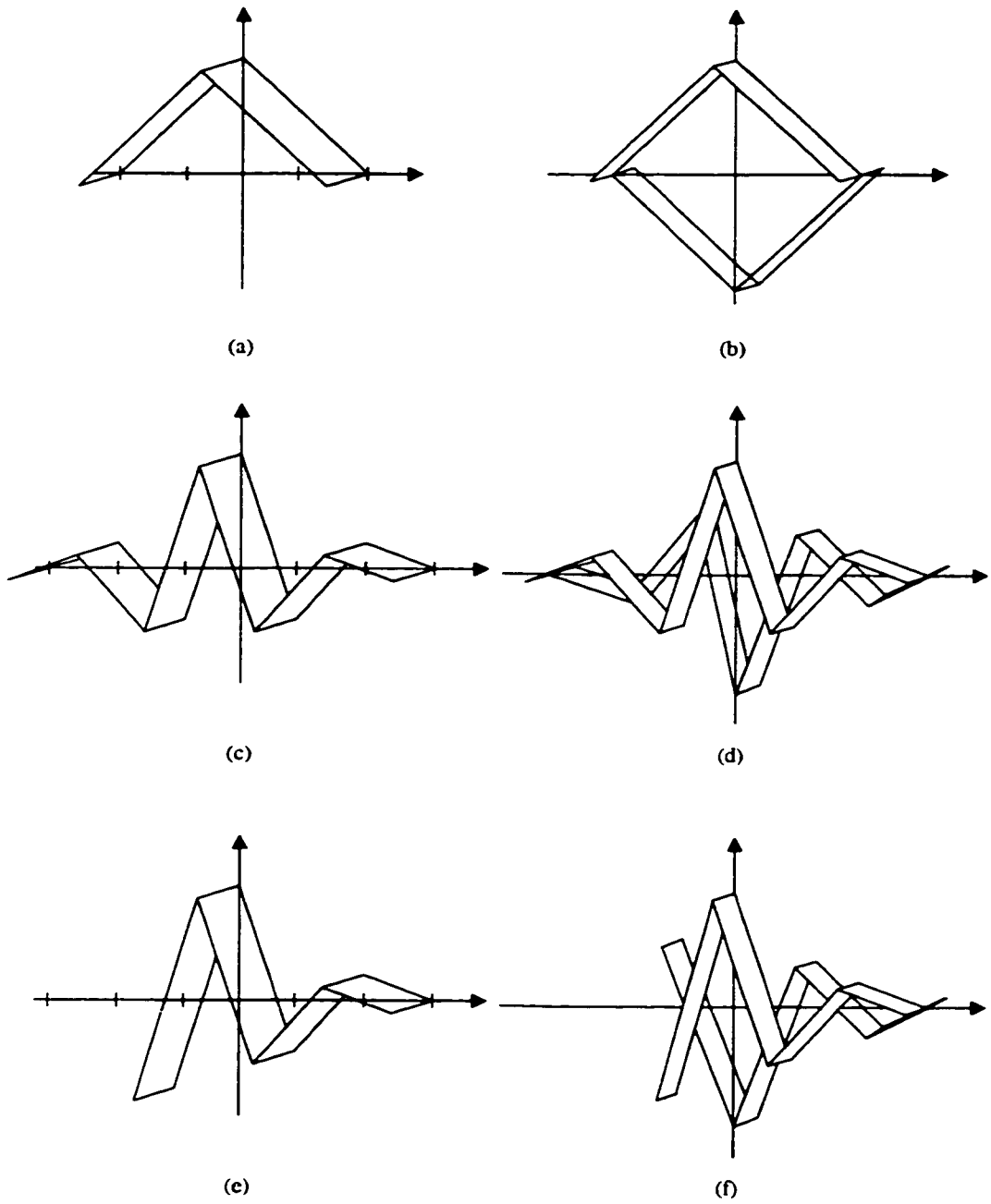

Figure 3.5: Two-Dimensional B-Spline Scaling and Wavelet Bases: (a) Scaling, (b)-(d) Normal Wavelet, (e)-(f) Edge Wavelet

where $\overline{M}^a{}_n$ and $\overline{J}^b{}_n$ are basis functions, $m^a{}_n$ and $j^b{}_n$ are unknown coefficients, N_a is the number of basis $\overline{M}^a{}_n$, and N_b is the number of basis $\overline{J}^b{}_n$. Therefore, the incorporation can be accomplished by expanding $\overline{M}^a{}_n$ and $\overline{J}^b{}_n$ with the two-dimensional scaling and wavelet bases and computing the hybrid sub-matrices defined in Chapter II as

$$\begin{aligned}
y^a_{mn} &= (-\overline{M}^a_m, \overline{H}^1_t(\overline{M}^a_n)) \\
y^c_{mn} &= (-\overline{M}^a_m, \overline{H}^2_t(\overline{M}^a_n)) \\
z^b_{mn} &= (-\overline{J}^b_m, \overline{E}^1_t(\overline{J}^b_n)) \\
t^b_{mn} &= (\overline{J}^b_m, \overline{E}^1_t(\overline{M}^a_n)) \\
c^b_{mn} &= (\overline{M}^a_m, \overline{H}^1_t(\overline{J}^b_n)) \\
V_{inc,m} &= (-\overline{M}^a_m, \overline{H}^2_t(\overline{M}_f))
\end{aligned}$$

Note that the sub-matrices y^a_{mn}, z^b_{mn}, t^b_{mn}, and c^b_{mn} are computed using MoM, while y^c_{mn} and $V_{inc,m}$ are solved by FEM.

The integration of MRA theory into the hybrid MoM/FEM method enhances the computational efficiency of the hybrid linear system. As shown in the above equations, computations of the hybrid sub-matrices involve integrations of Green's function with scaling functions and wavelets. Due to the vanishing moment properties of wavelets, many of the resultant sub-matrices' elements become very small compared to the largest element, and can be discarded without significantly affecting the solution (often called threshold) [31] - [45]. This threshold process is applied to the sub-matrices which consist of the system matrix shown in the following equation. They are: $[Z^b]$, $[T^b]$, $[C^b]$, $[Y^a]$, and $[Y^b]$.

$$\begin{bmatrix} [Z^b] & [T^b] \\ [C^b] & [Y^a] + [Y^b] \end{bmatrix} \begin{bmatrix} [J^b] \\ [M^a] \end{bmatrix} = \begin{bmatrix} 0 \\ -[V_{inc}] \end{bmatrix}$$

It is important to emphasize that the threshold must be performed in each sub-matrix independently. This is because the system information in each sub-matrix has different order of magnitude and, therefore, the largest element varies among the sub-matrices. If we choose the single largest element from all sub-matrices and use the same largest element in the threshold, some of the sub-matrices will loose critical system information, leading to an inaccurate solution of the problem. For this reason. the implementation of local thresholds plays a key role in achieving a sparse linear system that guarantees an accurate solution. The resultant highly sparse matrices will not only enhance the solution time of the hybrid linear system but also will result in huge memory savings by using sparse-matrix storage schemes. This subject has been rigorously investigated for aperture-coupled patch antenna problems in Chapter V and Chapter VI.

CHAPTER IV

HIGH PERFORMANCE COMPUTING (HPC)

Throughout the previous two chapters, we have focused on solving aperture-coupled electromagnetic problems efficiently by developing the hybrid MoM/FEM method and incorporating multiresolution analysis. Specifically, by effectively combining FEM and MoM, the hybrid MoM/FEM method has minimized computational loads for the problem and eliminated analytical difficulties of deriving the required Green's functions in FEM domain. Moreover, the hybrid MoM/FEM method becomes computationally very efficient with the integration of MRA theory (significant decrease in storage requirement and execution time due to a highly sparse hybrid linear system), making it more attractive and competitive. In spite of these theoretical and numerical improvements, we still suffer computational difficulties in many practical large-scale electromagnetic problems. Such difficulties include large memory requirement for FEM linear systems, long computation times from the many repeated FEM and MoM computations for frequency points and magnetic sources. In addition, a significant amount of memory is often required to store the large sparse hybrid linear system.

To circumvent those computational obstacles, we have considered the use of High-Performance Computing (HPC) in the wavelet hybrid MoM/FEM method. In par-

ticular, we use a task parallelization to accelerate the many repeated FEM and MoM computations for excitations and frequencies, while we employ a matrix decomposition scheme to deal with the large FEM and hybrid linear systems [48]. This study is supported by a number of examples to provide adequate justification for the presented arguments.

4.1 Background

HPC environments offer computers with the highest available computing power, usually achieved by means of a large memory and large number of processors collaborating to solve one (or at most a few) computationally intense problems at a time. Historically, HPC has advanced not only by the growth of hardware technology but also by the development of software that support parallel computation. Parallel systems matured and entered the commercial production between 1975 and 1990 [49]. At that time, however, it was difficult to implement full parallelism and achieve the high potential performance levels because the software of the time performed poorly and was difficult to use. The software has since been improved to correct these weaknesses and broaden the scope of HPC. Nevertheless, it has not yet matured enough to be used in as friendly and convenient a manner as the personal computer or ordinary workstation [50]. One of the major hindrances to the development of appropriate software is the broad range of different parallel systems dedicated to certain classes of research. As a result of lack of standardization, early HPC users could not have software portability across different types of parallel machines [51, 52]. It was not until the early 90s that vendors agreed to develop a standard parallel language, the MPI (Message Passing Interface) standard [53]-[55], as a part of HPC standardization. Along with the vendors' own software for their systems, MPI has

been developed continuously among the vendors to support various kinds of parallel systems [56, 57]. In comparison to software development for HPC systems, even greater progress has been made on the hardware side over the past 20 years, due to the fast-growing VLSI technology. Hundreds of processors with giga-hertz clock speeds, giga-bytes of memory, and tera-bytes of hard disk space, become standard hardware features of today's state-of-the-art parallel computers [58]– such as the IBM Blue Horizon [59], IBM SP2 [60], and HP V2500 [61]. To take full advantage of such advanced hardware systems and stay competitive with sequential computing, HPC has yet to clear many unresolved issues, such as programming familiarity, performance stability, and performance portability [62]. Nevertheless, HPC has been regarded as a powerful and attractive computing resource because it can deliver a large amount of memory and fast computation capability. It has greatly contributed to many scientific areas (for example, biology - mapping the chemical sequences for human DNA [63], graphics and visualization - constructing digital astronomical models that re-create the Milky Way, and, eventually, the universe [64]) by dealing with large-scale problems which typically have millions of unknowns.

4.2 The Architecture of a Parallel Computer

Parallel computers can be classified according to memory structure as either no-shared memory systems or shared memory systems. In a no-shared system, each processor is connected to the other processors by high speed switches or through network connection (ethernet), and, as the name implies, has a private memory which is not shared with other processors. As a result, data is transferred between processors by message passing communications. For this reason, it is often referred to as a message passing system. Due to the need to explicitly encode all communications

between processors, it is difficult to create a initial program. However, a no-shared memory machine is still attractive because of its scalable performance. A schematic diagram is shown in Fig. 4.1(a) [65].

Unlike the previous case, a shared memory system has global memories that can be accessed by all processors. The shared memory model has been implemented in two different systems: (1) Uniform Memory Access (UMA) system; and (2) Non-Uniform Memory Access (NUMA) system. An UMA system is characterized by the constant memory access time for all processors. This has been realized by connecting processors to a system bus and making them equally distanced from the global memories - Fig. 4.1(b). Due to the limited bandwidth of the shared system bus, the UMA system may suffer bottlenecks coming from the congestion of access to the global memory in the system bus. Thus, the UMA system does not scale well as a number of processors increase. As shown in Fig. 4.1(c), NUMA system has global memories which are physically distributed and virtually shared. Therefore, processors can access their local memory faster than remote memory. This type of structure offers ease of shared-memory programming and scalability at the cost of non-uniform memory access time.

In general it is easier to create an initial program for a shared memory system than for a no-shared memory systems because the shared memory system allows the programmer to ignore the communications between processors and concentrate on dividing the program into tasks that can be performed in parallel. However, shared memory systems require other programming efforts as a result of their unique architecture. Effective manipulations of multiple simultaneous accesses to a single memory location caused by more than a single processor is one such effort required in shared memory systems.

The best choice of a parallel architecture depends on the application runs that need to be executed, the programming model which needs to be supported, and the required costs.

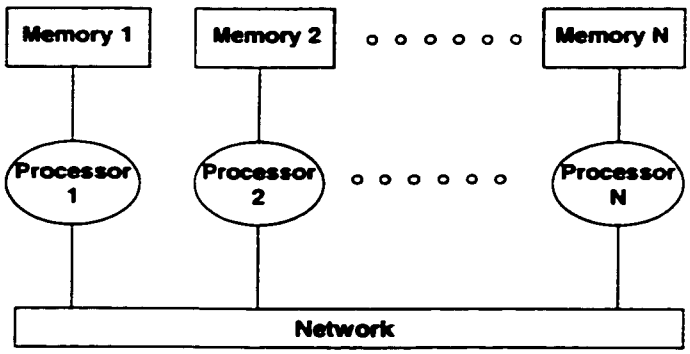

(a)

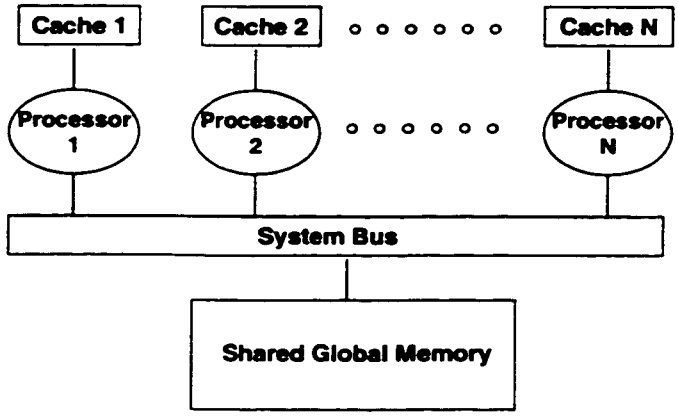

(b)

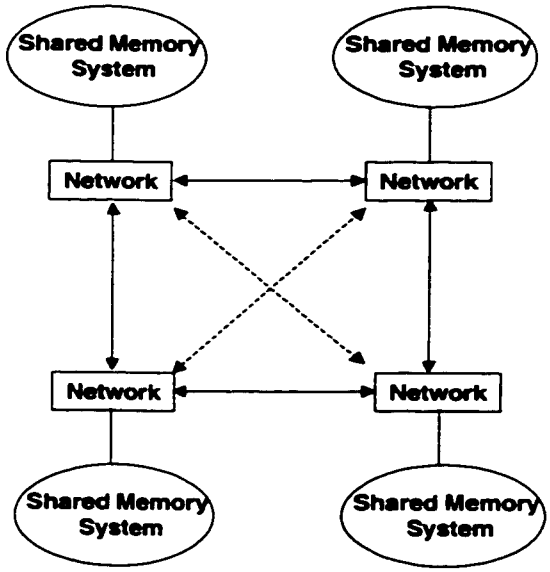

(c)

Figure 4.1: Architecture of Parallel Machines (a) No-Shared Memory System, (b) Uniform Memory Access (UMA) System, (c) Non-Uniform Memory Access (NUMA) System. The systems depicted in (b) and (c) are of the shared memory type.

4.3 FEM Task Parallelization

In the hybrid MoM/FEM method, FEM is applied repeatedly over different excitations and frequency points to compute the sub-matrices $[Y^c]$ and $[V_{inc}]$ defined in Eqs. (2.40) – (2.41) as

$$y^c_{mn} = (-\overline{M}^a_m, \overline{H}^2_t(\overline{M}^a_n)) = \sum_{k=1}^{N_\phi} \phi_{kn}(-\overline{M}^a_m, \overline{\phi}_k) \tag{4.1}$$

$$V_{inc,m} = (-\overline{M}^a_m, \overline{H}^2_t(\overline{M}_f)) = \sum_{k=1}^{N_\phi} \phi_{kf}(-\overline{M}^a_m, \overline{\phi}_k) \tag{4.2}$$

where $\overline{M}^a_n$ and $\overline{M}_f$ are magnetic sources, $\overline{\phi}$ is the FEM edge vector basis, and N_ϕ is the number of $\overline{\phi}$. It has been clearly shown in Chapter II that the sub-matrices can be computed from ϕ by solving a FEM linear system expressed as:

$$[A][\Phi] = [B]$$

where ϕ is the element of the vector $[\Phi]$. Note that the overall memory size required for FEM computation is determined by the dimension of a FEM linear system.

To speed up the sub-matrix computations over the desired frequency points, we have applied task parallelization schemes in FEM computations. It is important to mention that for this task parallelization, the size of a FEM linear system should not exceed the memory assigned to a single processor. Otherwise, the FEM linear system has to be divided in a number of processors using the matrix decomposition method which will be discussed later.

Task parallelization is a simple and easily implementable method that can be utilized in FEM calculations. Figure 4.2 shows how this parallelization performs the required tasks in a multi-processor environment. As seen from the figure, the tasks are first distributed to processors and then executed in these processors simultaneously. Assuming that the tasks are independent of each other, as it happens in

moderately sized FEM computation, each processor can carry out its assigned tasks with minimum communication overhead. As a result, we can achieve almost linearly scalable performance. It is worthwhile to emphasize again that each processor should be provided the memory required to perform its assigned task in order to be computationally independent from other processors and achieve maximum scalability. Otherwise, the communication overhead among processors grows and the overall computation slows considerably. Among the available parallel systems, the no-shared memory system has the most suitable architecture for effectively handling FEM task parallelization and can alleviate the above problem because all FEM computations can be executed independently among processors using their large local memory.

Since FEM can be independently applied for each source and frequency point, we have considered three possible task parallelizations in the hybrid FEM computation: (1) frequency parallelization; (2) source parallelization; and (3) frequency-source parallelization (the combination of the frequency and source parallelization).

In frequency parallelization, frequency points are processed in parallel but sources are processed serially. As shown in Fig. 4.3, FEM computations over different frequency points are distributed to the processors and performed simultaneously to solve Eqs. (4.1) and (4.2). Each processor performs the identical FEM routine with same magnetic sources, but for a different set of frequency data. This parallelization and execution strategy is called the SIMD (Single Instruction Multiple Data Stream) model when the processors are synchronized to execute the same instruction at the same time. Several early parallel computers (eq., Illiac IV, Maspar) were tailored to support this parallel execution model. In modern multiprocessor computer systems, each processor can execute its own copy of the program and synchronization need not be enforced; this generalization results in the SPMD (Single Process Multiple

Data Stream) model.

Another way of implementing task parallelization is the reverse case of the previous parallelization : (1) frequency points - serial processing; (2) magnetic sources - parallel processing. In this way, Eqs. (4.1) and (4.2) are computed over all magnetic sources at a single frequency point simultaneously, but frequency points are processed one after another. Figure 4.4 shows this source parallelization. This scheme affords more parallelism when the number of sources is greater than the number of frequency points. Increased parallelism is advantageous in that it allows more processors to participate, resulting in a proportional speedup.

Frequency-source parallelization is the most efficient scheme of three in that both frequency points and sources are processed in parallel way. As shown in Fig. 4.5, the frequency-source parallelization assigns a distinct range of frequency points and sources to each processor while only a range of frequencies or a range of sources is assigned to each processor in the previous two methods. In this manner, we can have more flexibility in distributing computational tasks according to the number of available processors. This combined parallelization method can use all available processors while neither of the previous two methods can use more processors than the maximum number of frequency points or the maximum number of sources, respectively. The combination can use a number of processors equal to the product of the number of frequency points and the number of sources.

For a simple demonstration of task parallelization, the computation of an electromagnetic circuit shown in Fig. 4.6 is considered. This type of geometry is commonly found in a packaged high-frequency electromagnetic circuit. The center conductor is used to send electromagnetic signals while the surrounding via fences are used to support a metal package which provides shielding against electromagnetic interfer-

ence and physical protection from hostile environments. The circuit is filled with a dielectric material ($\epsilon_r = 2.5$) and covered at the top and bottom with perfect electric conductors. The via fences are located 0.25 mm from the center conductor and each via has a diameter of 0.25 mm. The via-to-via spacing is 1.3 times the via diameter. Utilizing frequency parallelization, FEM computation is performed over 32 frequency points to solve 160,000 unknowns in this geometry.

Figure 4.7(a) shows the computed total electric field distribution in the substrate of the circuit at 25GHz. Since the via holes are closely spaced for the electromagnetic field at this frequency, the field is confined around the center conductor. Thus, these via fences can be used to isolate the electromagnetic field and reduce electric couplings in high density circuit regions. The performance of the applied task parallelization is shown in Figure 4.7(b). As expected, we have achieved almost linearly scalable performance for frequency parallelization over the 32 frequency points.

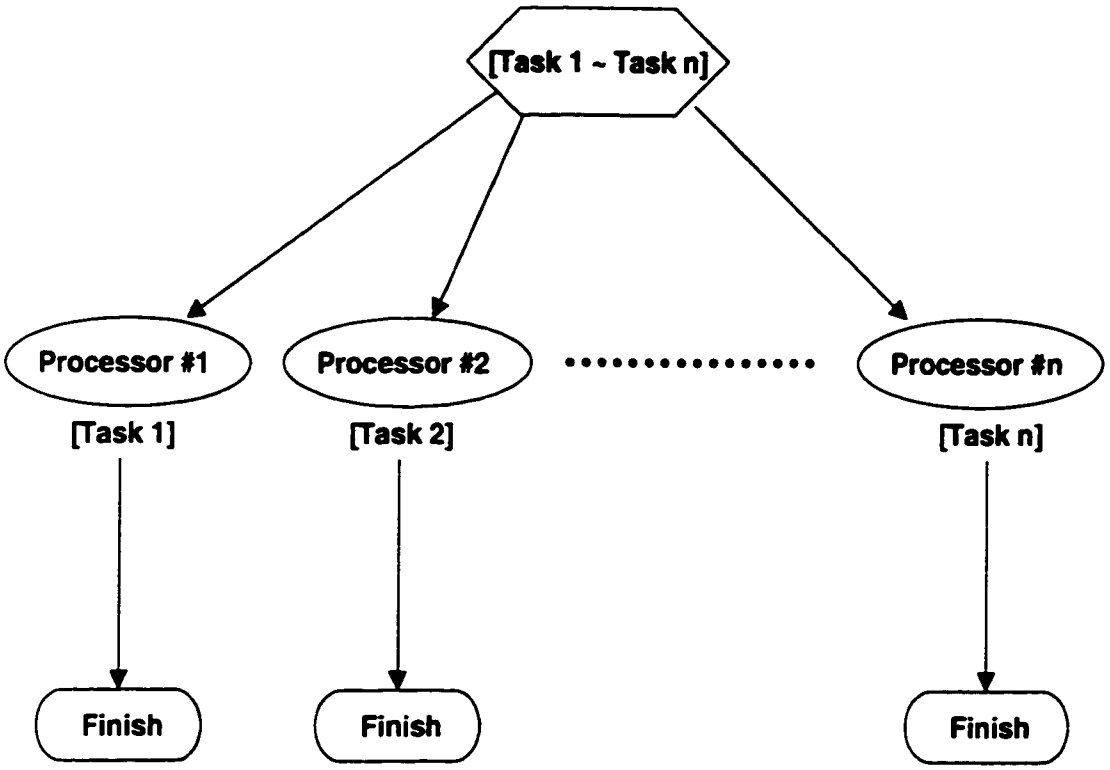

Figure 4.2: Task Parallelization Scheme

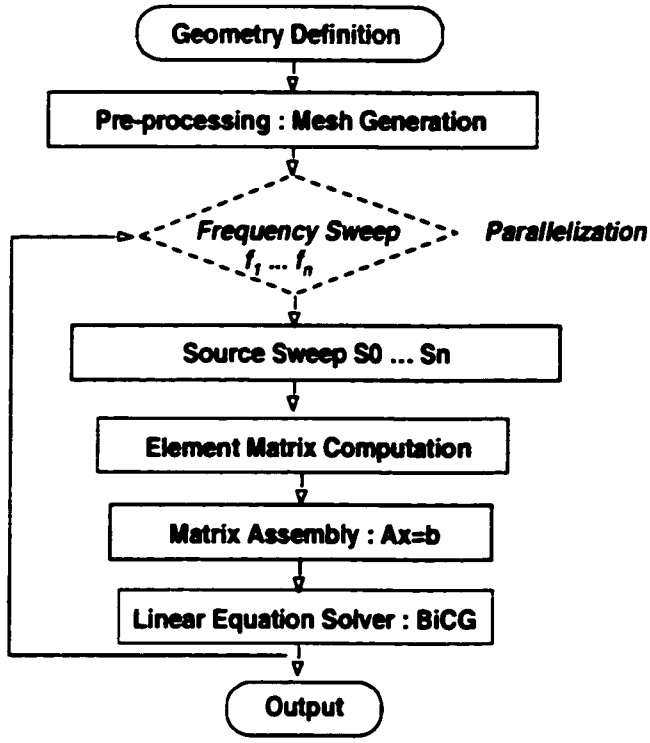

(a)

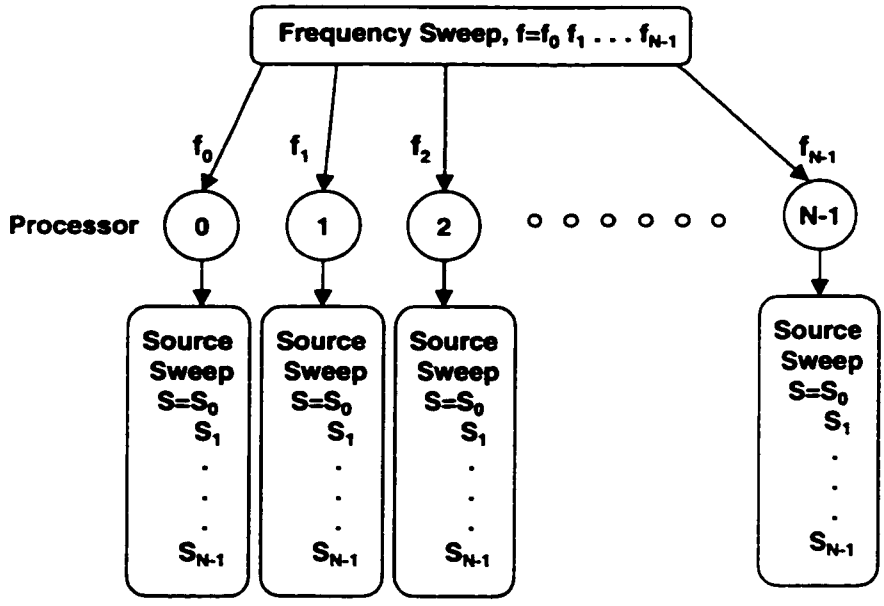

(b)

Figure 4.3: Frequency Parallelization Scheme

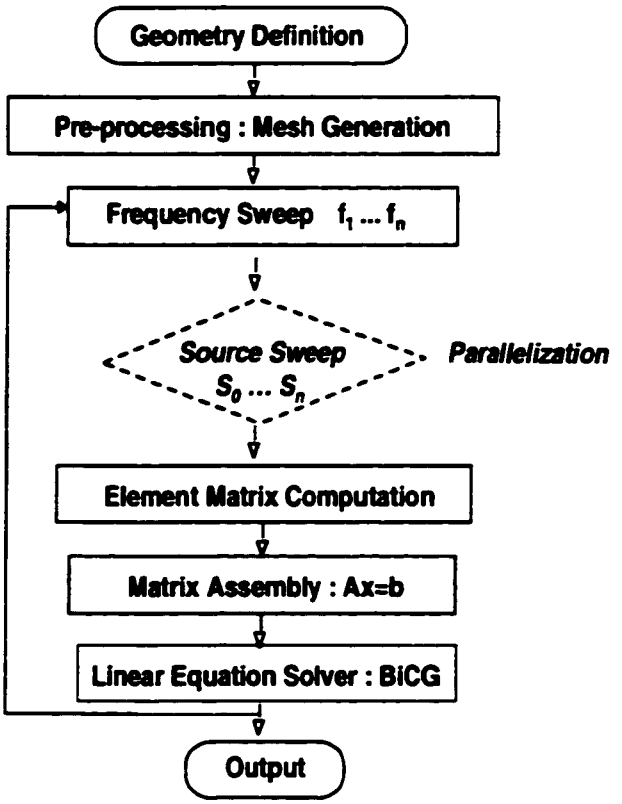

(a)

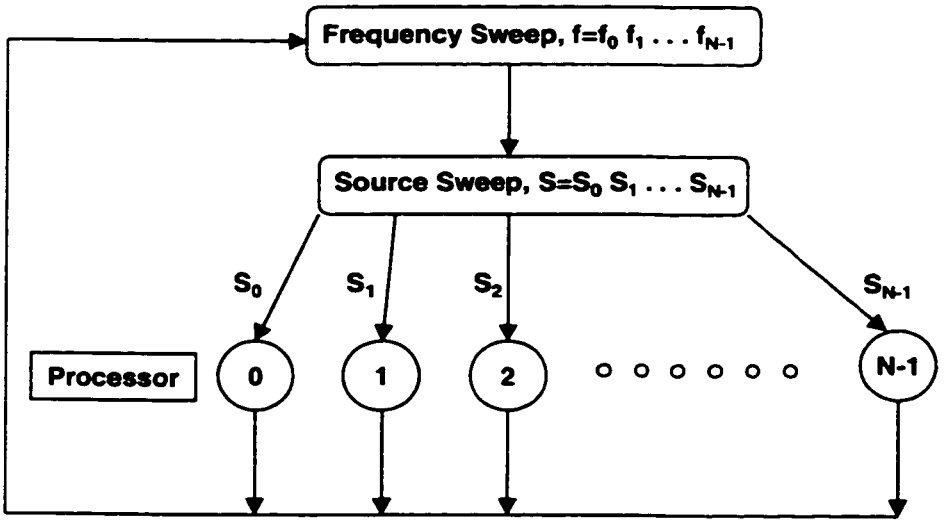

(b)

Figure 4.4: Source Parallelization Scheme

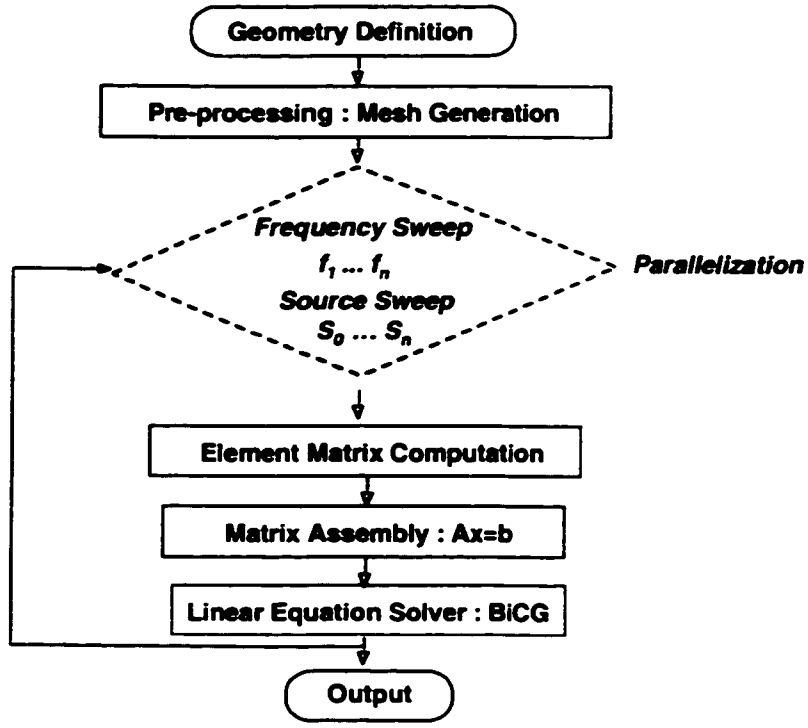

(a)

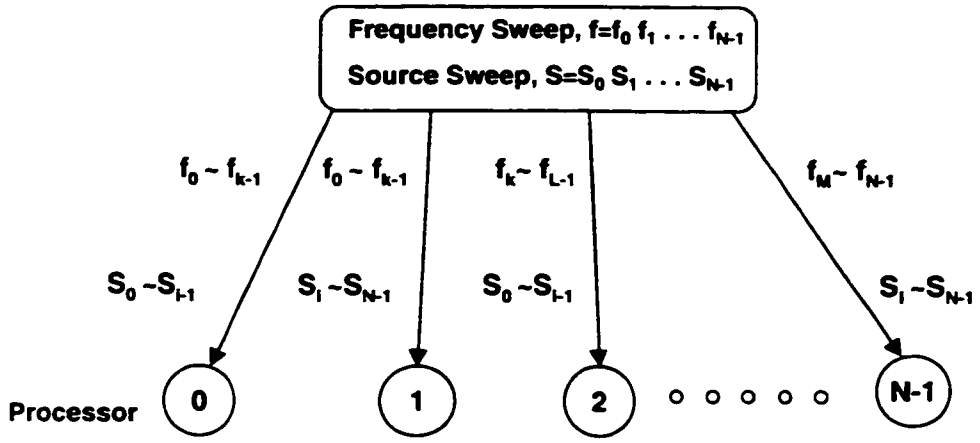

(b)

Figure 4.5: Frequency-Source Parallelization Scheme

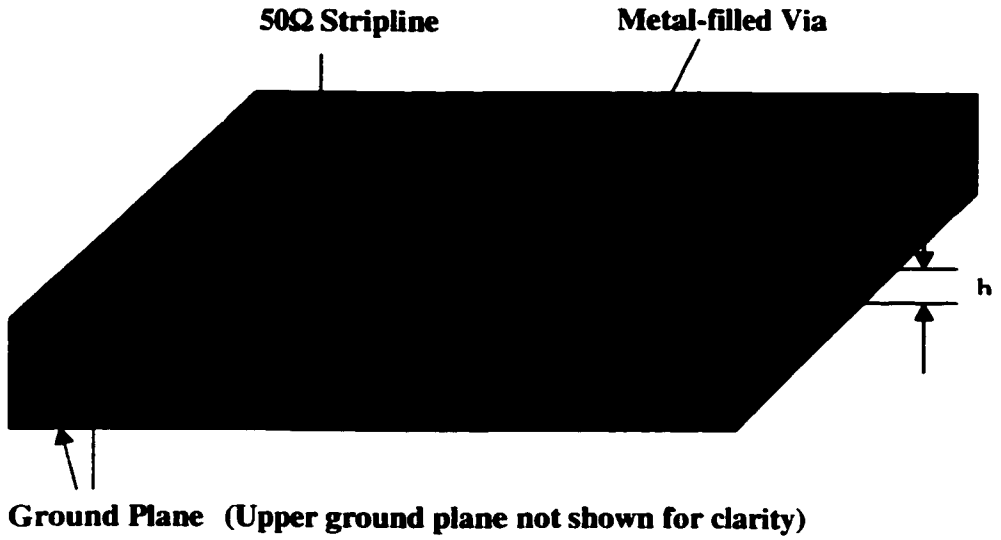

(a)

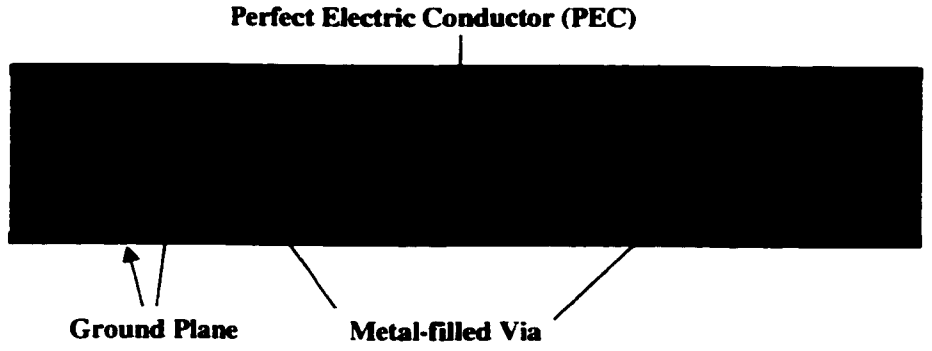

(b)

Figure 4.6: Example of task parallelization: Stripline with via fences surrounding center conductor, $\epsilon_r = 2.5$, h = 0.25 mm, H = 2h, G = 1.3h, S = 1h, D_v = 1h. (a) Schematic view, (b) Cross-section view

(a)

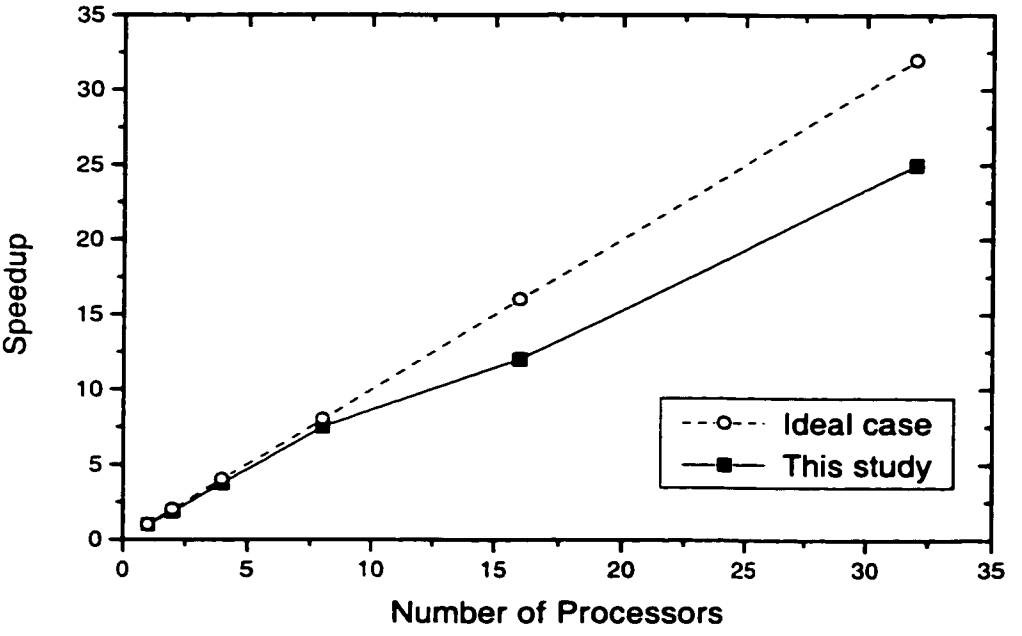

(b)

Figure 4.7: (a) Top view of the total electric field in the stripline circuit (b) Performance measurement

4.4 Matrix Decomposition Method

The matrix decomposition method is a parallelization paradigm used to solve a large linear system which can not be stored in a single processor. This technique can be utilized to handle any type of linear system which has the form $[A][x] = [B]$ and is solved by iterative methods [66]. It is well known that non-iterative methods such as gaussian elimination are not efficient for solving large linear systems because of their long computation time and large memory requirements. We use matrix decomposition to solve two large linear systems in an hybrid MoM/FEM method: (1) an FEM linear system (Fig. 4.8) in Eq. 4.3;

$$[A][\Phi] = [B] \tag{4.3}$$

and (2) a hybrid linear system in Eq. 2.24;

$$\begin{bmatrix} [Z^b] & [T^b] \\ [C^b] & [Y^a] + [Y^b] \end{bmatrix} \begin{bmatrix} [J^b] \\ [M^a] \end{bmatrix} = \begin{bmatrix} 0 \\ -[V_{inc}] \end{bmatrix}. \tag{4.4}$$

We have considered two matrix decomposition scenarios [67], [68] and present them below in detail.

The first scenario is shown in Fig. 4.9. In the initial stage, portions of a large linear system, $[A_i]$, are generated in a master processor and transferred to slave processors (step 1). Once the slave processors have received sections of the linear systems, they all start an iterative solution process. There are two critical operations in the iterative solution routine that have to be carefully parallelized: (1) renewal of a solution vector, $[x]$, in each processor, and (2) matrix-vector operation, $[A] \cdot [x]$, using the partial linear system stored in the processors. With this parallelization algorithm, these tasks are accomplished by broadcasting a new $[x]$ to all processors (step 2), performing partial matrix-vector products in each processor (step 3), and gathering

Case	Order of unknowns (N)	Matrix dimension
FEM linear system	10^7	25×10^7 ($25 \times$ N)
Hybrid linear system	10^4	10^8 (N^2)

Table 4.1: The estimated dimension of the matrix [A] in the FEM and hybrid linear systems.

and combining the results from each processor (step 4), as shown in Fig. 4.9. Note that the communication processes, broadcasting and gathering, are limited by the bandwidth of the interconnection network of the parallel system which may be a simple ethernet, high speed bus, very high speed multistage switch, or hypercube. Moreover, they are limited by software overhead for generating messages if a message passing paradigm is used for communications. The particular interconnection network used considerably affects the overall computation time of the iterative solution routine, as well as the cost of the parallel computer system.

The first matrix decomposition method is simple and easily implementable. But the cost paid is a communication latency between the master and slave processors caused by the transfer of the matrix [A] and the vector $[x]$. The distribution of matrix [A] to processors occurs only once at the beginning of the solution process. Even so, and even though a sparse matrix storage scheme is used, the transfer takes a considerable portion of the total run time because of the large dimension of the matrix [A]. To address this argument quantitatively, we have estimated the dimension of the matrix [A] in the FEM and hybrid linear systems in Table 4.1. In both cases, an order of 10 million matrix elements is involved in the distribution of the matrix [A]. The unknown coefficient vector $[x]$, on the other hand, is updated in every iteration as the master processor broadcasts the $[x]$ to the slave processors. Considering that about 90% of the total run time is spent in an iterative solution process, this broadcasting communications leads to the major computational delay. Therefore, the first method

proves to be inefficient for large-scale electromagnetic problems. For this reason, we have considered the second scenario to minimize the overall communication cost in the solution process.

The main interest in the second scenario is how to distribute matrix [A] and update vector $[x]$ in the least communication time. Since the generation of matrix [A] takes less than 10% of the total run time, we have considered the generation of the partial matrix, $[A_i]$, in each processor - Fig. 4.10(a). instead of generating it in the master processor and sending the appropriate portion to each slave processor. By generating $[A_i]$ directly in the slave processors, while we skip only one communication process, we can save much communication time. In this partitioning, it is important to balance the dimensions of the partial matrices among the processors in order to maximize the computational speed and efficiency. The major saving can be achieved in the updating of vector $[x]$ when matrix [A] is sparse. In this case, we need not send the entire vector $[x]$ to every slave processor. Using the indices of the non-zero elements in the partial matrix associated with each particular slave processor, we can send that processor a portion of vector $[x]$ which has values only at these indices (step 2). Since this reduction of $[x]$ occurs in every iteration, we can considerably reduce the communications between processors that occur during each iteration, which eventually will save a significant amount of the total execution time of an iterative solution process. The saving becomes ever more significant as the number of unknowns in a problem reaches to the order of 10^7 and the number of iterations is proportionally increased. After the matrix-vector multiplication is carried out, using indirect indexing of the partial [A] and [x] (step 3) in each processor, the results are collected by the master processor and combined to give a final result of $[\mathbf{A}] \cdot [\mathbf{x}]$ (step 4).

As an example of this matrix decomposition method, we have applied the second matrix decomposition method to a simple, but large microstrip structure (Fig. 4.11(a)). Artificial absorbers (AA) have been used in the substrate and free space region to terminate the infinite section of microstrip. This problem has 67 $\times$ 211 $\times$ 85 grid points and a total of 7,100,411 unknowns (each rectangular block is subdivided into tetrahedral elements) . The 2G-Bytes of memory required for FEM computation has been provide by dividing it over more than 9 processors (each processor has 256M-Bytes of memory). The run time for 9 to 16 processors was measured, as shown Fig. 4.11(b). Because of the communication overhead among processors, the performance is not as scalable as for the task parallelization case. However, this parallel scheme can handle and solve a large linear system in reasonable amount of time. The computed return loss is shown in Fig. 4.11(a).

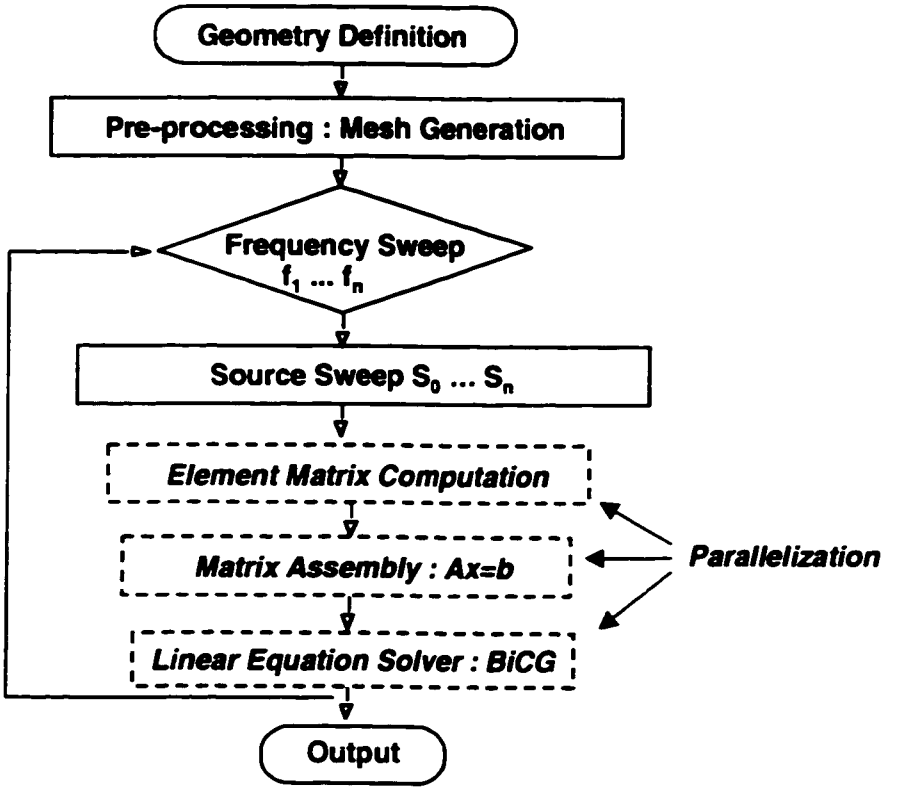

Figure 4.8: Parallelization of FEM iterative solver

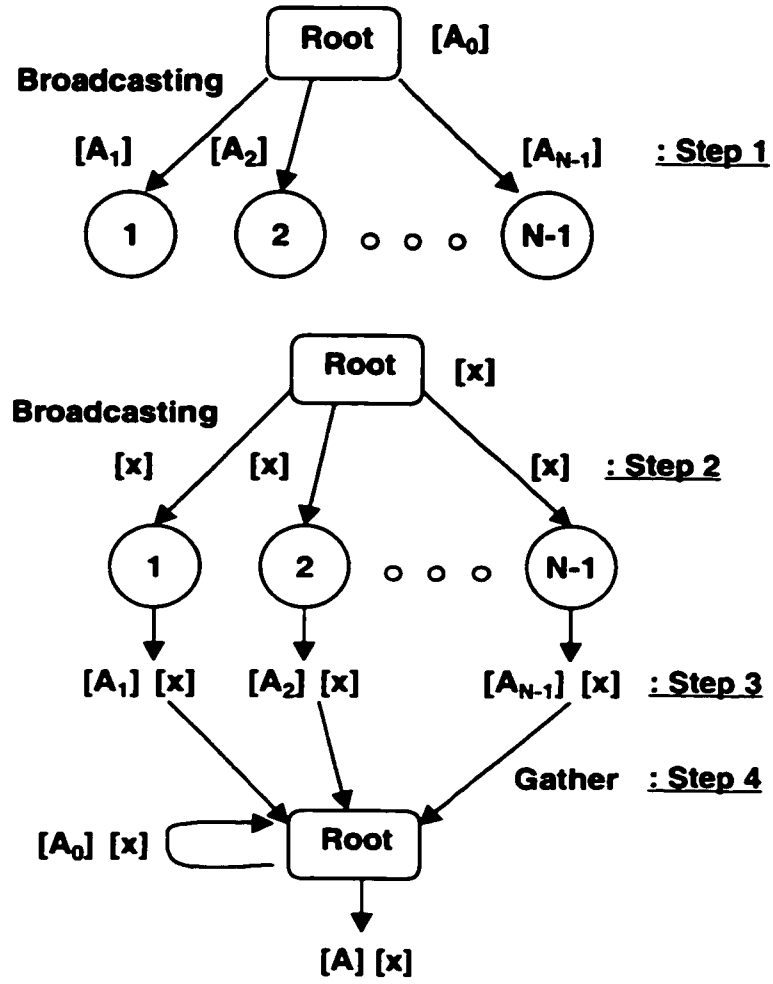

Figure 4.9: Matrix-Decomposition and Matrix-Vector Multiplication: Scheme I, where $[A] = \bigcup_{i=0}^{N-1}[A_i]$, Step 1 - send a partial linear system to each slave processor, Step 2 - broadcast renewed $[x]$, Step 3 - perform partial matrix-vector multiplication in processors simultaneously, Step 4 - collect the results and give the final result of $[\mathbf{A}] \cdot [\mathbf{x}]$

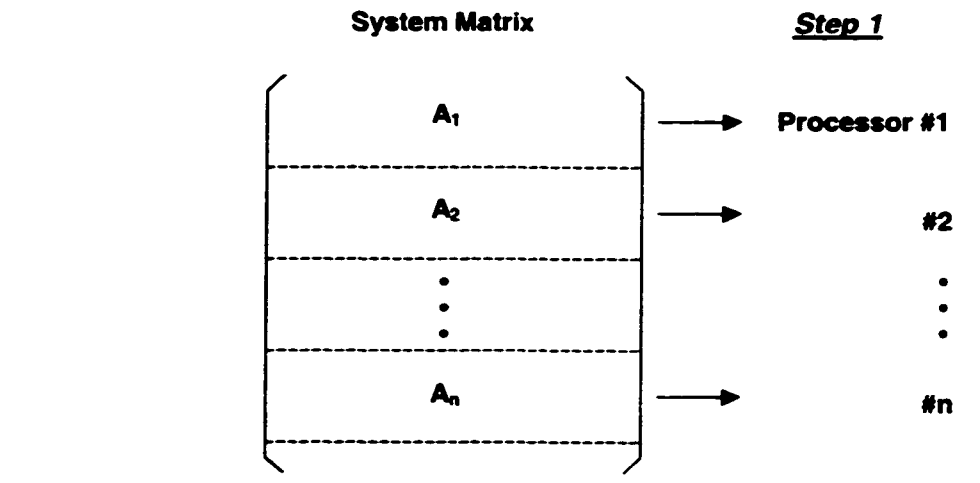

(a)

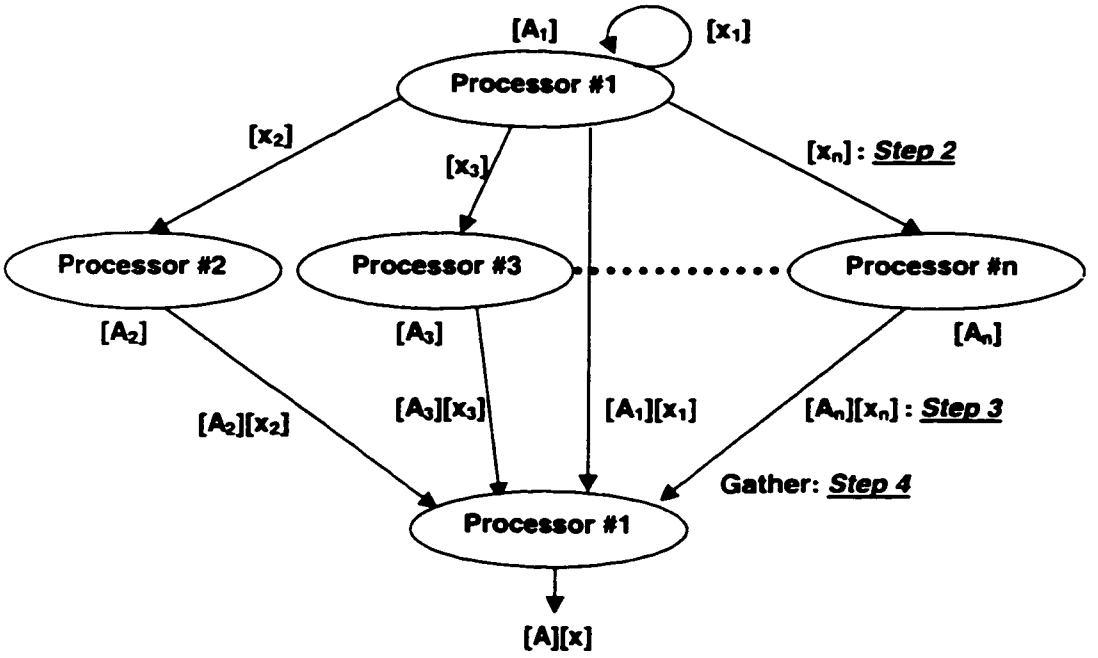

(b)

Figure 4.10: Matrix-Decomposition and Matrix-Vector Multiplication: Scheme II, where $[A] = \bigcup_{i=1}^{N}[A_i]$ and $[x] = \bigcup_{i=1}^{N}[x_i]$, (a) Step 1 - generate a partial linear system in each processor. (b) Matrix-vector multiplication ($[\mathbf{A}] \cdot [\mathbf{x}]$), Step 2 - send renewed $[x_i]$ which is banded to a partial linear system, Step 3 - perform partial matrix-vector multiplication, Step 4 - gather the results and give the final result of $[\mathbf{A}] \cdot [\mathbf{x}]$.

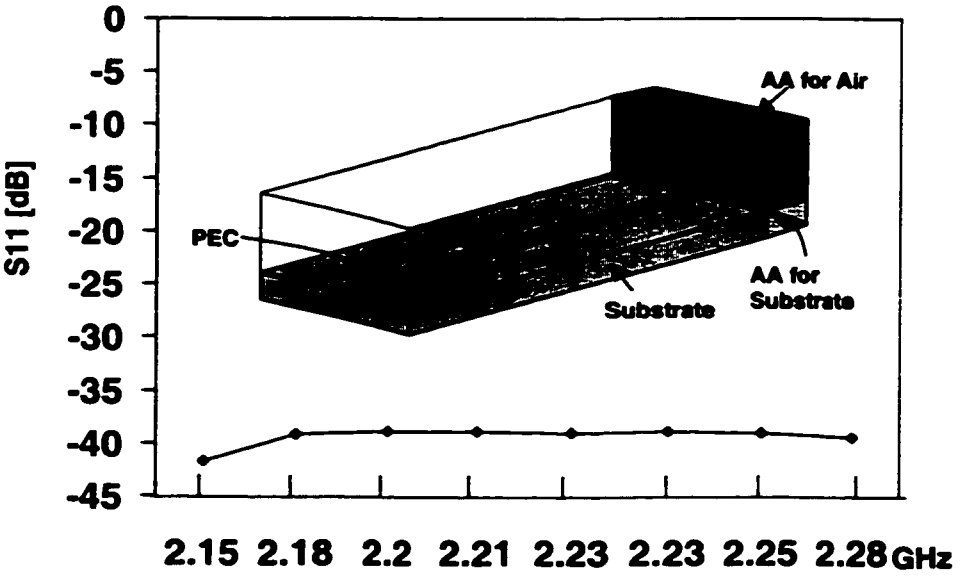

(a)

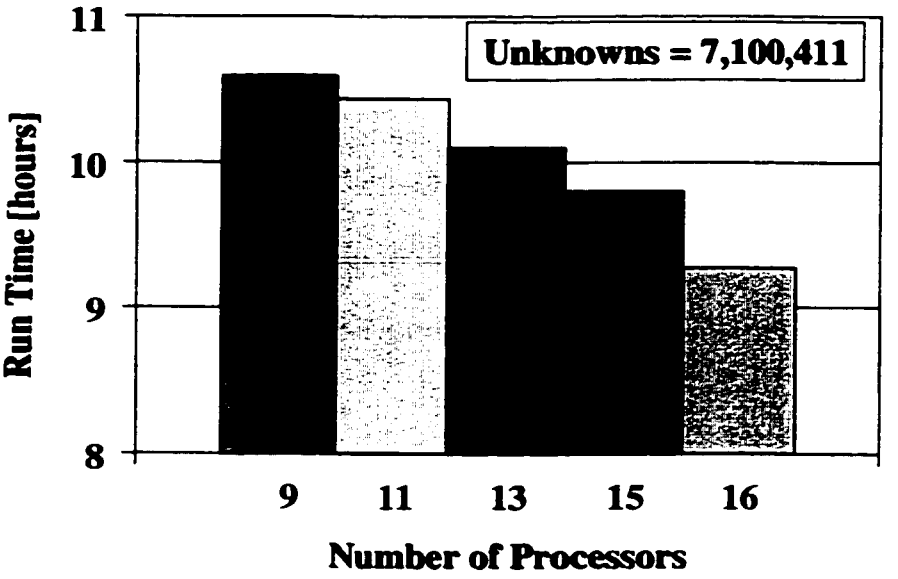

(b)

Figure 4.11: Example of matrix decomposition method : microstirp through line, ϵ_r for substrate = 2.54. ϵ_{AA} for substrate = 2.54 – j8, ϵ_{AA} for air = 1 – j5, substrate thickness = 1.6 mm, PEC width = 4.95 mm, grid = 67 × 211 × 85, total number of unknowns = 7,100,411. (a) schematic diagram and the computed return loss, (b) Performance measurement.

4.5 Task and Matrix Decomposition Method

Frequency parallelization, source parallelization, and the matrix decomposition method can be combined together to fully utilize their advantages simultaneously. As shown in Figure 4.12, sources and frequency points are processed serially in a processors group using matrix decomposition method. But they are processed in parallel as other source and frequency points are assigned to the rest processors groups. In this way, all available processors can perform large FEM computations for numerous frequency points.

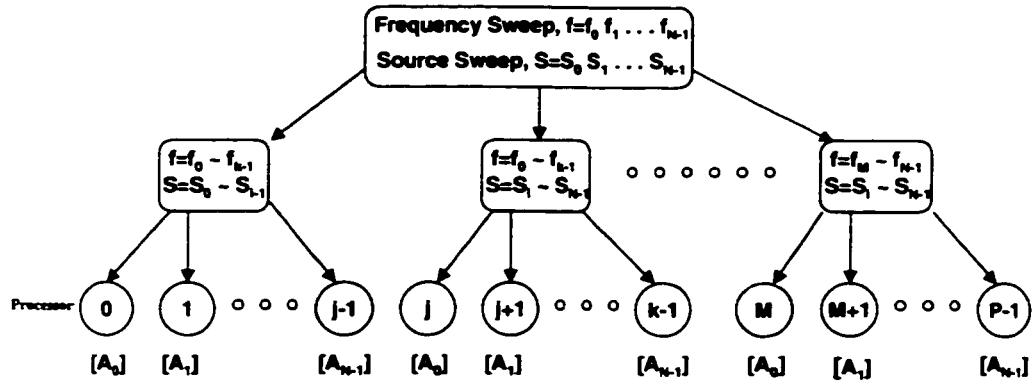

Figure 4.12: Combination of frequency and source parallelization and matrix decomposition method, where $[A] = \bigcup_{i=0}^{N-1}[A_i]$

4.6 MoM Task Parallelization

The dominant process in MoM computation is the computation of the impedance matrix elements, which is a series of numerical integrations of free space Green's function with bases in the MoM domain, as shown in Eqs.(2.14) – (2.17). Mathematically, these numerical integrations are not associated with each other and, therefore, can be carried out independently. For this reason, we apply task parallelization to speedup the MoM computations. Shown in Fig. 4.13 is the implementation of task parallelization scheme in MoM matrix generation. In the first stage, each processor generates a partial MoM matrix, $[Z_i]$ where i=0 $\cdots$ n-1 (stage 1). Then, the computed partial matrices are collected by the master processor to give a full MoM impedance matrix (stage 2). To achieve maximum speedup in MoM task parallelization, it is important to assign each processor a similar amount of computational tasks (number of matrix elements). Unlike the FEM case, MoM computation does not require a large independent memory for each processor. Thus, we can use both the no-shared and the shared memory type of machine in MoM parallel computation.

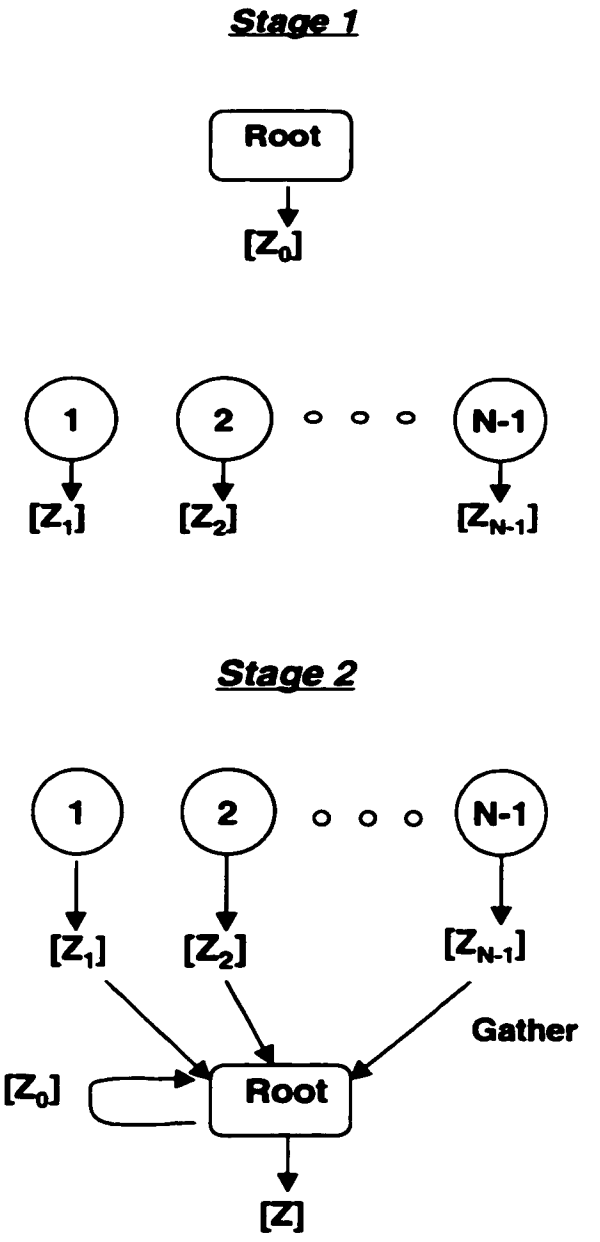

Figure 4.13: MoM task parallelization, where $[Z] = \bigcup_{i=0}^{N-1}[Z_i]$

CHAPTER V

VALIDATION

In this chapter we validate the hybrid MoM/FEM technique for aperture-coupled types of electromagnetic problems. As a validation model we have chosen a slot-coupled patch antenna with double layers, a widely known problem with an analytic solution. We first validate the developed hybrid MoM/FEM technique with this structure using scaling functions expanded on a patch and a slot. Second, we incorporate wavelets and explore its numerical strength. The microstrip feed region is discretized as is usual with tetrahedral elements for FEM computation. This discretization remains unchanged throughout all computations. We verify the computed results by comparing them with the measurement data [69]. In addition, threshold effects of a wavelet hybrid matrix and the savings in memory are closely examined.

5.1 Scaling Function Expansion (Zero Level Expansion)

Fig. 5.1 shows a double-layered slot-coupled microstrip patch antenna system proposed by Pozar [70]. A radiating patch and a microstrip feedline are printed on the top and bottom substrate, respectively, while a ground plane with a small nonresonant aperture is placed between them. The electromagnetic field is fed by the microstrip feeding line and coupled to the patch antenna through the aperture in the ground plane.

To expand electric currents on the patch and magnetic currents on the slot, we have used roof-top scaling functions on the patch in x and y directions and horizontally on the slot along the aperture (x direction). It is reasonable to consider the variation of magnetic current only in the longitudinal direction of the aperture because the width of an aperture is much narrower than the guided wavelength near resonant frequency. In the application of multi-resolution analysis (MRA) theory, the highest resolution of mesh is used in this scaling-function-only expansion (zero level expansion), while other lower resolutions of mesh are used in expanding scaling functions and wavelets (first and second level expansions), as shown in Fig. 5.2. Using a roof-top scaling function expansion in the highest resolution of mesh on a patch and a slot, a MoM solution is computed utilizing the available free space Green's functions. The microstrip feeding domain, on the other hand, is discretized with vector tetrahedral elements and solved by FEM. We have expanded equivalent magnetic currents on a slot in FEM domain with roof-top scaling functions. The final solution of this problem is obtained by combining the MoM and FEM solution and solving the combined equation as described in Chapter II.

We have calculated the input impedance of the circuit (Fig. 5.1) utilizing the solution according to the method shown in Appendix A. The results show good agreement with the measurement data over the computed frequency range (Fig. 5.3). Additionally, we have shown the radiating electric field and the current distribution on a patch in Fig. 5.4.

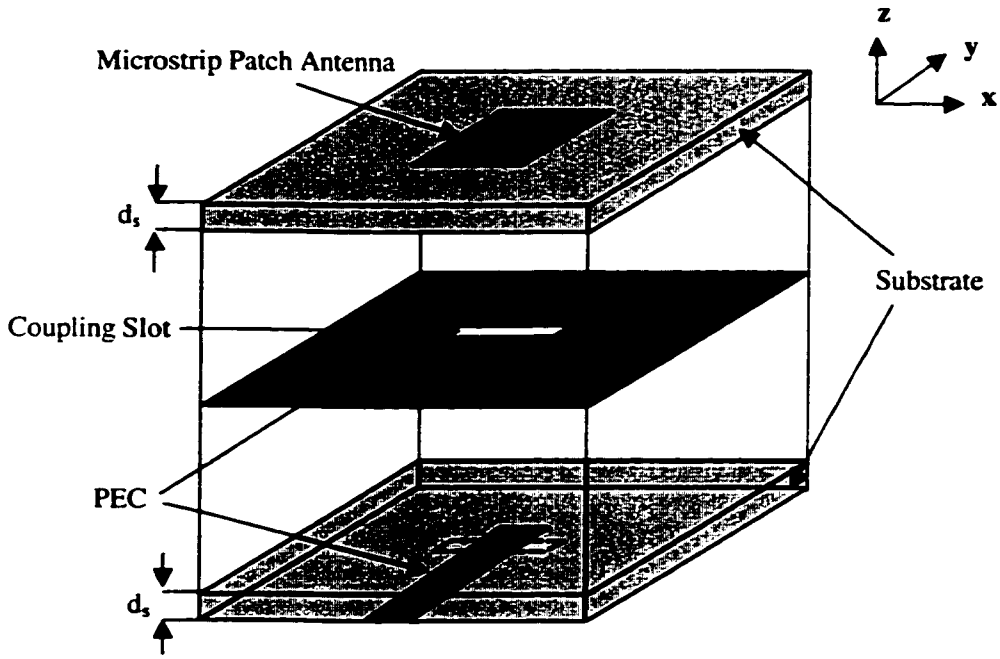

(a)

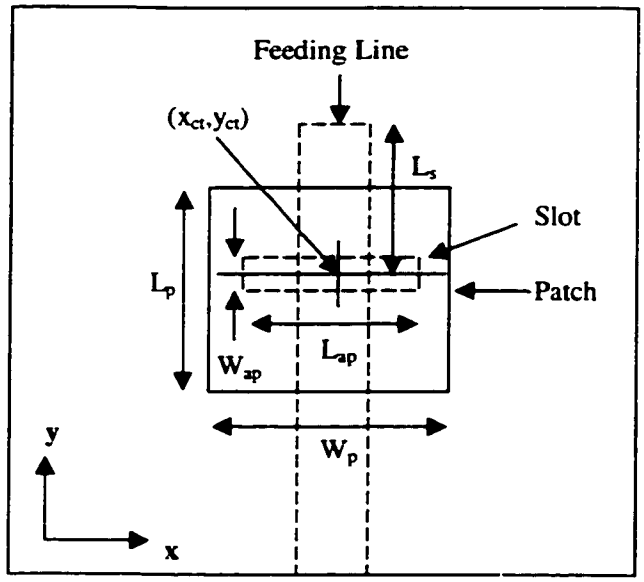

(b)

Figure 5.1: A Double-Layered Slot-Coupled Microstrip Patch Antenna System (a) Schematic view (b) Top view : $d_s = 0.16cm$, $L_p = 4.0cm$, $W_p = 3.0cm$, $x_{ct} = 0.0cm$, $y_{ct} = 0.0cm$, $L_{ap} = 1.12cm$, $W_{ap} = 0.155cm$, $L_s = 2.0cm$. Feeding line width $= 0.442cm$, Dielectric constant $= 2.54$.

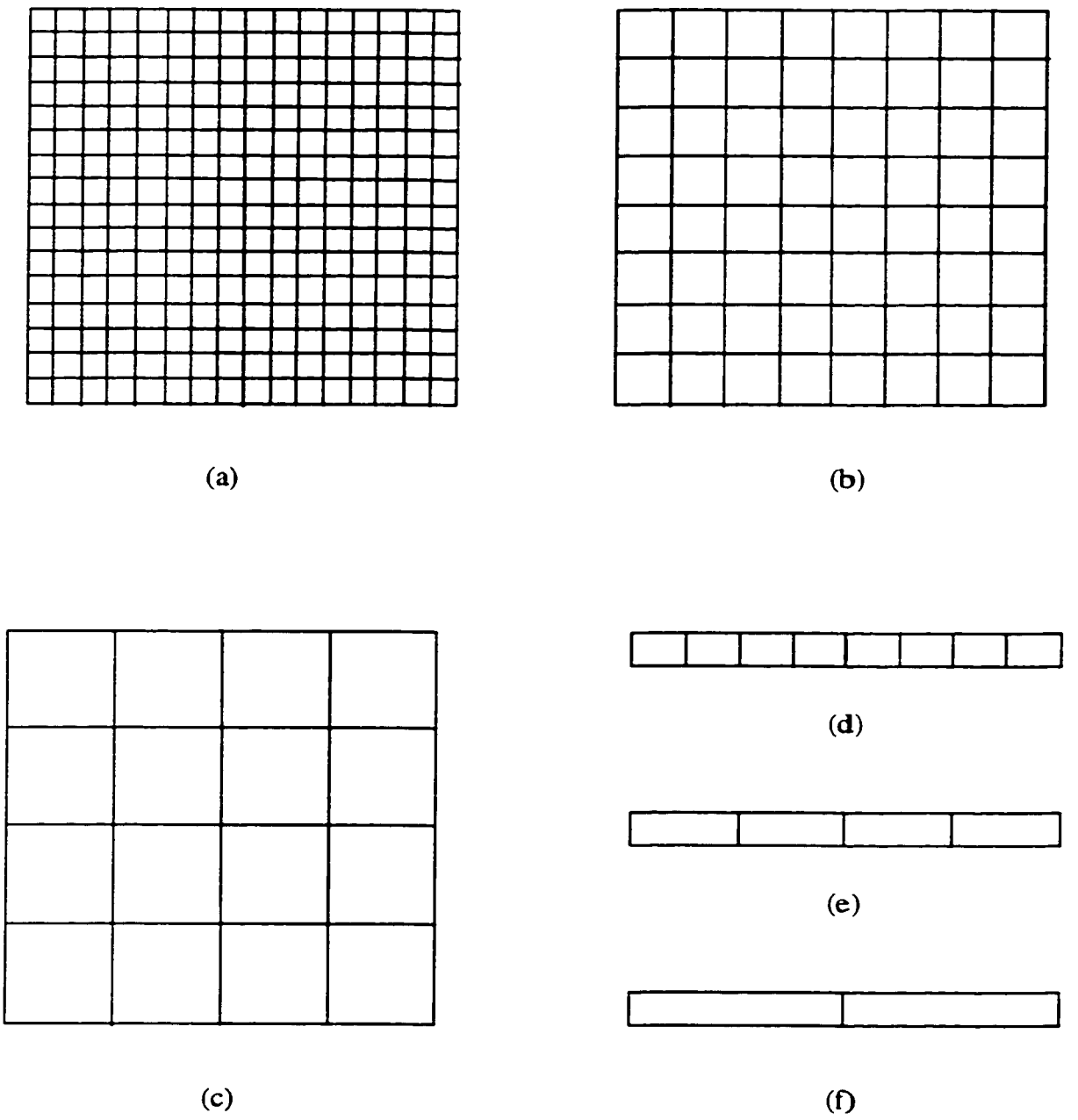

Figure 5.2: An example of multi-resolution meshing scheme on a patch and a slot. **Patch** : (a) Zero level grid – scaling functions only, (b) First level grid – scaling functions and wavelets, (c) Second level grid – scaling functions and wavelets. **Slot** : (d) Zero level grid – scaling functions only, (e) First level grid – scaling functions and wavelets, (f) Second level grid – scaling functions and wavelets.

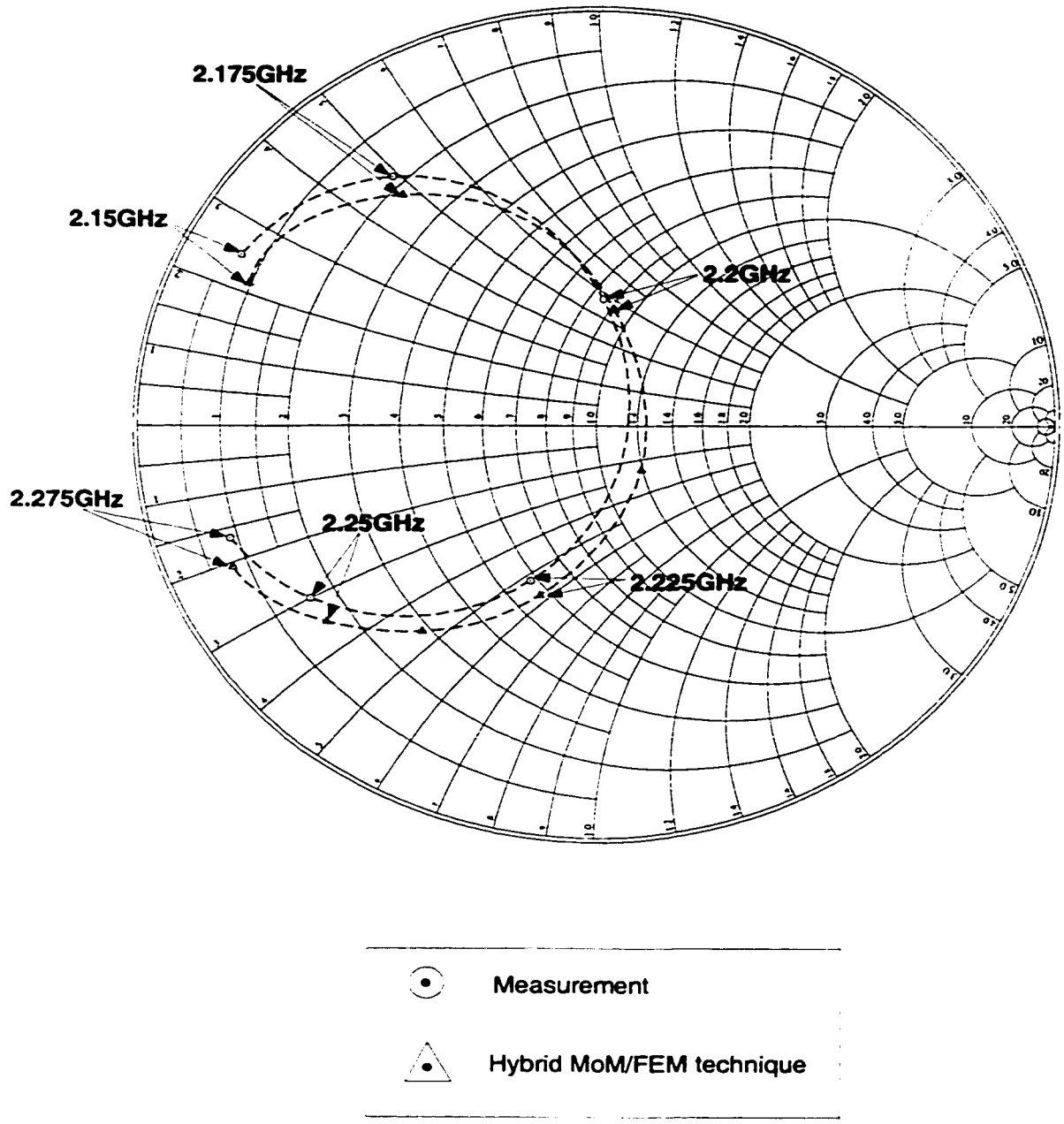

Figure 5.3: Input impedance of the patch antenna system - Zero level expansion

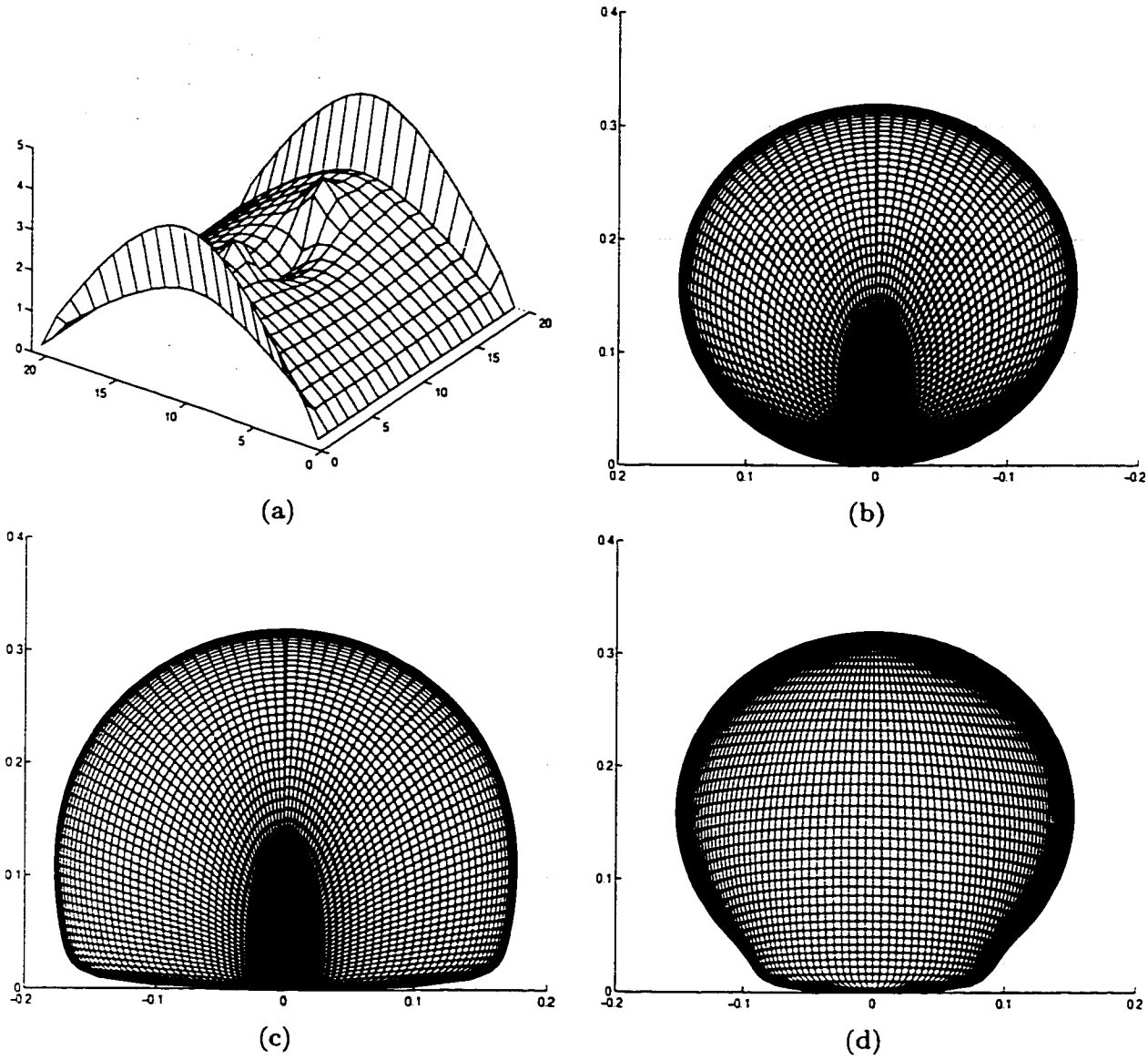

Figure 5.4: (a) Current distribution on a patch, Radiating electric field: (b) E_ϕ (observation angle : $\phi = 180^o$, $\theta = 0^o$), (c) E_θ (observation angle : $\phi = 90^o$, $\theta = 0^o$), (d) E_{total} (observation angle : $\phi = 0^o$, $\theta = 0^o$).

5.2 Scaling Functions and Wavelets Expansion

In this section, we verify the integration of MRA theory into the hybrid method with the same geometry used in the previous section (Fig. 5.1). The patch antenna and the coupling aperture are now modeled using scaling and wavelet bases while the microstrip feeding line is discretized with tetrahedral elements as before. We have considered two different expansions of the zero level scaling function space, using multi-resolution analysis. One is first level expansion, which gives scaling functions and wavelets in the first level grid – Fig. 5.2 (b), (e). The other is second level expansion, which gives wavelets in the first level grid - Fig. 5.2 (b) and (e), and scaling functions and wavelets in the second level grid - Fig. 5.2 (c) and (f). In both cases, the resolution levels are equal to zero level scaling-only expansion according to MRA theory. Figure 5.5 shows the equivalence of all these expansions along with their respective calculated input impedances.

In the following sections, a slot-coupled antenna patch problem is thoroughly studied with first and second level expansions. Specifically, we present in detail the effect on the numerical solutions caused by thresholding the hybrid linear system and the resulting saving in memory.

5.2.1 First Level Expansion

As mentioned previously, first level expansion produces scaling functions and wavelets in a first level grid. We have expanded the electric currents on a patch and the equivalent magnetic current on a slot with these basis sets and solved the problem (Fig. 5.5) using the hybrid MoM/FEM method. The discretization of the microstrip feeding region remains unchanged with the same vector tetrahedral elements as before.

We have computed the single patch antenna problem (Fig. 5.5) with various threshold levels and closely examined its effect on the accuracy of the solutions. As mentioned in Chapter III, thresholding is performed locally for each sub-matrix in the hybrid MoM/FEM matrix by discarding small off-diagonal wavelet elements less than a certain fraction of the largest element. Figure 5.6 shows the calculated input impedance for different threshold levels from 10^{-5} to 6×10^{-5}. As one can see, input impedance is close to that of the exact solution when threshold tolerance is equal to or less than 10^{-5}. The input impedance starts to deviate as threshold tolerance is increased to 2×10^{-5}. At the tolerance of 6×10^{-5}, the input impedance becomes totally different from that of the exact solution. Therefore, for this single patch antenna problem, the threshold tolerance should not be greater than 10^{-5}. We have observed the variations of electric current distribution on a patch as we change the threshold tolerance. A one-dimensional view of electric current distribution across the center of a patch is shown in Fig. 5.7 for various threshold tolerances. Interestingly, as the tolerance increases from 2×10^{-5}, not only does the shape of the current change but also the amplitude of the current becomes small. This phenomenon can be more clearly observed in the two-dimensional view shown in Fig. 5.8. As the tolerance is changed up to 2×10^{-5}, there is not much variation in the shape of the current; it is only a little rough. An apparently different shape of the current, sharp and rough, appears at a tolerance of 6×10^{-5} and the current becomes unrecognizable at a tolerance of 4×10^{-4}, as shown in Figs. 5.8 (d) and (e), respectively. It is interesting to note that at the tolerance of 4×10^{-4} the overall shape of the current is mostly destroyed (Fig. 5.8) but the envelope of center current in Fig. 5.7 is similar to that of the exact solution except for smaller edges and magnitude. Lastly, we studied the effect of threshold on the radiation pattern of this patch antenna system. Figures 5.9,

5.10, and 5.11 show each radiating electric field component for different threshold levels. As expected, less electric field is radiating with the increment of threshold tolerance. This is because the edge electric currents on a patch, a major component that makes the radiating electric field, become smaller as the threshold tolerance is increased, as shown in Fig. 5.7.

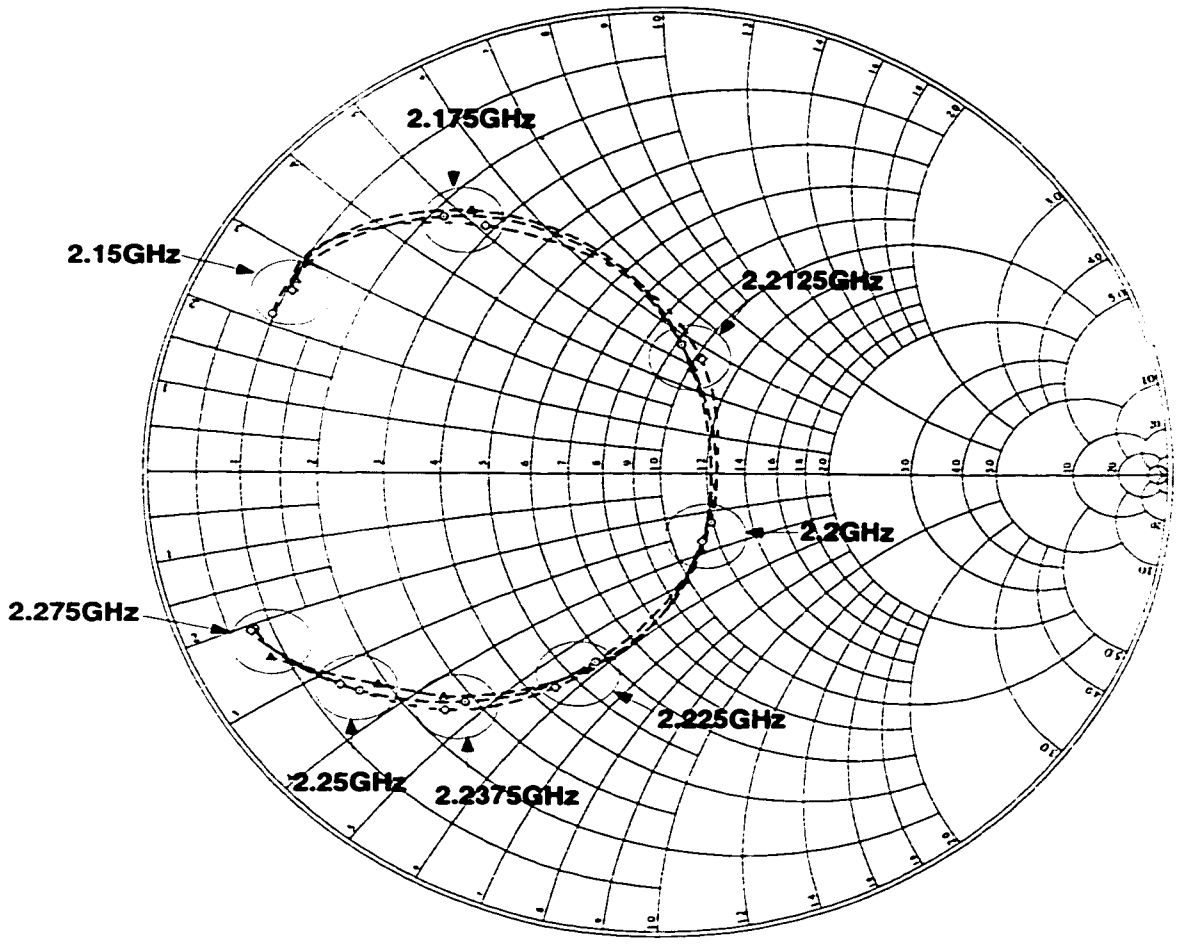

Figure 5.5: Input impedance of the patch antenna system for multi-level expansions

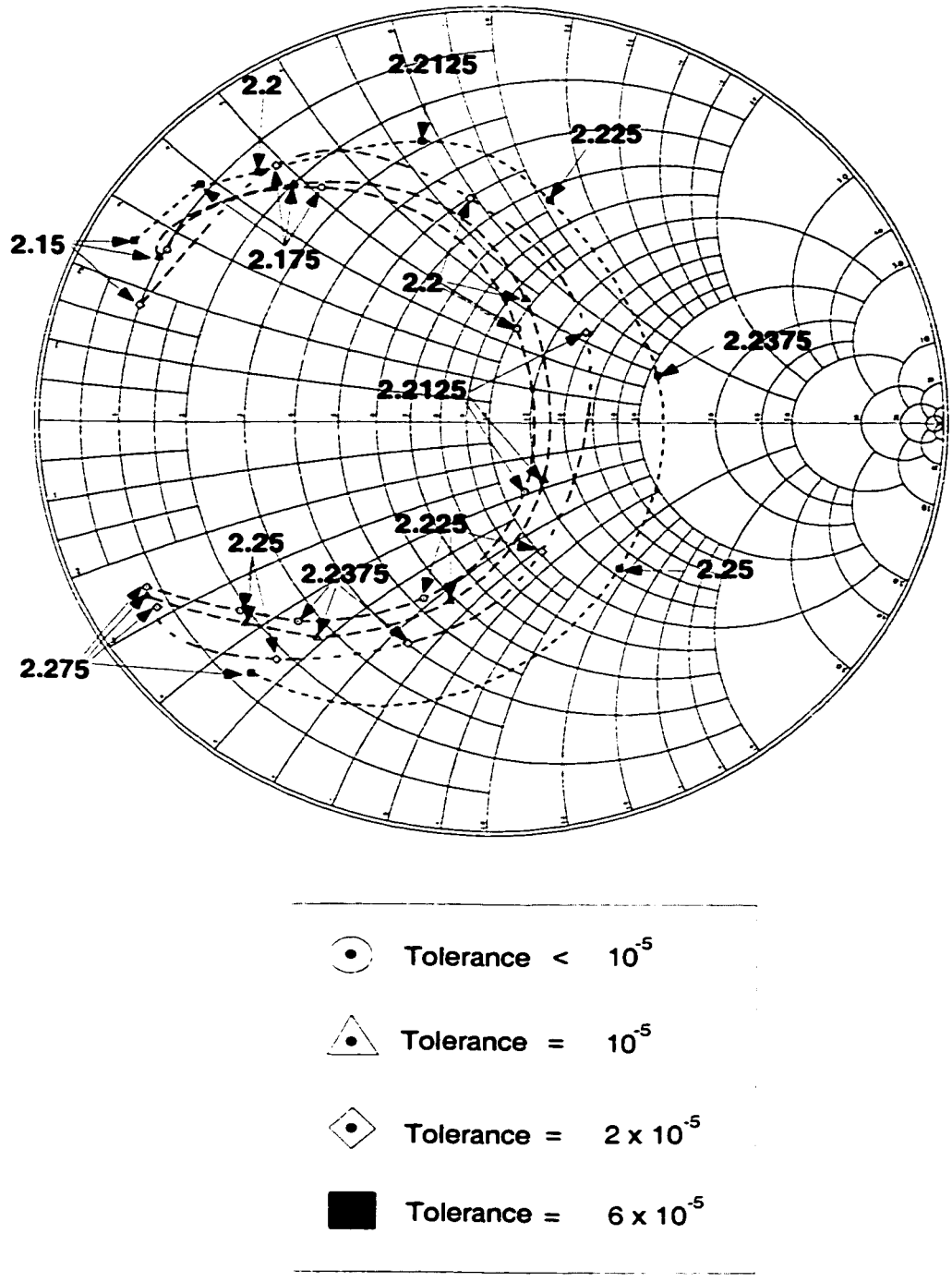

Figure 5.6: Input impedance of the patch antenna system for various threshold levels - First level expansion. (Numbers shown in the figure are frequency points in GHz)

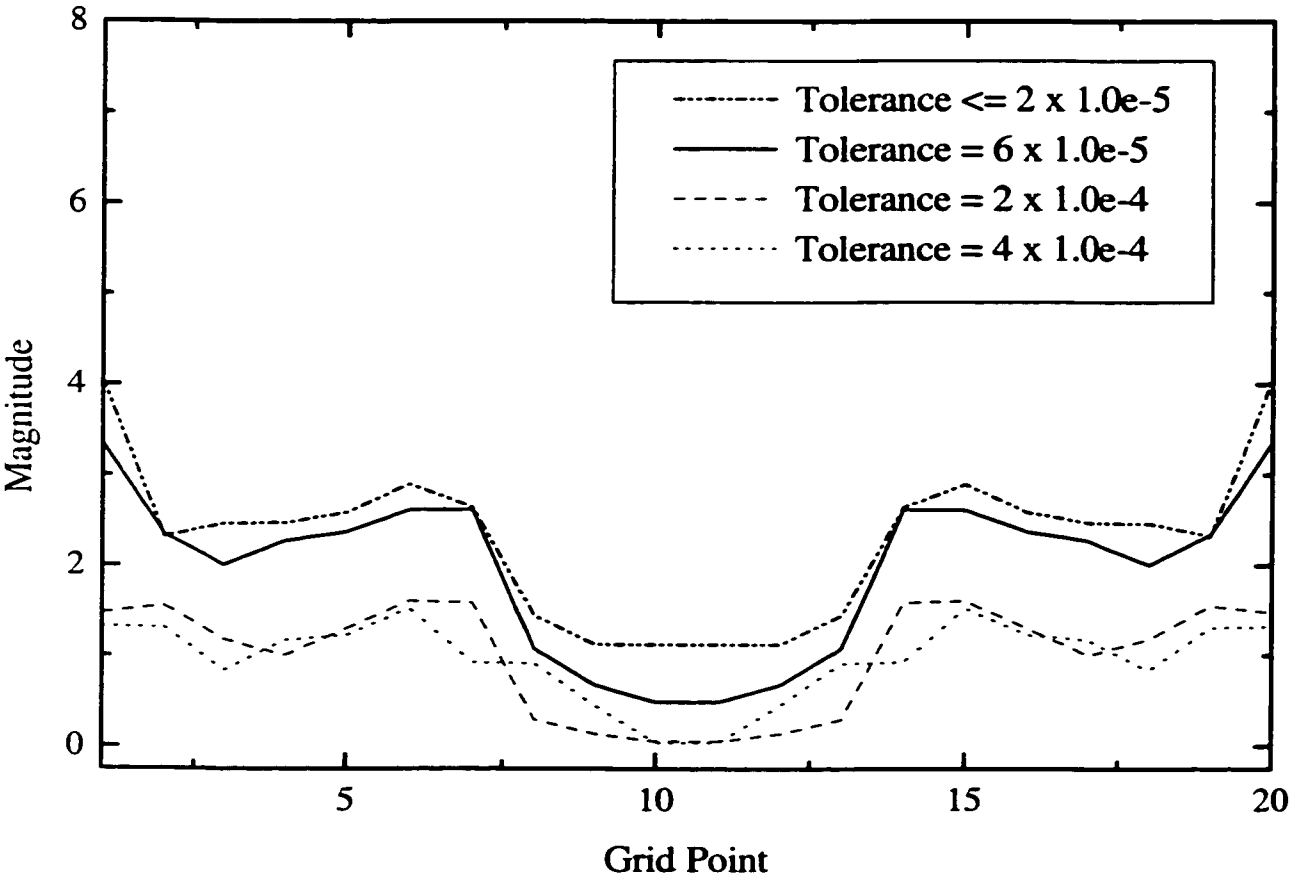

Figure 5.7: Current distribution across the center of a patch for various threshold levels - First level expansion

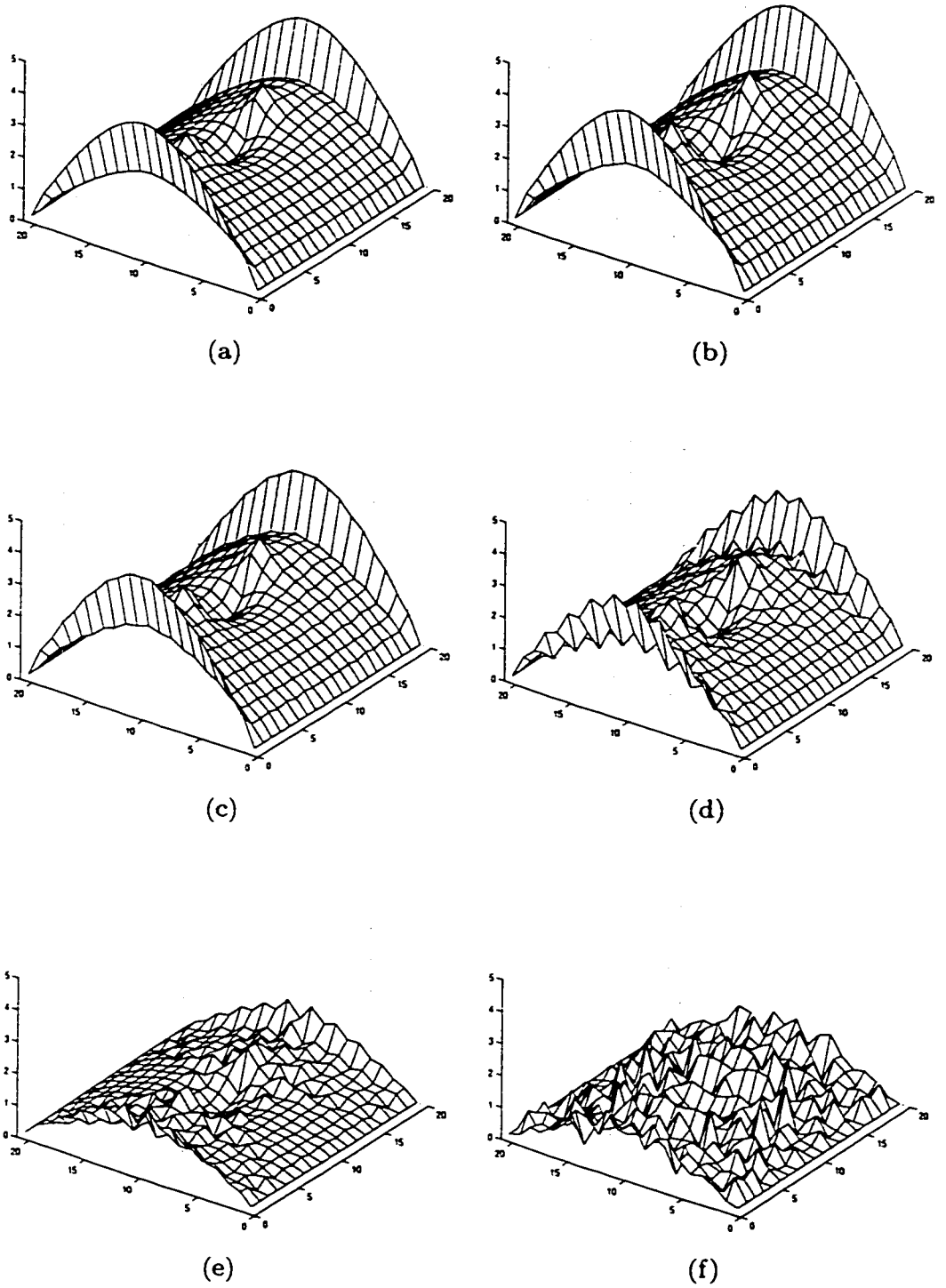

Figure 5.8: Current distribution on a patch for various threshold levels – First level expansion : (a) Tolerance $< 10^{-5}$, (b) Tolerance $= 10^{-5}$, (c) Tolerance $= 2\times10^{-5}$, (d) Tolerance $= 6\times10^{-5}$, (e) Tolerance $= 2\times10^{-4}$, (f) Tolerance $= 4\times10^{-4}$.

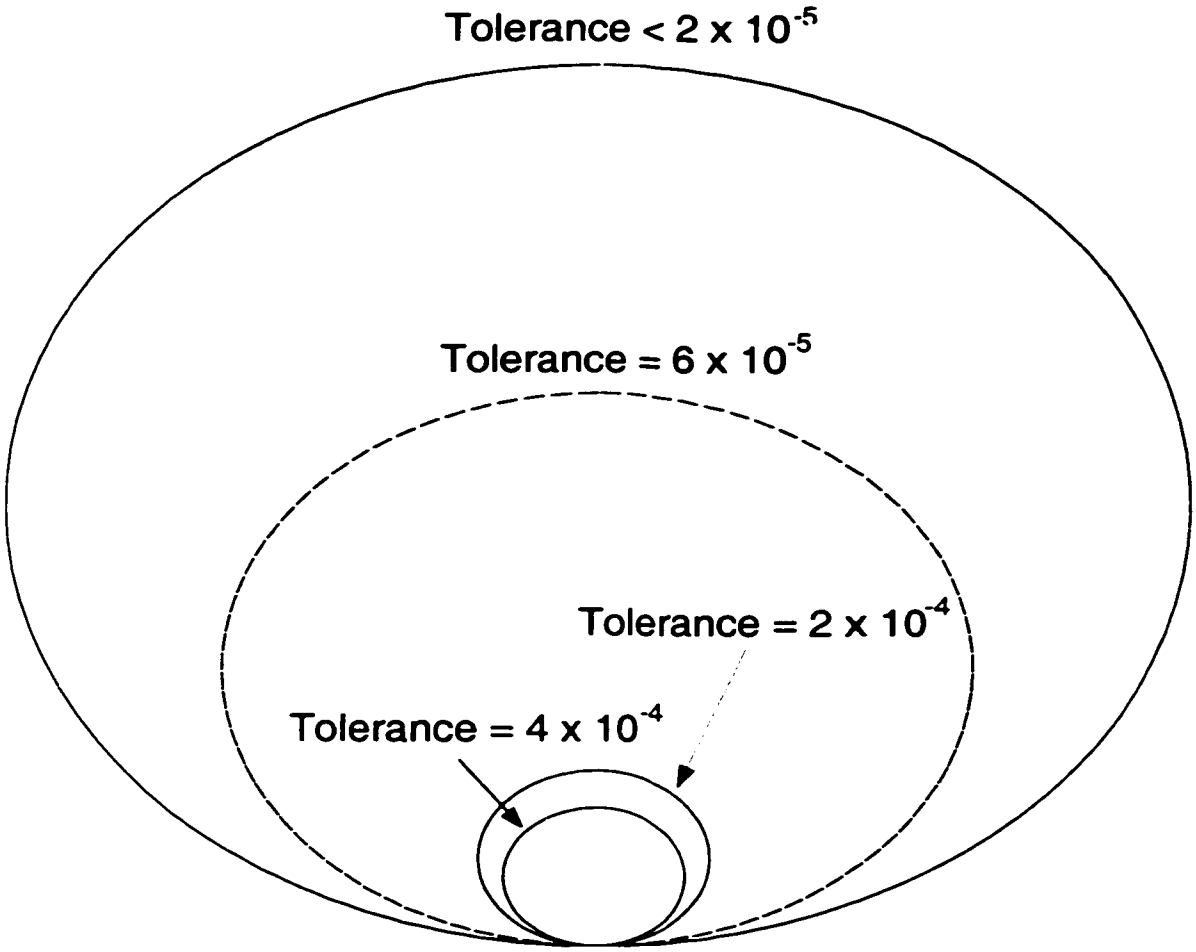

Figure 5.9: Radiating electric field, E_ϕ, for various threshold levels : Observation angle ($\phi = 180^o$, $\theta = 0^o$) – First level expansion.

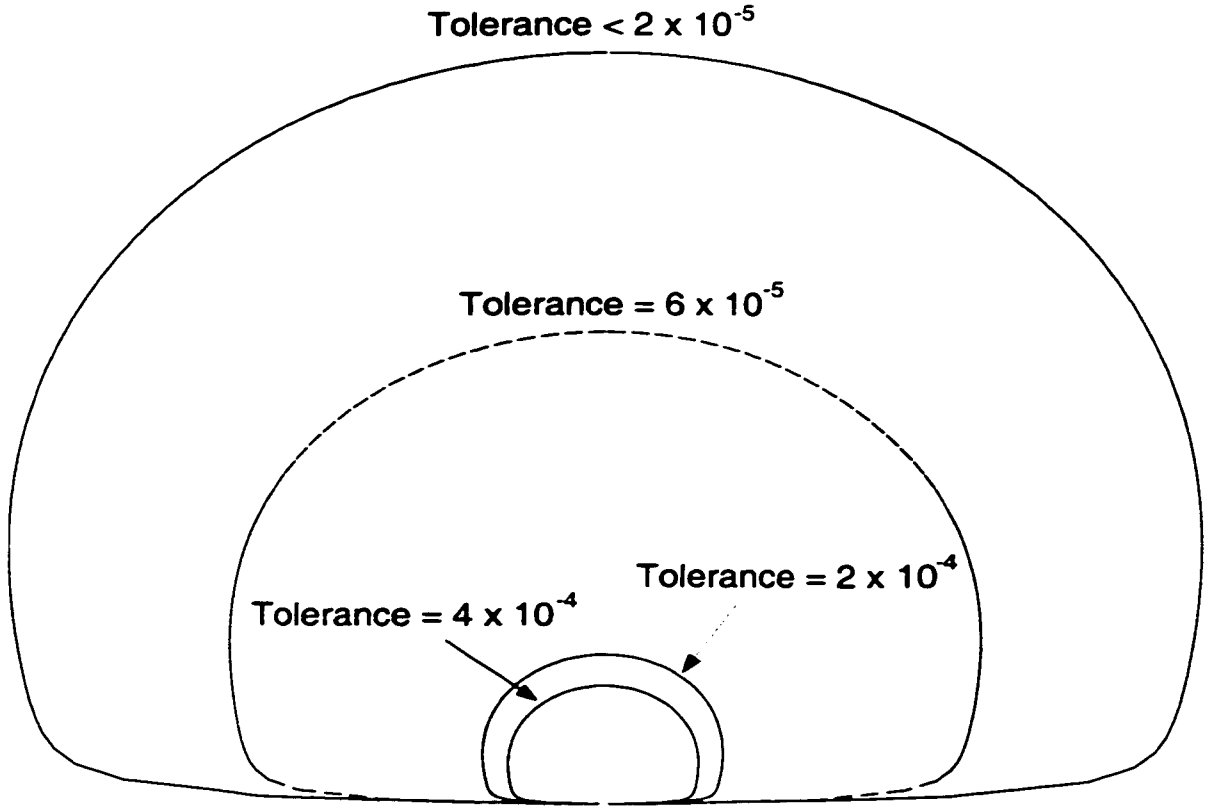

Figure 5.10: Radiating electric field, E_θ, for various threshold levels : Observation angle ($\phi = 90^o$, $\theta = 0^o$) – First level expansion.

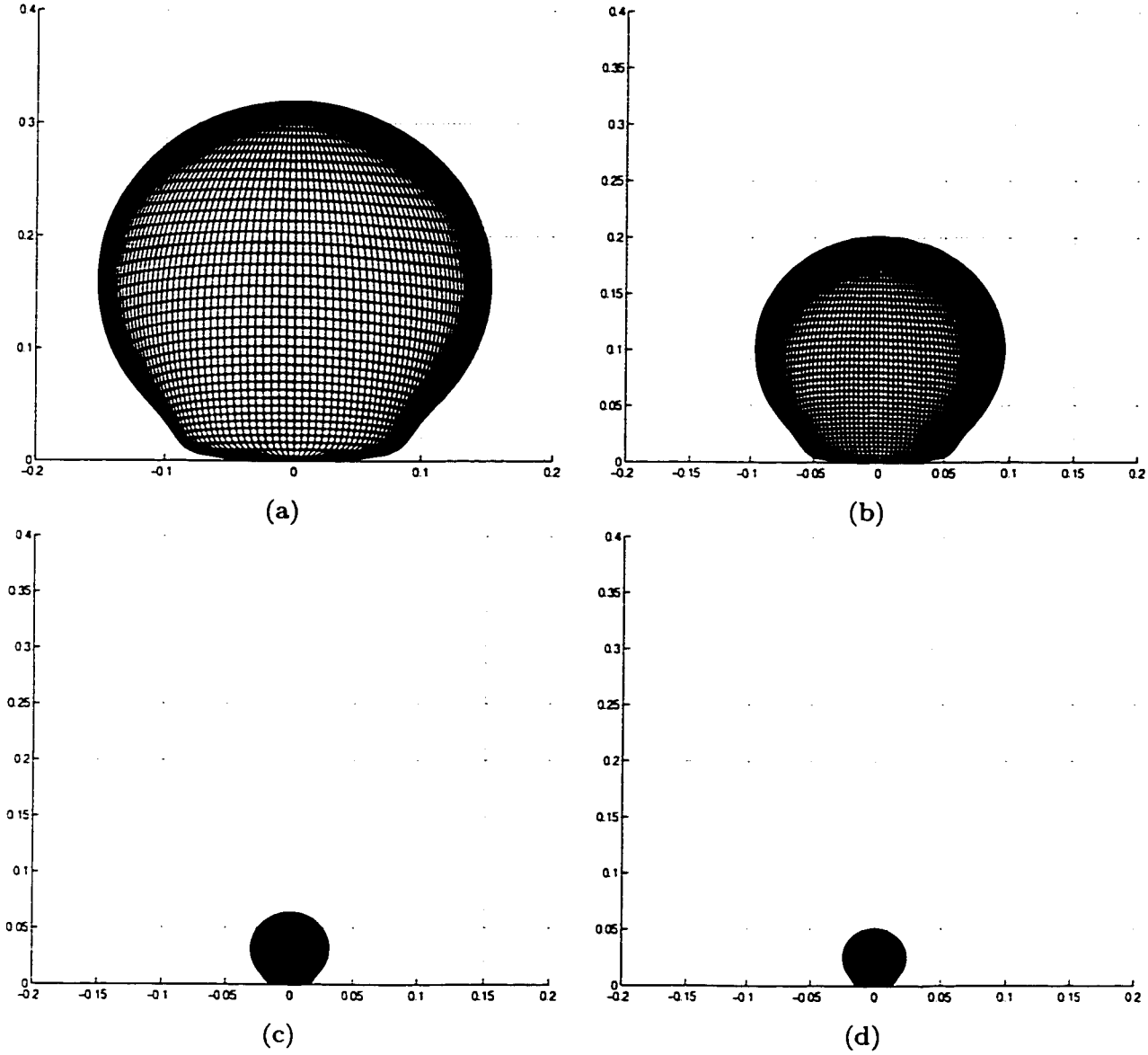

Figure 5.11: Radiating total electric field for various threshold levels – First level expansion : (a) Tolerance $< 2\times10^{-5}$, (b) Tolerance $= 6\times10^{-5}$, (c) Tolerance $= 2\times10^{-4}$. (d) Tolerance $= 4\times10^{-4}$. Observed at $\phi = 0^o$, $\theta = 0^o$.

5.2.2 Second Level Expansion

The second level expansion of zero level scaling function space (wavelets in the first level grid, and scaling functions and wavelets in the second level grid) can be used to model electric and magnetic current on a patch and slot, respectively, with the same tetrahedron mesh in the microstrip feed region as before. In this expansion, we can make the hybrid linear system more sparse than the previous first level expansion. This is possible because the resulting hybrid linear system has more wavelet terms (whose values are much smaller than other terms and can be treated as zero) than other linear systems generated by the previous two expansions. In other words, this process, called matrix diagonalization, concentrates most of the system's information near diagonal scaling function terms, making the hybrid linear system compact and sparse. We have shown the sparse hybrid linear systems and investigated the threshold effects on the numerical solutions of the hybrid MoM/FEM method.

Figure 5.12 shows the computed input impedance of a single patch antenna system (Fig. 5.1) for three threshold levels. As one can see, the input impedance does not change up to the tolerance of 5×10^{-5}, but it becomes very different as the tolerance increases to 5×10^{-4}. The same trend of threshold effect is observed in the cross-section view of the electric current distribution shown in Fig. 5.13; it does not change much below the tolerance of 5×10^{-5} but becomes very different beyond the tolerance of 5×10^{-4}. Shown in Fig. 5.14 is the two-dimensional distribution of electric current on a patch for different threshold levels. The changes of the current distribution with respect to the threshold level are similar to that of first level expansion (Fig 5.14). However, they have a different numerical property coming from different expansions of scaling functions and wavelets. For example, the current

distribution in Fig. 5.14 (b), second level expansion with tolerance of 5×10^{-5}. and in Fig. 5.8, first level expansion with tolerance of 6×10^{-5}, are very similar to each other. But they give different input impedance; the former's is correct (Fig. 5.12) and the latter's is incorrect (Fig. 5.6). This difference is attributed to the higher diagonalization of the hybrid linear system by additional wavelets in the second level expansion. To put it differently, the system information is more concentrated in near diagonal scaling function terms for a higher-level expansion. As a result, the solution of a higher-level expansion is relatively less affected by threshold value than that of a lower-level expansion. Shown in Figs. 5.15 – 5.17 are radiating electric field patterns in each component for various threshold levels. As we have observed in the case of first level expansion, the strength of all radiating field components is reduced as the threshold tolerance is increased. Similar to the variation of the input impedance with respect to the threshold tolerance, the radiation pattern remains unchanged at the tolerance of 5×10^{-5} but is significantly reduced when the tolerance becomes larger than 5×10^{-4}. Figures 5.18 (a) and (b) show the resulting sparse matrices for the threshold tolerance of 5×10^{-5} and 10^{-2}, respectively. Surprisingly, the sparsity reached to 73.7% with the tolerance of 5×10^{-5}. This means that, with this value of threshold, we can solve the problem exactly using only 26.7% of the memory required in an ordinarily MoM computation. To observe the change of sparsity in further case, we performed threshold with tolerance of 10^{-2} and presented a resulting matrix having 95.87% of sparsity, even though the numerical results in this range of threshold tolerance are not correct and, indeed, are unacceptable. Because of the non-symmetric nature of the hybrid matrix, as can be noticed in Fig. 5.18, only a CG (conjugate gradient) type of iterative solver [66] can be used as a solution routine of the hybrid matrix.

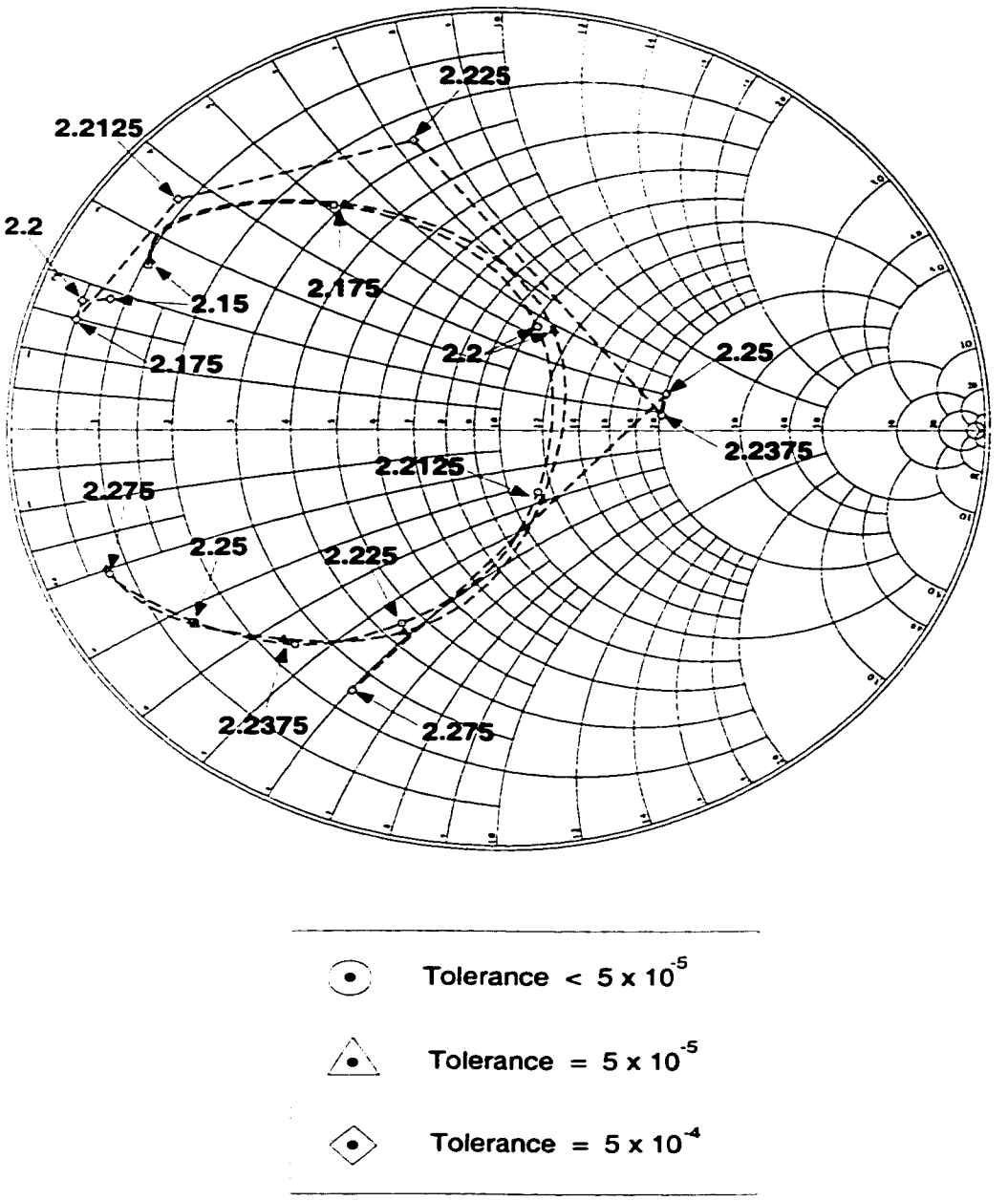

Figure 5.12: Input impedance of the patch antenna system for various threshold levels – Second level expansions. (Numbers shown in the figure are frequency points in GHz)

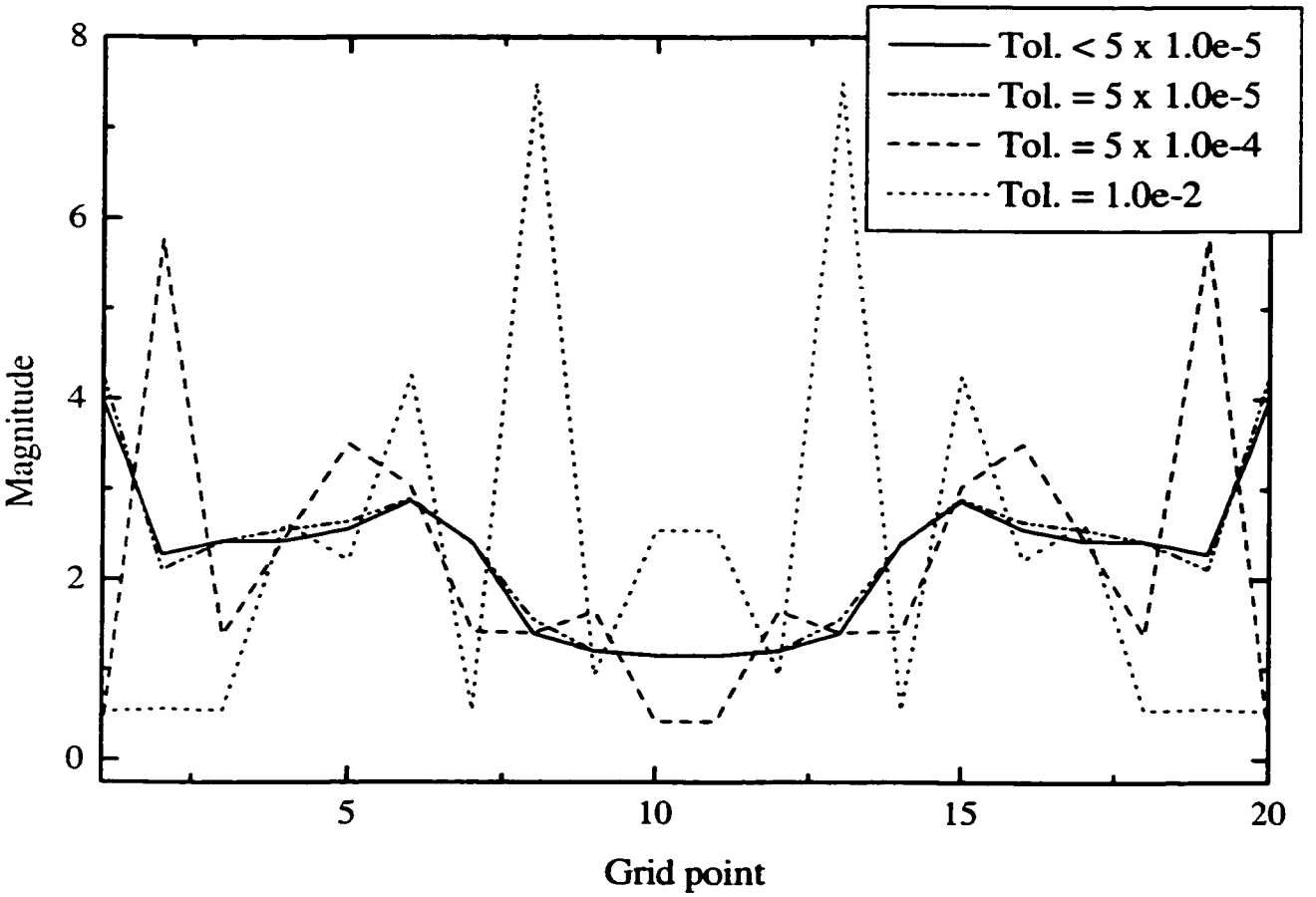

Figure 5.13: Current distribution across the center of a patch for various threshold levels – Second level expansion

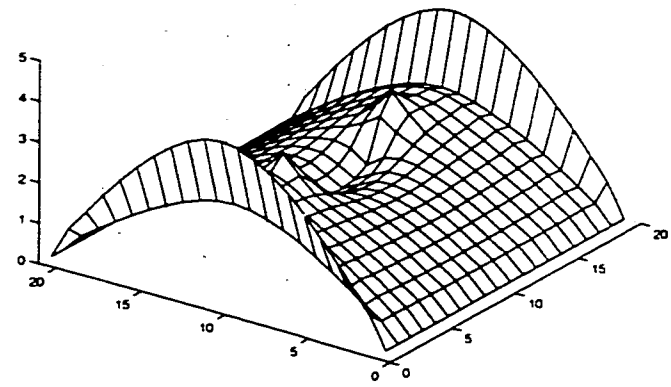

(a)

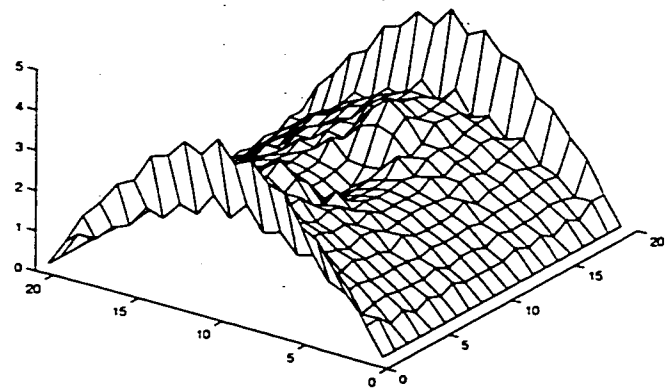

(b)

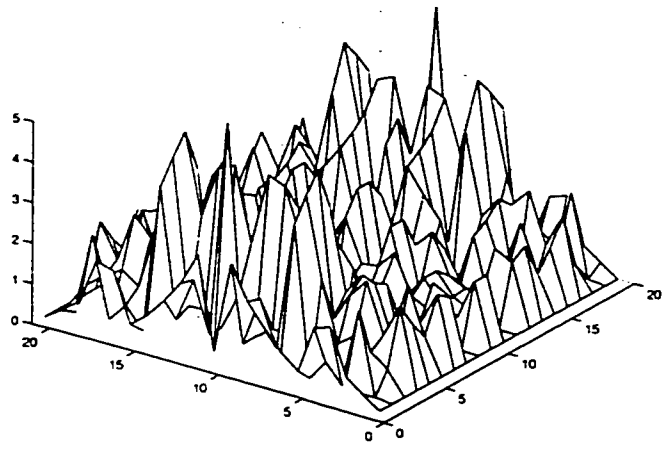

(c)

Figure 5.14: Current distribution on a patch for various threshold levels – Second level expansion : (a) Tolerance $< 5\times10^{-5}$, (b) Tolerance $= 5\times10^{-5}$, (c) Tolerance $= 5\times10^{-4}$.

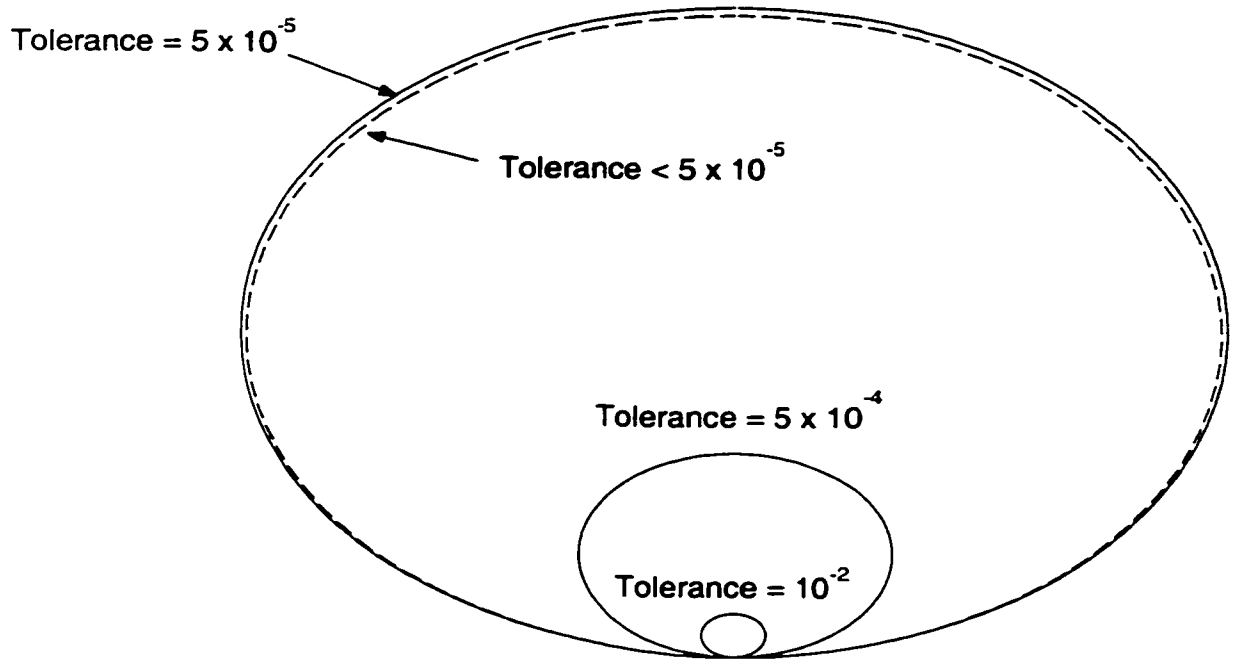

Figure 5.15: Radiating electric field, E_θ, for different threshold levels : Observation angle ($\phi = 180^o$, $\theta = 0^o$) – Second level expansion.

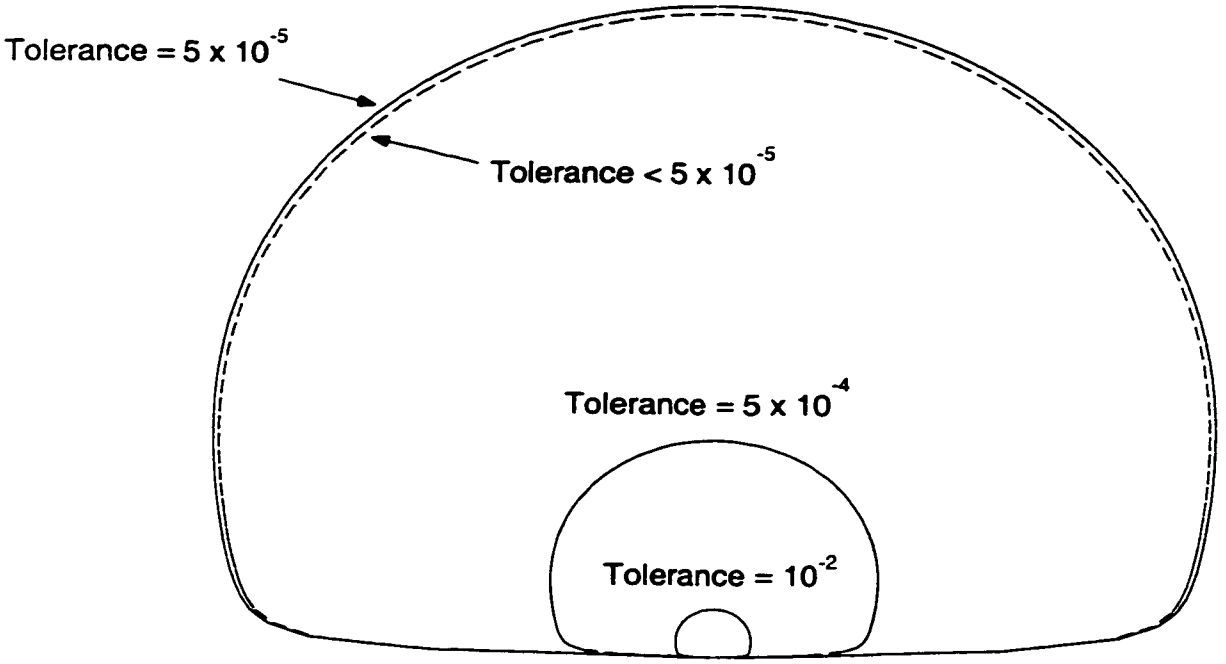

Figure 5.16: Radiating electric field, E_ϕ, for different threshold levels : Observation angle ($\phi = 90°$, $\theta = 0°$) - Second level expansion.

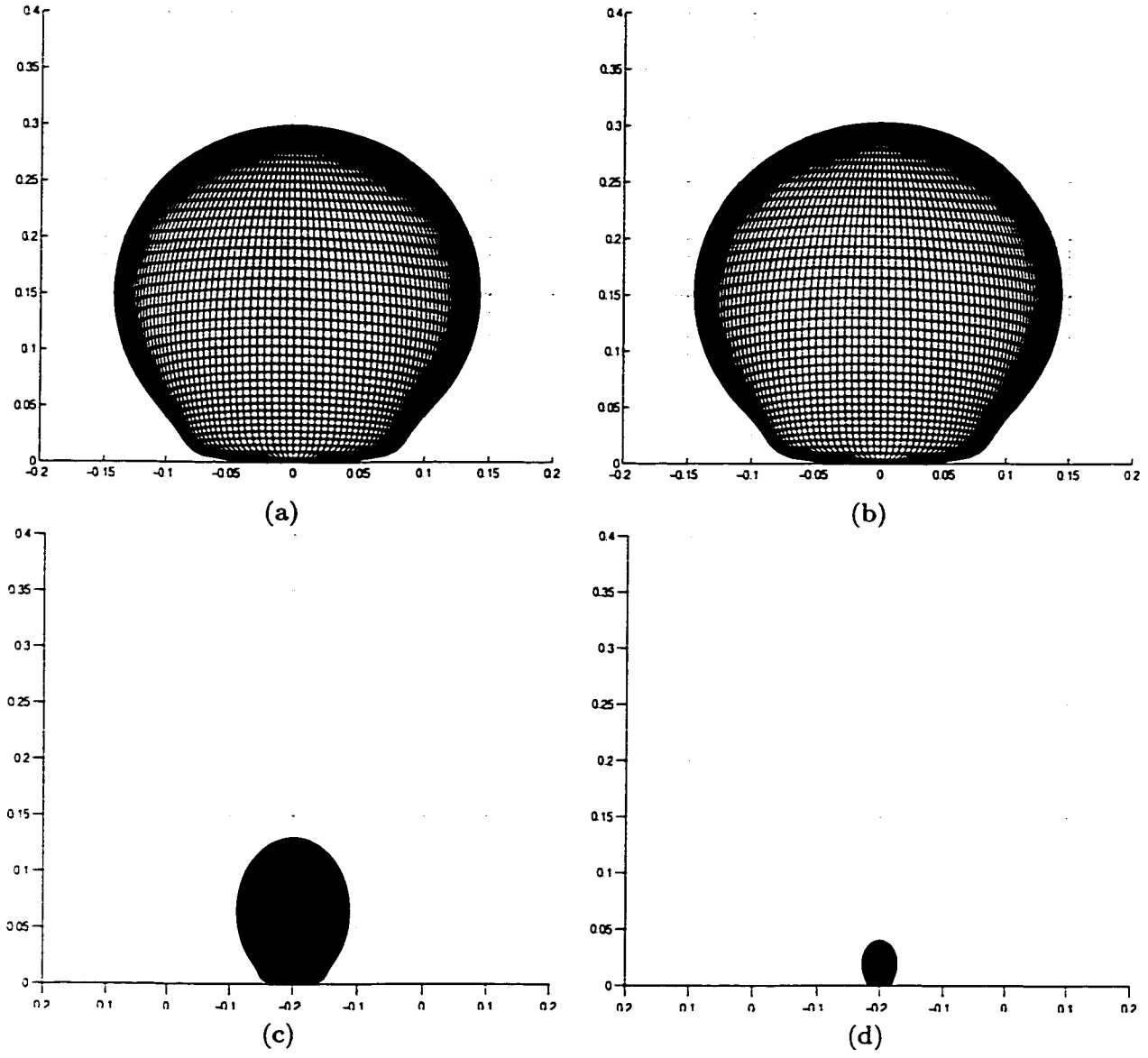

Figure 5.17: Radiating total electric field, E_{total}, for different threshold levels – Second level expansion: (a) Tolerance $< 5\times10^{-5}$, (b) Tolerance $= 5\times10^{-5}$, (c) Tolerance $= 5\times10^{-4}$, (d) Tolerance $= 10^{-2}$.

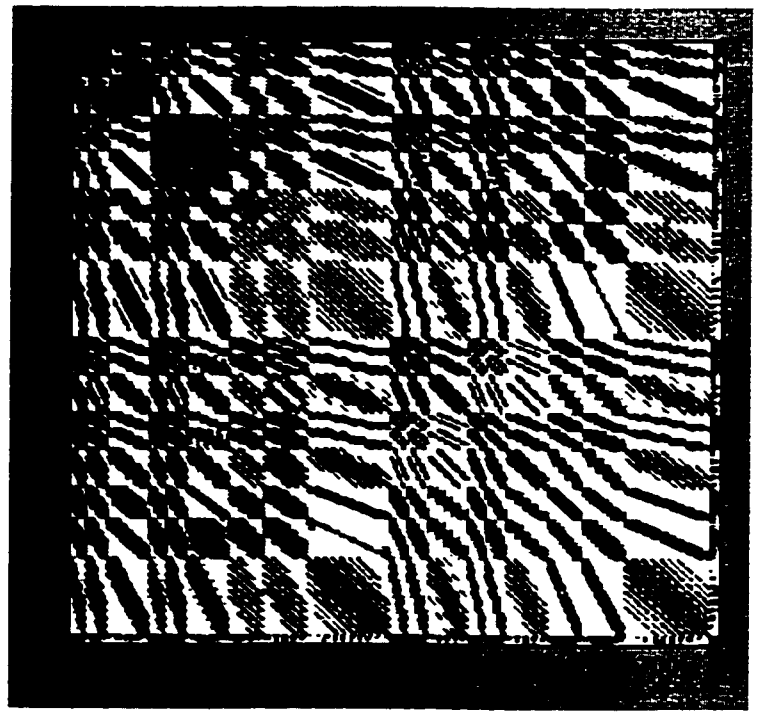

(a)

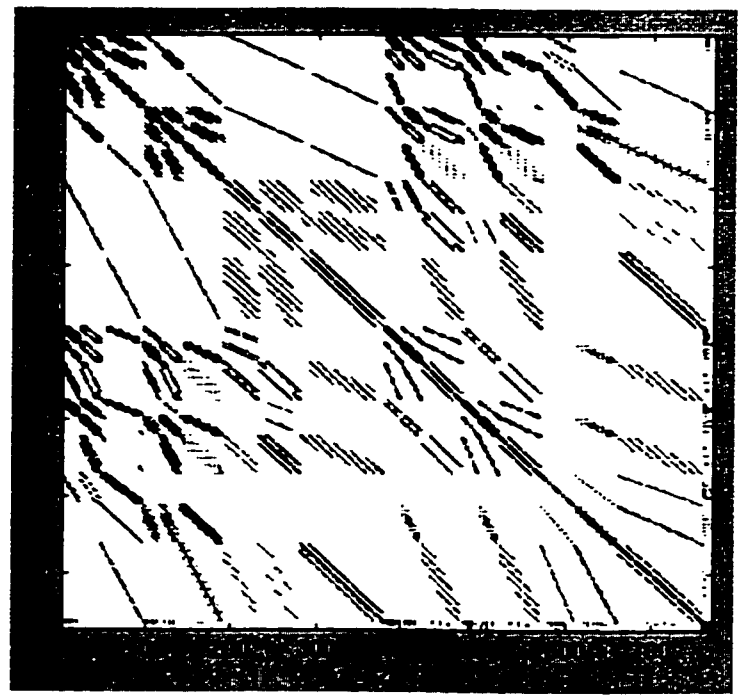

(b)

Figure 5.18: Sparsity of the hybrid matrix – Second level expansion : (a) 73.6984 % of sparsity with tolerance of 5×10^{-5}, (b) 95.8771 % of sparsity with tolerance of 10^{-2}.

CHAPTER VI

APPLICATION

Having verified the developed hybrid method along with its wavelet application, we now apply this method to a large-scale electromagnetic problem, specifically a 4×8 patch antenna array system. In this application, we numerically solve the array problem by integrating all three techniques and characterize the electromagnetic performance of the array system. This work includes: (1) multi-level expansions of scaling functions and wavelets on an array of patch and slot; (2) the use of parallel computing to supply the large memory required and carry out heavy computations. We present numerical results of this problem, including the return loss, the current distribution, the magnetic field distribution over the feeding network and the radiation pattern of the antenna array. Lastly, we discuss the threshold effect on the numerical solution of the problem in multi-level wavelet expansions and its resulting numerical features in detail.

6.1 4×8 Patch Antenna Array System

The hybrid MoM/FEM method, wavelet, and HPC are applied to an aperture coupled 4×8 patch antenna array system as shown in Fig. 6.1. To investigate a numerical feature of multi-level wavelet expansion the problem is solved with three different basis expansions on patches and apertures: (1) zero level scaling-only ex-

pansion; (2) first level expansion (scaling functions and wavelets in first level grid); and (3) second level expansion (wavelets in first level grid, and scaling functions and wavelets in second level grid). Bases are expanded in both horizontal and perpendicular directions on patches, whereas we place bases for aperture only horizontally along the aperture, as before. The microstrip feeding network is again discretized with tetrahedron. A total of 1.7 million unknowns are generated in this problem and 99% of unknowns are located in the microstrip feeding network. The solution procedures are: (1) obtain the FEM solution in the feeding network domain and the MoM solution in the array antenna domain; (2) combine the FEM and MoM solutions; and (3) solve a combined hybrid equation.

All computations are performed on a distributed memory machine, IBM SP2 with 256M-Bytes of memory and 160MHz of clock speed. Task parallelization is used in MoM while task parallelization and domain decomposition method are used in FEM. The parallel MoM code shows about 50% of speedup with 32 processors on both the distributed and the shared memory machine. The parallel FEM code can solve problems on the order of 10^7 unknowns.

6.1.1 Scaling Function Expansion (Zero Level Expansion)

In a zero level expansion, using only scaling function on patches and slots, we calculated the current distribution on patch antenna array using Eq. (2.21) and plotted its result in Fig. 6.3. Figure 6.2 shows the total magnetic field distribution over the feeding network obtained by Eq. (A.1). The resonance of the system can be seen from the low standing wave ratio of the magnetic field in Fig. 6.3. Finally, the radiating total electric field from the 4×8 patch array is shown in Fig. 6.4. Note that in this scaling-only expansion a full hybrid matrix must be used for the solution

of the problem, which requires approximately 4G-Bytes of memory. We separately stored the full hybrid linear system in 16 nodes which have 256M-Bytes of memory in each, and solved it using the matrix-decomposition scheme mentioned in Chapter IV.

We computed a normalized reflection coefficient of the array system using Eq. (A.2) and presented it in Fig. 6.5 along with those from lower levels of resolution.

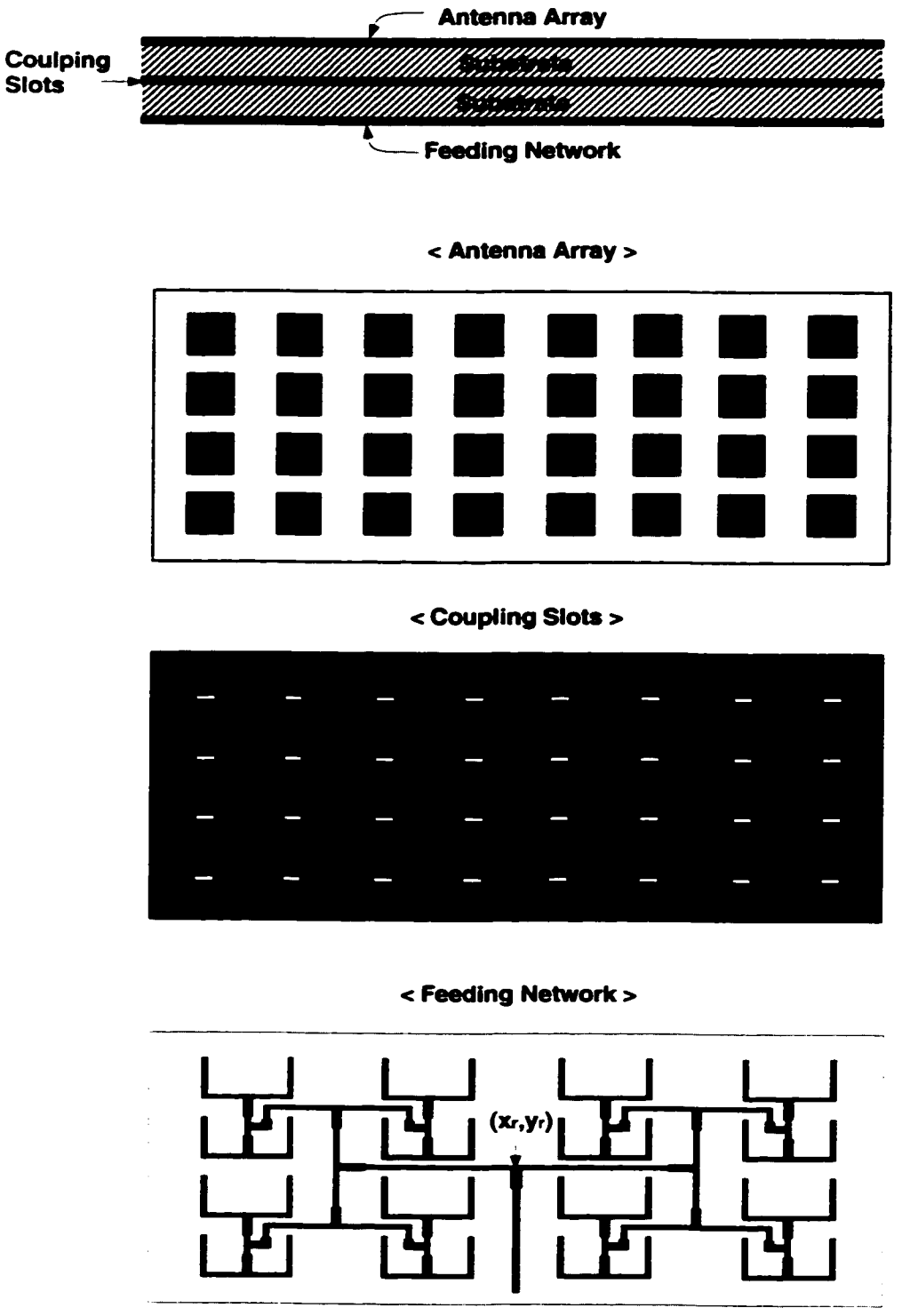

Figure 6.1: Microstrip-feed slot-coupled patch antenna array with double layers

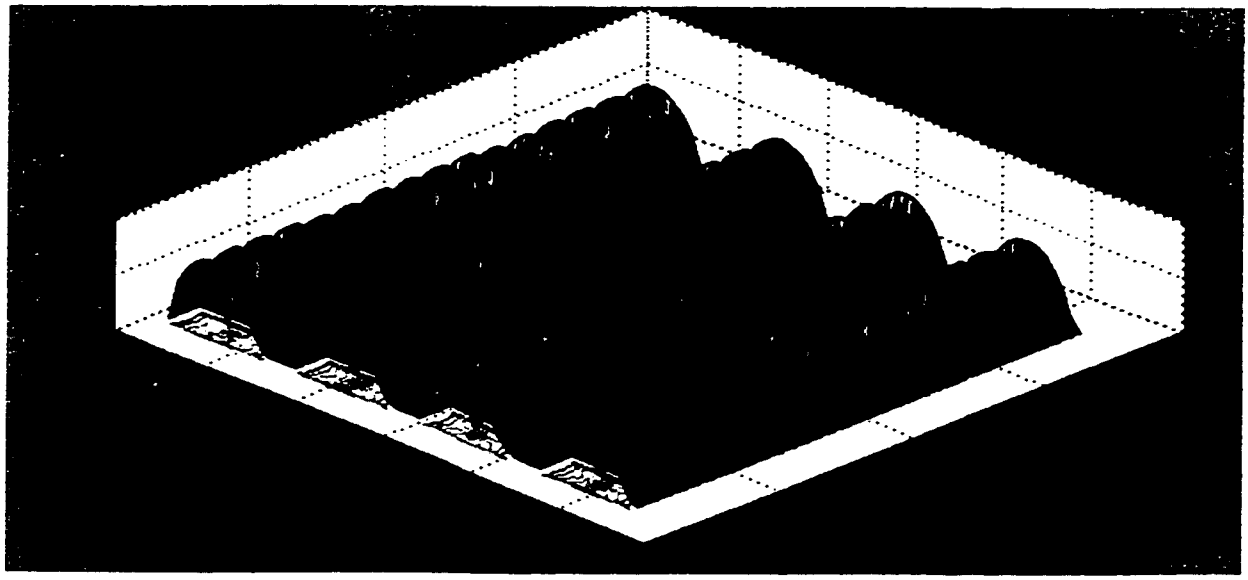

Figure 6.2: Computed current distribution on patch antenna array

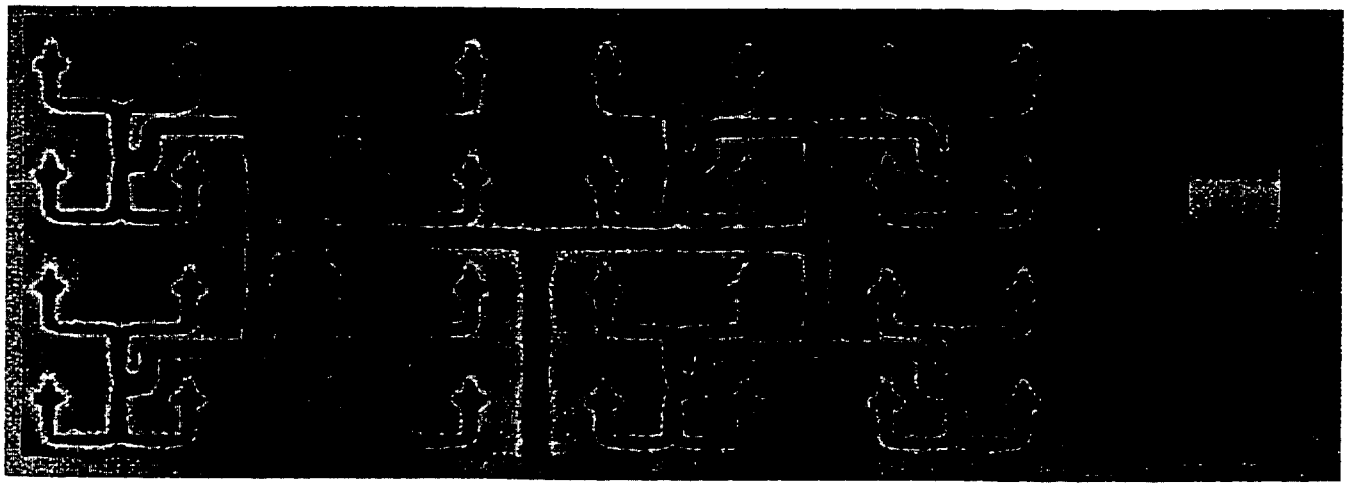

Figure 6.3: Computed total magnetic field distribution on feeding network near resonant frequency

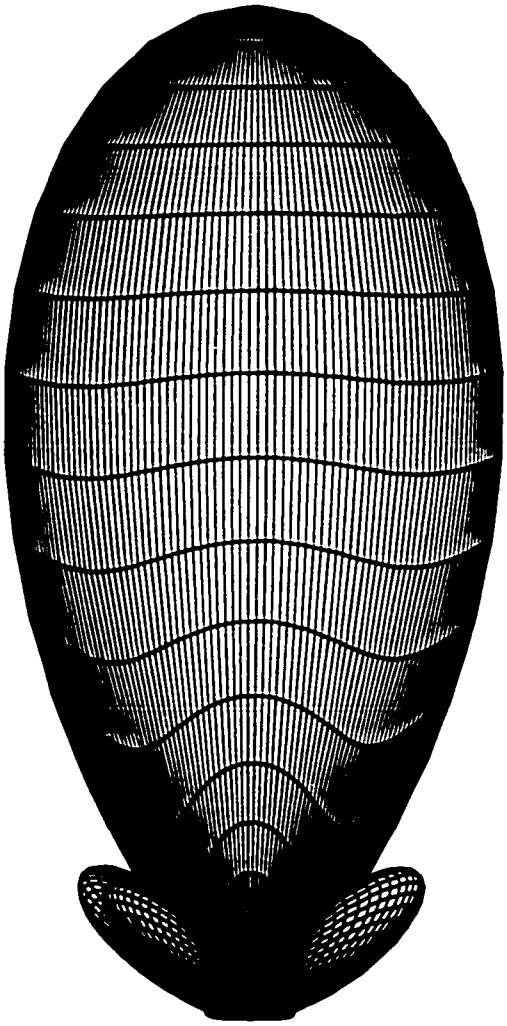

Figure 6.4: Radiating total electric field from 4×8 antenna array

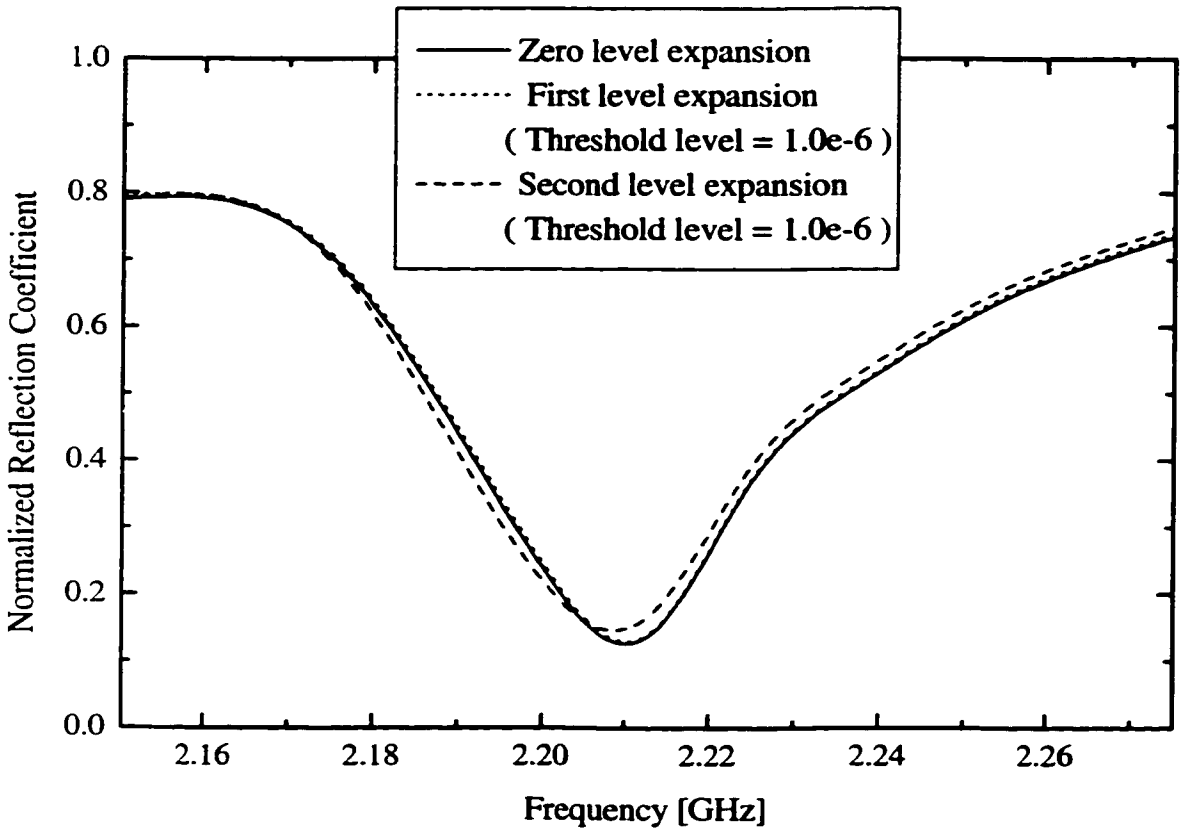

Figure 6.5: Return loss of the array antenna system for multi-level expansions.

6.1.2 First Level Expansion

First level scaling functions and wavelets were deployed on slots and patches to expand the magnetic and electric current, respectively. Using this expansion, we calculated the input impedance of the array system for various threshold levels and presented them in Fig. 6.6. Thresholding is performed locally for each sub-matrix in the hybrid MoM/FEM matrix by discarding terms less than a certain fraction of the maximum element's value. As can be seen in Figs. 6.5 and 6.6, under the tolerance of 2×10^{-6} the computed input impedance is consistent with that of zero level expansion, but it starts to change at the tolerance of 4×10^{-6}. Comparing to the case of second level expansion shown in Fig. 6.7, the input impedance in this expansion shows more sensitivity to threshold tolerance. This is true because first level expansion has fewer wavelet terms and, therefore, the resulting hybrid linear system is less diagonalized than that of second level expansion.

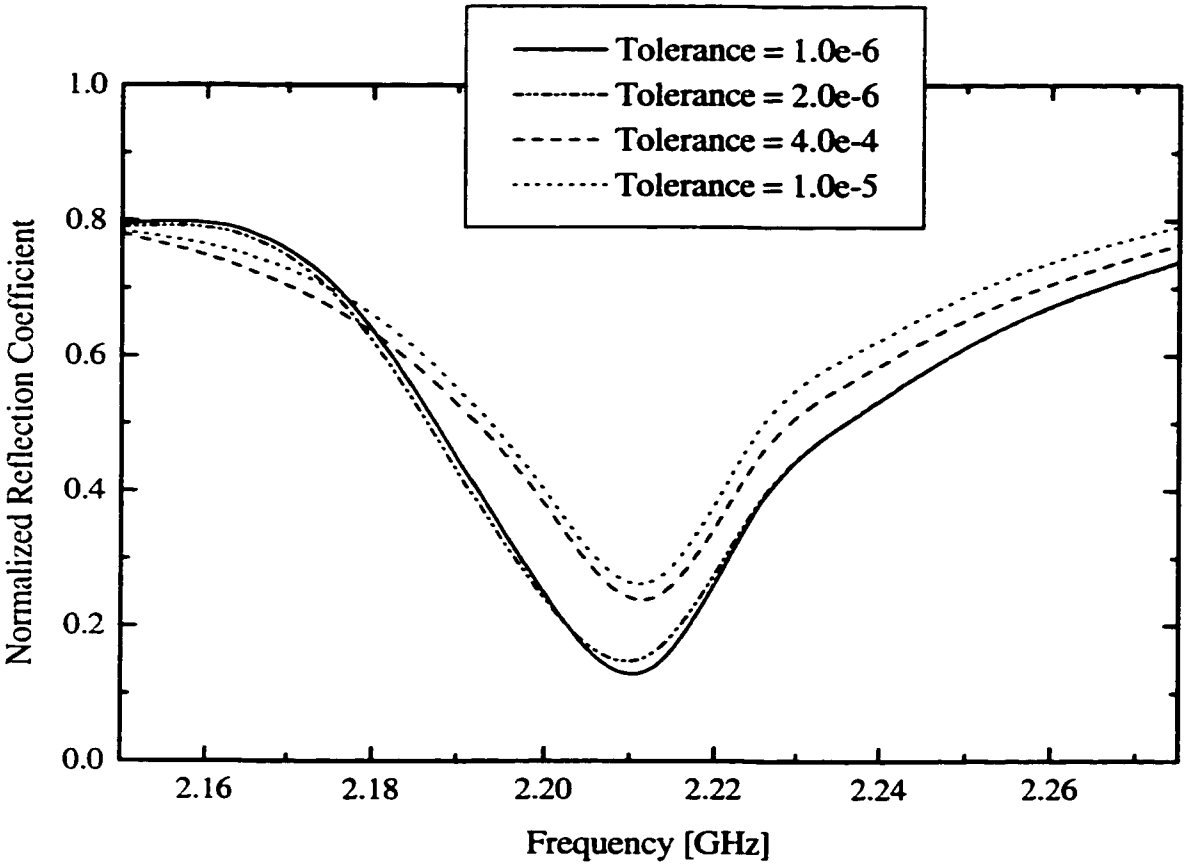

Figure 6.6: Return loss of the array antenna system for first level expansion.

6.1.3 Second Level Expansion

The array problem is now solved with second level scaling and wavelet expansions using the same solution procedure as previously. The calculated return loss of the array system is shown in Fig. 6.5 for three threshold tolerances. As we have observed in the previous expansion case, the accuracy of input impedance is degraded as the threshold rate is increased. Specifically, a threshold of 10^{-6} hardly affects the input impedance of the array system, as shown in Fig. 6.5, and there is only small variation between 10^{-6} and 10^{-5}. Significant change in input impedance comes as the threshold level is raised to 10^{-4}. This variation can be graphically observed in the comparison of total magnetic field distributions on the feeding network as presented in Fig. 6.3. Reasonably enough, the magnetic field in the slot region is vanishing as the threshold tolerance is increased, indicating the decrease of magnetic field coupling through the slot. In addition, a larger standing wave ratio of the magnetic field at the feeding section of microstrip explains the inaccurate return loss in a higher threshold level condition. The electric current in the antenna array in Figs. 6.9 – 6.12 demonstrates the effect of threshold similar to those of the magnetic field on the microstrip feeding network. To show even a small variation on current distribution, which is difficult in an overall current-array distribution for some threshold cases, we also presented a magnified plot, a single cut of a current array. The current has a negligible variation for the tolerances between 10^{-6} and 10^{-5}. At 10^{-4}, however, the overall current profile is similar to the previous one, but the current becomes crumpled and rough in detail. Finally, even the overall current shape is totally destroyed as the threshold level increases to 10^{-2}.

From MRA, the number of meshes and bases on patches and slots in the array system can be calculated using Eqs. 6.1 – 6.7 in each expansion level. The number

of grids (x_{mesh}, y_{mesh}, and sx_{mesh}) is reduced by half as the order of expansion level is increased, while the number of bases remains the same regardless of expansion levels. Since all the bases in each expansion level span the same solution space, according to MRA theory, the solution can be computed at any level of expansion. The amount of required memory for the hybrid MoM/FEM linear system can be estimated by Eq.(6.8). Table 6.1 shows an example of memory size for a second level expansion with a 4×4 grid per patch and a 2×1 grid per slot in a 4×8 array system. This problem can be solved using only scaling functions with a 16×16 grid per patch and an 8×1 grid per slot as an ordinarily MoM computation. However, in this case, almost 4G-bytes of memory are required to store the hybrid MoM/FEM linear system. Alternatively, we can solve the problem using much less memory in the second level expansion. In fact, this expansion also needs the same amount of memory, 4G-bytes, for the hybrid linear system. But the savings in memory come only after thresholding the hybrid linear system and storing only significant terms using sparse matrix storage scheme. We have accurately solved this array problem with threshold tolerance $\leq 10^{-5}$, as shown in Fig. 6.7, using as small as 111.98M-bytes of memory, saving 97.13% of memory. Further thresholding with the tolerance larger than 10^{-5} does not vary the sparsity more than 3% and, more importantly, the computation result is not accurate. Therefore, for this array problem, it is desirable to keep the threshold tolerance under 10^{-5}. Shown in Fig. 6.13 is a structure of the hybrid linear system thresholded by 10^{-3}, where only diagonal elements are remained. For the lower threshold levels, we expect many small off-diagonal elements in the hybrid linear system.

$$x_{mesh} = x_{div}/2^{x_{level}} \tag{6.1}$$

$$y_{mesh} = y_{div}/2^{y_{level}} \tag{6.2}$$

$$N_{by} = (x_{mesh} \times 2^{x_{level}})(y_{mesh} \times 2^{y_{level}} - 1) \tag{6.3}$$

$$N_{bx} = (y_{mesh} \times 2^{y_{level}})(x_{mesh} \times 2^{x_{level}} - 1) \tag{6.4}$$

$$sx_{mesh} = sx_{div} \tag{6.5}$$

$$N_{sx} = sx_{mesh} \times 2^{sx_{level}} - 1 \tag{6.6}$$

$$N_{tot} = (N_{by} + N_{bx} + N_{sx}) \times A_x \times A_y \tag{6.7}$$

$$M_{tot} = ((N_{by} + N_{bx} + N_{sx}) \times A_x \times A_y)^2 \times 16 \tag{6.8}$$

where

- x_{div}, y_{div}: number of divisions in x and y directions at zero level expansion on a single patch.
- x_{mesh}, y_{mesh}: number of divisions in x and y directions at any expansion level on a single patch.
- x_{level}, y_{level} : expansion level of patch in x and y directions
- N_{by}, N_{bx} : number of bases expanding electric current, J_y and J_x, on a single patch.
- sx_{div}: number of divisions in x direction at zero level expansion on a slot.
- sx_{mesh}: number of divisions in x direction at any expansion level on a slot.
- sx_{level}: expansion level of slot in x direction.
- N_{sx}: number of bases expanding magnetic current, M^a, on a slot in x direction.

- A_x, A_y: number of patches in x and y directions.
- N_{tot} : total number of unknowns in slots and patch array.
- M_{tot} : the required memory size for storing a hybrid linear system (Byte).

Threshold level	Sparsity (%)	Num. of non-zero element	Memory (Bytes)
N/A (Ordinarily MoM)	0	15616 × 15616	3.9 G
10^{-6}	95.33	11388236	182 M
10^{-5}	97.13	6998766	111.98 M
10^{-4}	97.69	5633153	90.13 M
10^{-3}	99.43	1397314	22.35 M
10^{-2}	99.81	462113	7.39 M

Table 6.1: Comparison of sparsity of the hybrid MoM/FEM linear system for various threshold levels. – Second level expansion.

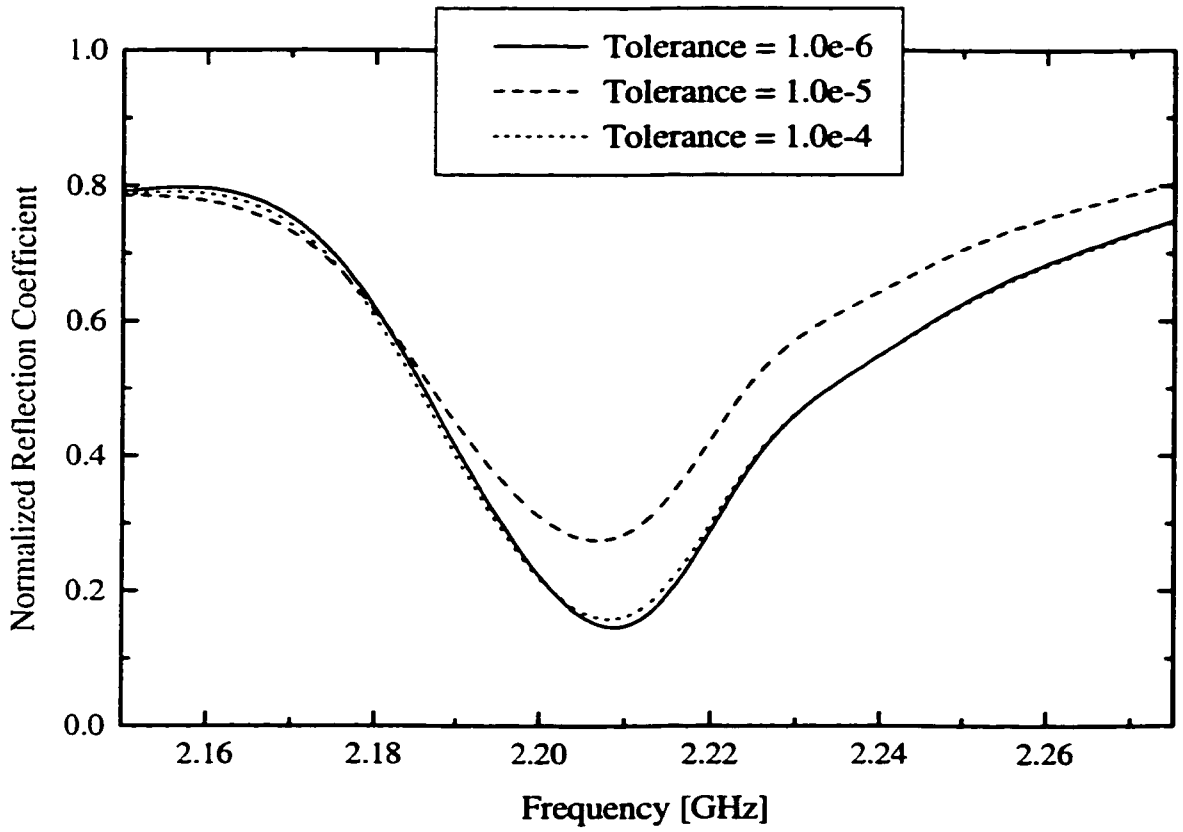

Figure 6.7: Return loss of the array antenna system for second level expansion.

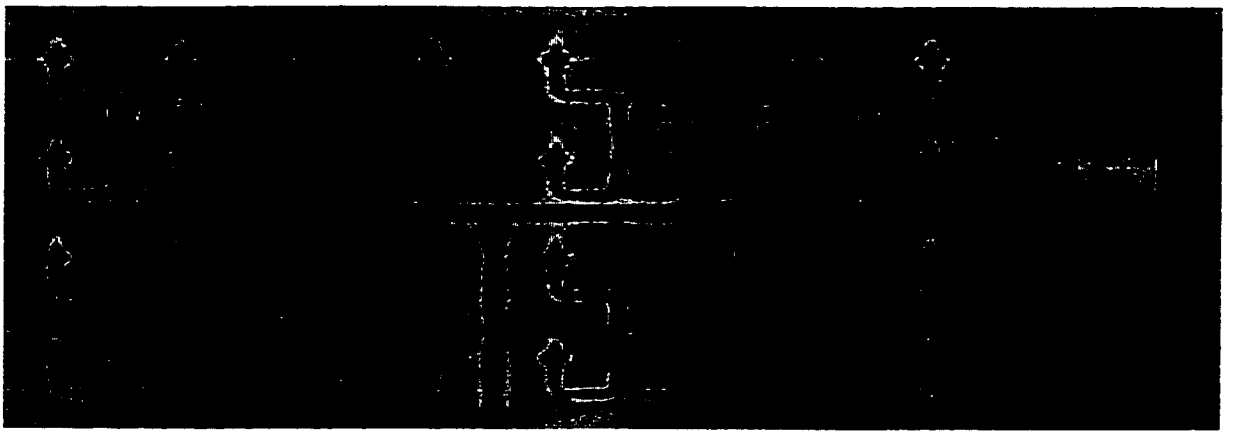

(a)

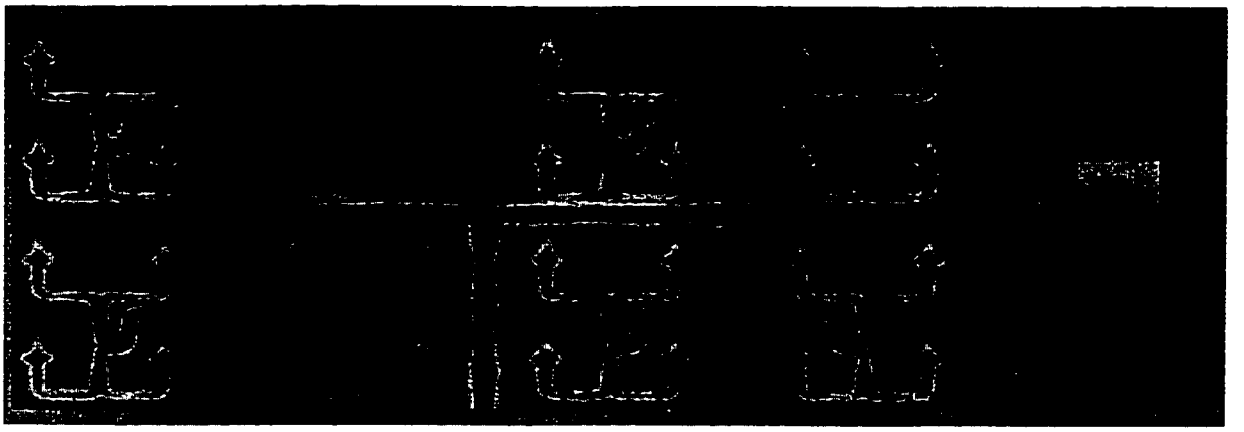

(b)

(c)

Figure 6.8: Computed total magnetic field distributions on feeding network near resonant frequency – Second level expansion for threshold levels of : (a) 10^{-5}, (b) 10^{-4}, (c) 10^{-2}.

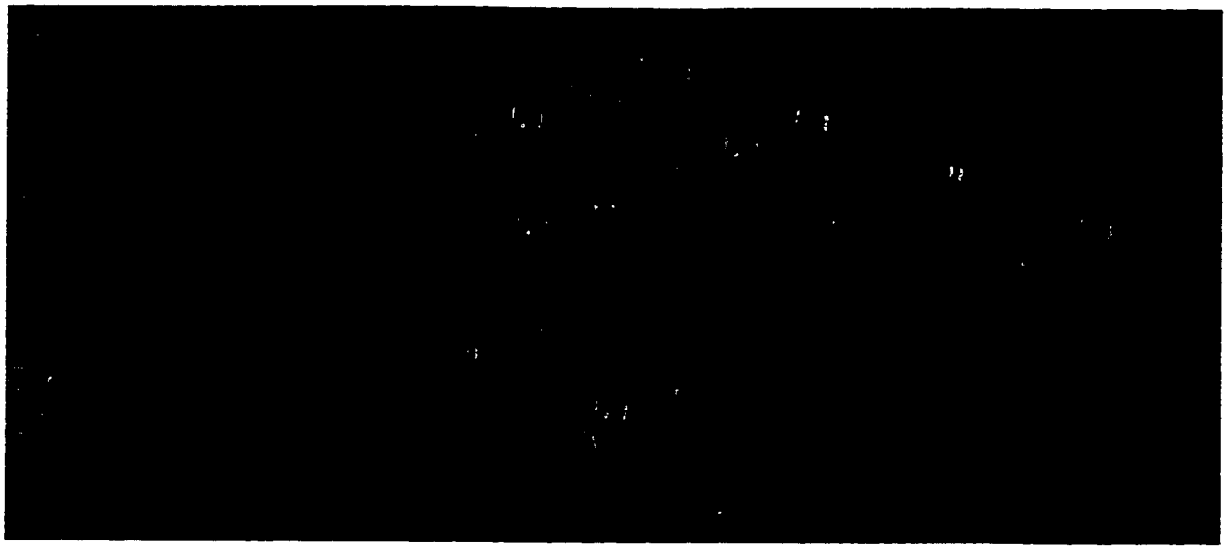

(a)

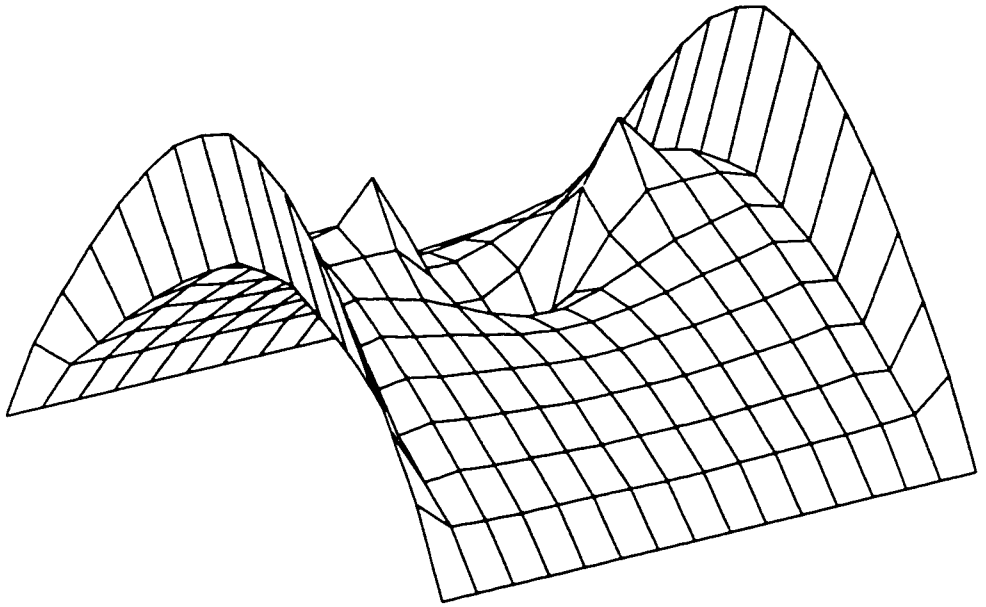

(b)

Figure 6.9: Computed current distribution on antenna array for second level expansion and threshold level of 10^{-6}: (a) overall view, (b) an enlarged view.

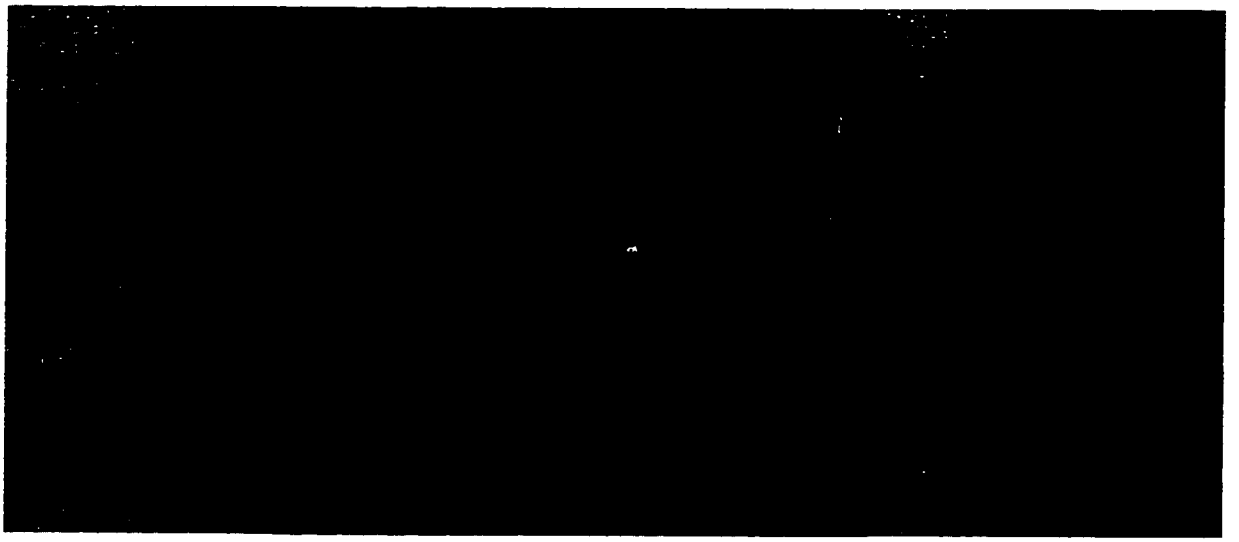

(a)

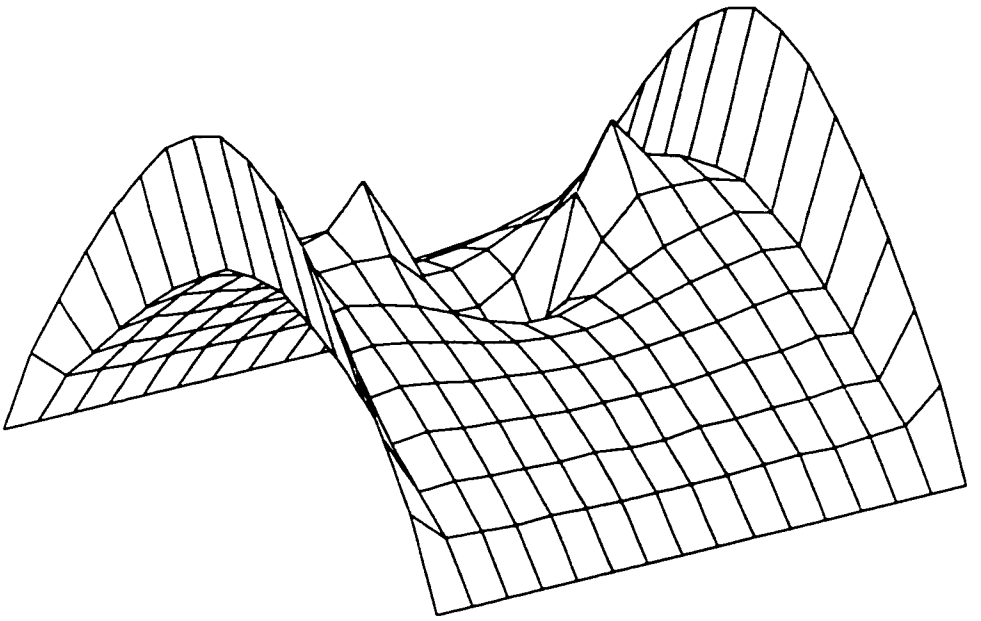

(b)

Figure 6.10: Computed current distribution on antenna array for second level expansion and threshold level of 10^{-5}: (a) overall view, (b) an enlarged view.

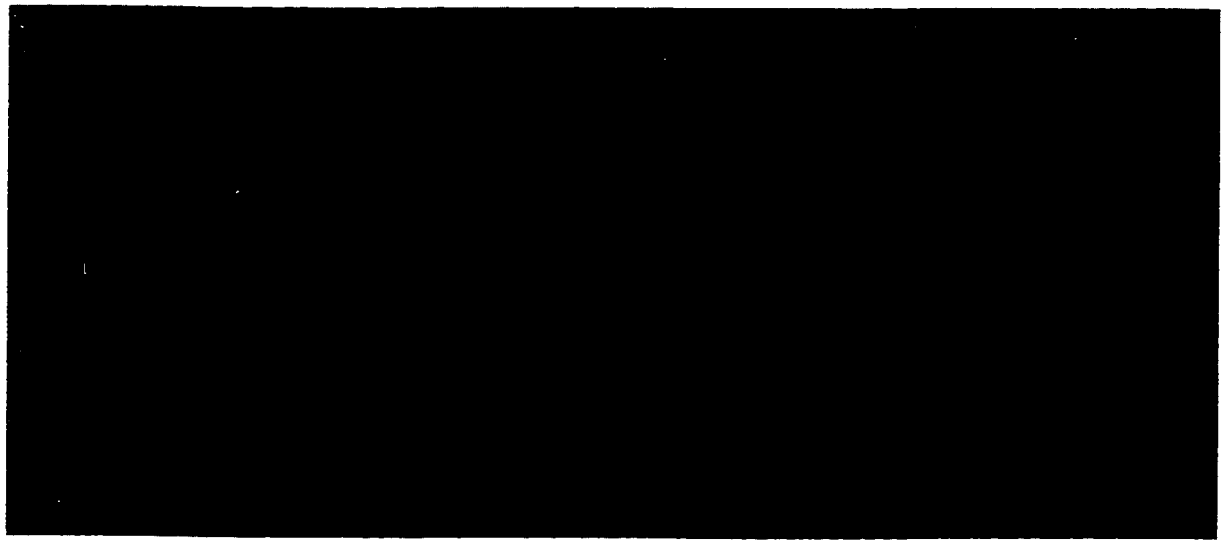

(a)

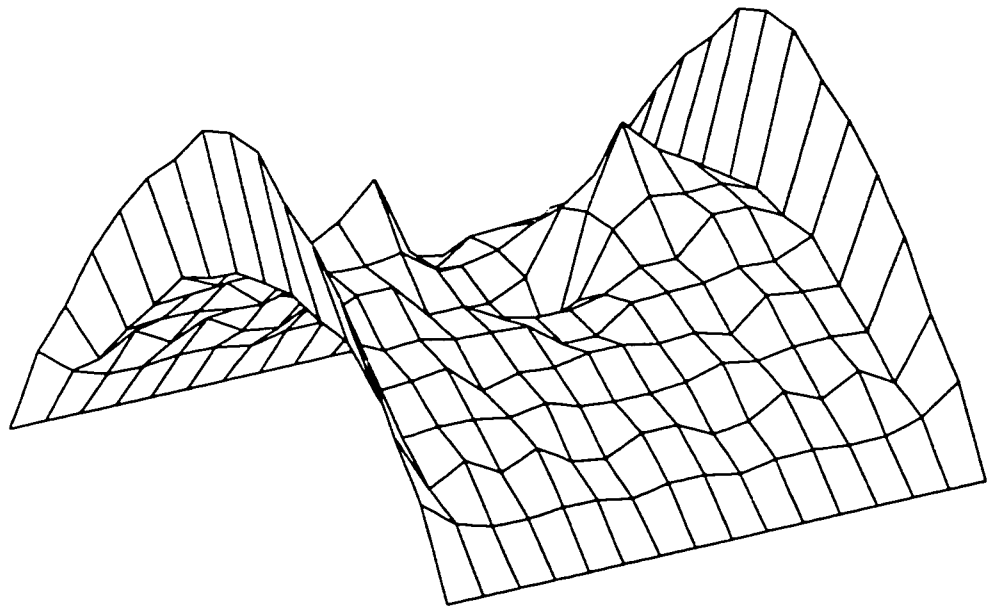

(b)

Figure 6.11: Computed current distribution on antenna array for second level expansion and threshold level of 10^{-4}: (a) overall view, (b) an enlarged view.

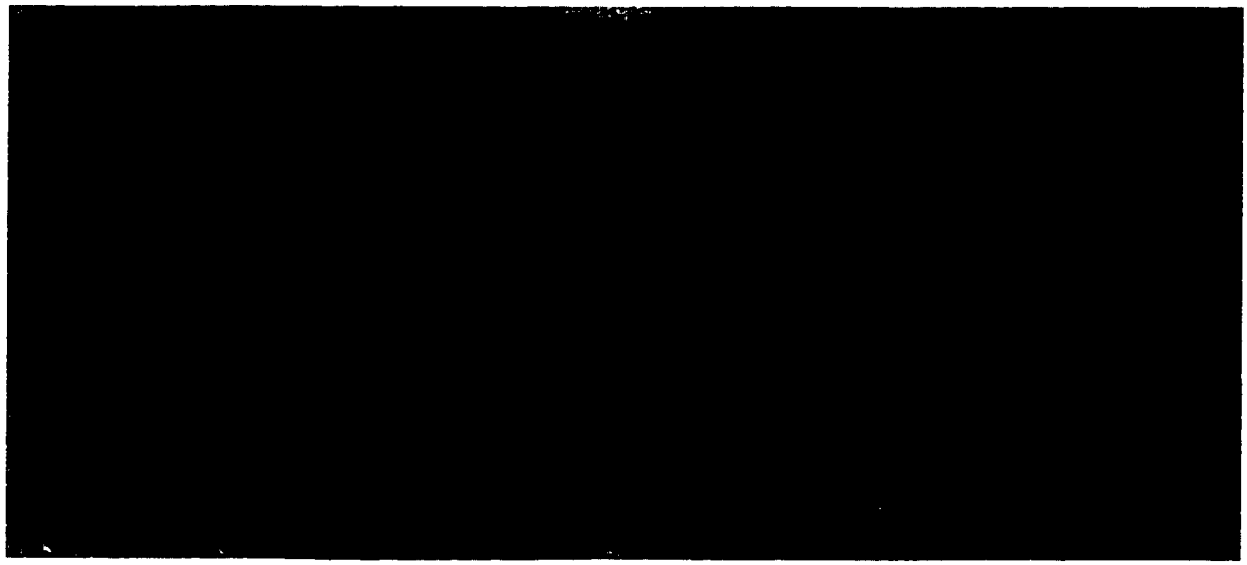

(a)

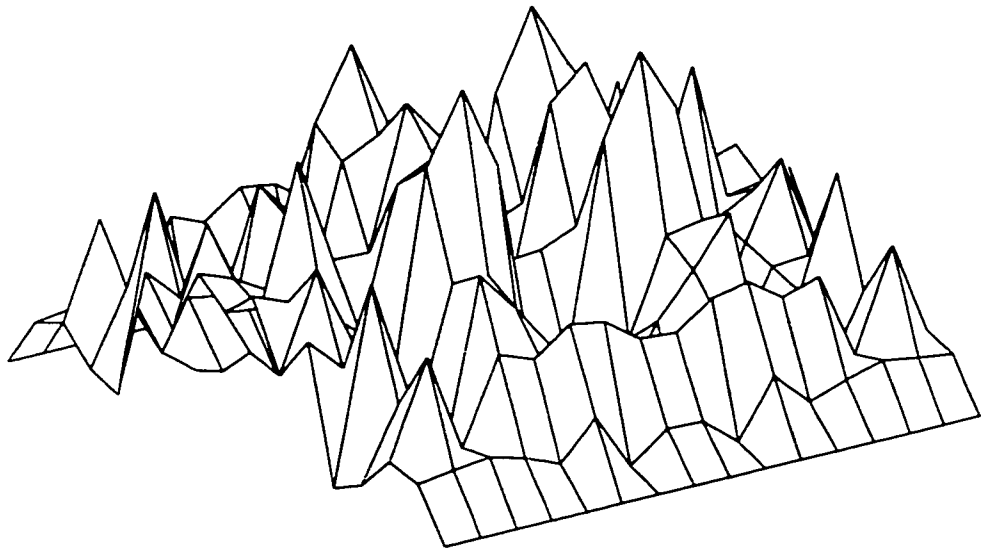

(b)

Figure 6.12: Computed current distribution on antenna array for second level expansion and threshold level of 10^{-2}: (a) overall view, (b) an enlarged view.

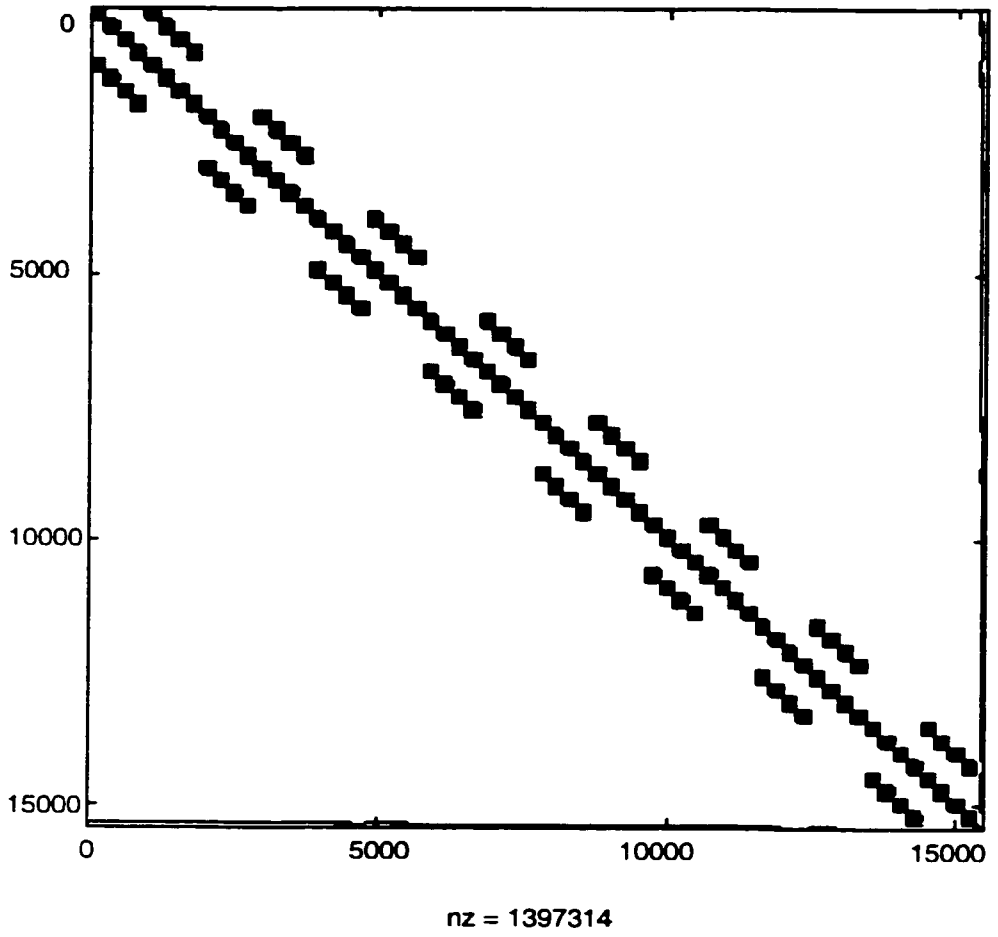

Figure 6.13: A sparse hybrid MoM/FEM linear system generated by second level expansion and a threshold tolerance of 10^{-3} in a 4×8 antenna array problem, showing 99.43% of sparsity.

CHAPTER VII

CONCLUSIONS

7.1 Summary of Achievements

Our effort in this study focused on the development of a fast and accurate computational technique for the large-scale electromagnetic (EM) problems which may include large scattering domains and complex circuit geometries. We have successfully accomplished this task through three stages of development: (1) the development of a hybrid MoM/FEM technique; (2) the application of wavelet theory; and (3) the incorporation of High Performance Computing (HPC).

By effectively combining FEM and MoM, the developed hybrid MoM/FEM technique can selectively utilize the advantage of FEM and MoM according to the characteristics of sub-divided computational domains. For example, an arbitrarily shaped complex circuit geometry filled with homogeneous/inhomogeneous materials can be formulated with FEM, and the radiating free space domain can be solved with MoM utilizing the available free space Green's function. Therefore, we can solve the given EM problem with a smaller cost of analytical effort and computing resources than other existing numerical methods.

The successful application of wavelets on the hybrid MoM/FEM technique has significantly reduced memory and accelerated the computation speed in another way.

Because of a highly sparse linear system rendered by this special basis function (wavelet), we can achieve a huge saving in memory and reduce the time required to solve the hybrid linear system.

While previous efforts primarily concerned theoretical/numerical (software) improvement, HPC emphasizes resolving the computing hardware requirement of the large-scale EM problems – a system that can perform massive/fast computation and has very large memory. Utilizing parallel machines with efficient parallelization strategies, the parallelized hybrid technique not only demonstrates scalable performance (task parallelization) but also can deal with the problems which have on the order of 10^7 unknowns (matrix decomposition method).

The hybrid MoM/FEM technique and its wavelet application have been validated with the single aperture-coupled patch antenna structure: excellent agreement has been achieved between the computed result and the published experimental data. We have further investigated the detailed thresholding mechanism at various expansion levels and thresholding tolerances, and shown how the numerical solutions (such as input impedance, current distribution on patch, and radiation pattern) and the sparsity of the hybrid linear system are affected by them.

Finally, this technique has been applied to a large aperture-coupled patch antenna array system which has on the order of a million unknowns and requires several gigabytes of memory to solve with the conventional methods. As presented in Chapter VI, this large problem is solved using a remarkably small volume of memory (only 5% of memory required for the ordinary technique) in a short time without losing the accuracy of solution. This study, we believe, suggests a strong possibility of the real time design/characterization of large and complex microwave/millimeter-wave devices and circuits.

7.2 Suggested Future Work

The techniques developed throughout this research can be further investigated in several directions:

- Enhancement of wavelet hybrid MoM/FEM technique.
- Application of the developed technique to various large-scale electromagnetic problems that are not amenable to solution with other techniques.
- Improvement and optimization of parallel computation and its application to various parallel platforms.

The wavelet hybrid MoM/FEM technique itself can be enhanced in diverse ways: (1) Incorporation/development of Graphical Users Interface (GUI) for accurate and flexible modeling of complex geometries; (2) rigorous and systematic study of wavelets' thresholding scheme for higher sparsity; (3) fast numerical integration algorithm for short overall MoM computation time; and (4) efficient iterative algorithm for the minimum use of memory and the short solution time of FEM linear system and a hybrid linear system. Furthermore, incorporation of a hybrid MoM/FEM technique with other numerical methods, such as the finite difference time domain (FDTD) method, can provide more methodological flexibility in solving sub-divided computational domains.

The developed wavelet hybrid MoM/FEM technique can be applied to other interesting electromagnetic scattering and high-speed high-frequency circuit problems which can utilize the advantages of this technique. This type of EM problems is often encountered in most of today's advanced communication systems.

Lastly, efficient parallel schemes can improve the overall performance of wavelet hybrid technique in terms of memory and speed. In particular, we can effectively

decompose FEM and hybrid linear systems into processors for optimum load balancing and memory management. In addition, efficient parallelization of repeated matrix-vector multiplication can speed up the iterative solution process. Utilization of appropriate parallel platforms for various parallel schemes is another possible way to enhance HPC capability.

APPENDICES

APPENDIX A

Calculation of the Actual Magnetic Field and Input Impedance in Hybrid MoM/FEM Technique

The actual magnetic field in the feeding domain can be calculated from the linear combination of solutions of hybrid equations and magnetic field excited by each magnetic current on apertures and the feeding domain.

$$\bar{H}_2 = \bar{H}_2(M_f) + \sum_{n=1}^{N_a} m^a{}_n \bar{H}_2(M^a{}_n) \tag{A.1}$$

where $\bar{H}_2(M_f)$ is the magnetic field excited by magnetic current on the feeding domain (M_f), N_a is the total number of magnetic currents on apertures, m^a is the calculated coefficients of magnetic currents on apertures computed from Eq. (2.22), and $\bar{H}_2(M^a)$ is the magnetic field excited by magnetic currents in aperture (M^a).

The normalized input impedance of the system can be obtained from the actual magnetic field in Eq. (A.1) using the following relation [71].

$$z_{in} = \frac{1 - \Gamma e^{-j\frac{4\pi}{\lambda_g}l}}{1 + \Gamma e^{-j\frac{4\pi}{\lambda_g}l}} \tag{A.2}$$

where l is the length of the microstrip from the reference plane to the open end of feeding line, and λ_g is the guided wavelength measured from the magnetic field in Eq. (A.1). Γ is the reflection coefficient computed as follows.

$$\Gamma = \frac{\frac{I_{max}}{I_{min}} - 1}{\frac{I_{max}}{I_{min}} + 1} \tag{A.3}$$

where I_{max} and I_{min} are maximum and minimum value of magnetic field in Eq. (A.1).

APPENDIX B

Calculation of Impedance Matrix Elements

Computation of impedance matrix elements in Eqs. (2.14) - (2.19) requires elaborate mathematical handling to simplify and accelerate multi-fold integrations. This appendix shows how these complex integrations are dealt with spectral domain technique, a polar coordinate system, and a pole extraction method [72].

Suppose a conductor-backed dielectric slab, where the dielectric layer is parallel to the x-y plane with a height of d in z direction and the conductor sheet is placed on the x-y plane, as shown in Fig. B.1. The interactions between currents located at $z=z_1$ (either 0 or d) produce the following form of impedance matrix element.

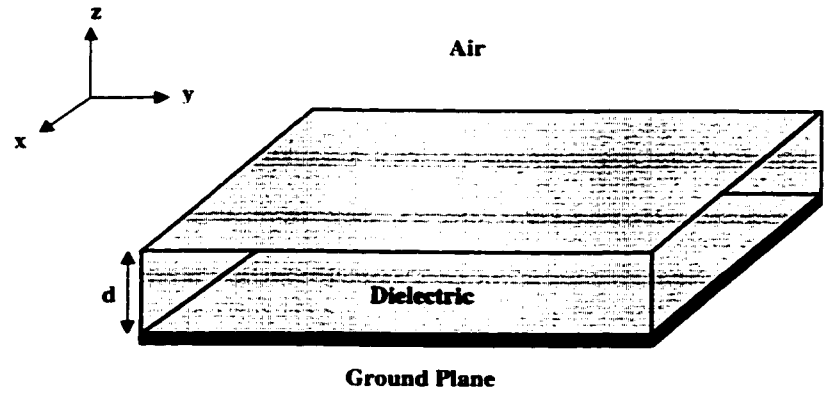

Figure B.1: Conductor-backed dielectric slab.

$$z_{ij} = (S_i, F(S_j))$$

$$= \iint \iint S_i(x,y) \cdot S_j(x'.y') \cdot G(x,y,z_1;x',y',z_1)\, dx\, dy\, dx'\, dy' \qquad \text{(B.1)}$$

where $S_{i,j}$ is the electric or magnetic current at z_1, and G is the Green's function associated with current at (x', y', z_1) and its generated field at (x, y, z_1).

Using the spectral domain representation of Green's function [69]

$$G(x,y,z_1;x',y',z_1) = \iint_{-\infty}^{\infty} \widetilde{G}(k_x,k_y) \cdot e^{jk_x(x-x')}\, e^{jk_y(y-y')}\, dk_x\, dk_y \qquad \text{(B.2)}$$

we can convert Eq.(B.1) into

$$z_{ij} = \iint \iint S_i(x,y) \cdot S_j(x',y') \cdot \iint_{-\infty}^{\infty} \widetilde{G}(k_x,k_y) \cdot e^{jk_x(x-x')}\, e^{jk_y(y-y')}\, dk_x\, dk_y\, dx\, dy\, dx'\, dy'$$

$$= \iint_{-\infty}^{\infty} \widetilde{S}_i^*(k_x,k_y) \cdot \widetilde{S}_j(k_x,k_y) \cdot \widetilde{G}(k_x,k_y)\, dk_x\, dk_y \qquad \text{(B.3)}$$

where

$$\widetilde{S}_{i,j} = \iint S_{i,j}(x,y) \cdot e^{-j(k_x x + k_y y)}\, dx\, dy \qquad \text{(B.4)}$$

and " $*$ " is the conjugate operator. The complete spectral domain forms, $\widetilde{G}$, of the Green's function are shown in Appendix C. If S_i and S_j are real and can be separated as

$$\widetilde{S}_{i,j}(k_x,k_y) = \widetilde{S}_{i,j}^{x}(k_x)\, \widetilde{S}_{i,j}^{y}(k_y) \qquad \text{(B.5)}$$

we can write Eq.(B.3) as

$$z_{ij} = \iint_{-\infty}^{\infty} \widetilde{S}_i^{x*}(k_x)\, \widetilde{S}_i^{y*}(k_y) \cdot \widetilde{S}_j^{x}(k_x)\, \widetilde{S}_j^{y}(k_y) \cdot \widetilde{G}(k_x,k_y)\, dk_x\, dk_y \qquad \text{(B.6)}$$

We can further facilitate the solution of integrals in Eq.(B.6) by changing Eq.(B.6) to polar coordinates β, θ using the following relations:

$$k_x = \beta \cos\theta \qquad \text{(B.7)}$$

$$k_y = \beta \sin\theta \qquad \text{(B.8)}$$

which leads to

$$z_{ij} = \int_0^{2\pi} \int_0^{\infty} \widetilde{S}_i^{x*}\ \widetilde{S}_i^{y*} \cdot \widetilde{S}_j^{x}\ \widetilde{S}_j^{y} \cdot \widetilde{G} \cdot \beta\, d\beta\, d\theta \tag{B.9}$$

Utilizing the even and odd properties of the integrand with respect to k_x and k_y, we can reduce integration over θ from 2π to $\pi/4$. That is

$$z_{ij} = 4\int_0^{\pi/2} \int_0^{\infty} Re(\widetilde{S}_i^{x*}\ \widetilde{S}_i^{y*} \cdot \widetilde{S}_j^{x}\ \widetilde{S}_j^{y}) \cdot \widetilde{G} \cdot \beta\, d\beta\, d\theta \tag{B.10}$$

for even functions of $\widetilde{G}$, and

$$z_{ij} = 4\int_0^{\pi/2} \int_0^{\infty} Im(\widetilde{S}_i^{x*}\ \widetilde{S}_i^{y*} \cdot \widetilde{S}_j^{x}\ \widetilde{S}_j^{y}) \cdot \widetilde{G} \cdot \beta\, d\beta\, d\theta \tag{B.11}$$

for odd functions of $\widetilde{G}$, where Re and Im denote real and imaginary parts of its enclosing functions, respectively.

Finally, we remove singularities, namely, the surface wave poles, in the Green's function, using a pole extraction technique. Let β_0 be a surface wave pole and Eqs.(B.10) – (B.11) be

$$z_{ij} = 4\int_0^{\pi/2} \int_0^{\infty} \frac{q(\beta,\theta)\beta}{r(\beta)} \cdot \beta\, d\beta\, d\theta, \quad \text{where } r(\beta_0) = 0 \tag{B.12}$$

We remove the pole β_0 in the integrand of Eq.(B.12) by subtracting the integrand by a function that approximates the integrand near β_0. This approximated function is obtained by

$$\begin{aligned}
\lim_{\beta\to\beta} \frac{q(\beta,\theta)\beta}{r(\beta)} &= \lim_{\beta\to\beta_0} \frac{q(\beta,\theta)\beta}{(\beta-\beta_0)} \frac{(\beta-\beta_0)}{r(\beta)-r(\beta_0)} \\
&= \lim_{\beta\to\beta_0} \frac{q(\beta,\theta)\beta}{(\beta-\beta_0)} \frac{1}{r'(\beta)} \\
&= \lim_{\beta\to\beta_0} \frac{q(\beta_0,\theta)}{r'(\beta_0)} \frac{\beta_0}{(\beta-\beta_0)} \\
&= \lim_{\beta\to\beta_0} \frac{q(\beta_0,\theta)}{r'(\beta_0)} \frac{2\beta_0^2}{(\beta-\beta_0)(\beta_0+\beta_0)}
\end{aligned}$$

$$= \lim_{\beta \to \beta_0} \frac{q(\beta_0, \theta)}{r'(\beta_0)} \frac{2\beta_0^2}{\beta^2 - \beta_0^2} \tag{B.13}$$

Therefore, after pole extraction, Eq.(B.12) can be integrated with the following expression.

$$z_{ij} = 4 \int_0^{\pi/2} \int_0^{\infty} \left[\frac{q(\beta, \theta)\beta}{r(\beta)} - \frac{q(\beta_0, \theta)}{r'(\beta_0)} \frac{2\beta_0^2}{\beta^2 - \beta_0^2} \right] d\beta d\theta + 4 \int_0^{\pi/2} \int_0^{\infty} \frac{q(\beta_0, \theta)}{r'(\beta_0)} \frac{2\beta_0^2}{\beta^2 - \beta_0^2} d\beta d\theta$$

$$= 4 \int_0^{\pi/2} \int_0^{\infty} \left[\frac{q(\beta, \theta)\beta}{r(\beta)} - \frac{q(\beta_0, \theta)}{r'(\beta_0)} \frac{2\beta_0^2}{\beta^2 - \beta_0^2} \right] d\beta d\theta + 4 \int_0^{\pi/2} -j\pi\beta_0 \frac{q(\beta_0, \theta)}{r'(\beta_0)} d\theta \tag{B.14}$$

Note that the infinite integration can generally be terminated at $\beta \simeq 150k_0$ [72].

APPENDIX C

Spectral Domain Green's Functions for Conductor-backed Dielectric Slab

Presented are the spectral domain Green's functions for the conductor-backed dielectric slab structure in Fig. B.1.

The components of the Green's function are

$G_{EJ}^{yy} = E_y$ at (x, y, d) due to y-directed electric current at (x', y', d)

$G_{EJ}^{xx} = E_x$ at (x, y, d) due to x-directed electric current at (x', y', d)

$G_{EJ}^{xy} = E_x$ at (x, y, d) due to y-directed electric current at (x', y', d)

$G_{HJ}^{xy} = H_x$ at $(x, y, 0)$ due to y-directed electric current at (x', y', d)

$G_{HJ}^{yx} = H_y$ at $(x, y, 0)$ due to x-directed electric current at (x', y', d)

$G_{HM}^{xx} = H_x$ at $(x, y, 0)$ due to x-directed magnetic current at $(x', y', 0)$

$G_{HJ}^{xx} = H_x$ at $(x, y, 0)$ due to x-directed electric current at (x', y', d)

$G_{EJ}^{yx} = E_y$ at (x, y, d) due to x-directed electric current at (x', y', d)

$G_{EM}^{yx} = E_y$ at (x, y, d) due to x-directed magnetic current at $(x', y', 0)$

$G_{EM}^{xx} = E_x$ at (x, y, d) due to x-directed magnetic current at $(x', y', 0)$

and their spectral domain representations, $\widetilde{G}$, are

$$\widetilde{G}_{EJ}^{yy} = -j\,\frac{Z_0}{4\pi^2 k_0}\,\frac{\sin(k_1 d)}{T_e T_m}\,[(\epsilon_r k_0^2 - k_y^2)k_2\cos(k_1 d) + j(k_0^2 - k_y^2)k_1\sin(k_1 d)] \quad \text{(C.1)}$$

$$\widetilde{G}_{EJ}^{xx} = -j\,\frac{Z_0}{4\pi^2 k_0}\,\frac{\sin(k_1 d)}{T_e T_m}\,[(\epsilon_r k_0^2 - k_x^2)k_2\cos(k_1 d) + j(k_0^2 - k_x^2)k_1\sin(k_1 d)] \quad \text{(C.2)}$$

$$\widetilde{G}_{EJ}^{xy} = \frac{Z_0}{4\pi^2 k_0}\,\frac{jk_x k_y}{T_e T_m}\,\sin(k_1 d)\,[k_2\cos(k_1 d) + jk_1\sin(k_1 d)] \quad \text{(C.3)}$$

$$\widetilde{G}_{HJ}^{xy} = \frac{1}{4\pi^2}\,\frac{1}{T_e T_m}\,[-\epsilon_r k_1 k_2\cos(k_1 d) + j(k_y^2(\epsilon_r - 1) - k_1^2)\sin(k_1 d)] \quad \text{(C.4)}$$

$$\widetilde{G}_{HJ}^{yx} = \frac{1}{4\pi^2}\,\frac{1}{T_e T_m}\,[\epsilon_r k_1 k_2\cos(k_1 d) - j(k_x^2(\epsilon_r - 1) - k_1^2)\sin(k_1 d)] \quad \text{(C.5)}$$

$$\widetilde{G}_{HM}^{xx} = \frac{-j}{4\pi^2 k_0 Z_0}\,\frac{1}{k_1 T_e T_m}\,[jk_x^2 k_1^2(\epsilon_r - 1) + (\epsilon_r k_0^2 - k_x^2)$$
$$\times\,\{k_1 k_2(\epsilon_r + 1)\sin(k_1 d)\cos(k_1 d) + j(\epsilon_r k_2^2\sin(k_1 d) - k_1^2\cos^2(k_1 d)\}] \quad \text{(C.6)}$$

$$\widetilde{G}_{HJ}^{xx} = \frac{1}{4\pi^2}\,\frac{jk_x k_y}{T_e T_m}\,(\epsilon_r - 1)\,\sin(k_1 d) \quad \text{(C.7)}$$

$$\widetilde{G}_{EJ}^{yx} = \widetilde{G}_{EJ}^{xy} \quad \text{(C.8)}$$

$$\widetilde{G}_{EM}^{yx} = -\widetilde{G}_{HJ}^{xy} \quad \text{(C.9)}$$

$$\widetilde{G}_{EM}^{xx} = -\widetilde{G}_{HJ}^{xx} \quad \text{(C.10)}$$

where G and $\widetilde{G}$ are related to

$$G(x, y, z_1; x', y', z_1) = \iint_{-\infty}^{\infty} \widetilde{G}(k_x, k_y)\;\cdot\; e^{jk_x(x-x')}\,e^{jk_y(y-y')}\,dk_x\,dk_y, \quad \text{(C.11)}$$

The following definitions are used in the expressions:

$$k_0^2 = \omega^2\mu_0\epsilon_0 \quad \text{(C.12)}$$

$$k_1 = \sqrt{\epsilon_r k_0^2 - \beta^2},\;\; Re[k_1] > 0,\;\; Im[k_1] < 0 \quad \text{(C.13)}$$

$$k_2 = \sqrt{k_0^2 - \beta^2},\;\; Re[k_2] > 0,\;\; Im[k_2] < 0 \quad \text{(C.14)}$$

$$\beta^2 = k_x^2 + k_y^2 \quad \text{(C.15)}$$

$$T_e = k_1\cos(k_1 d) + jk_2\sin(k_1 d) \quad \text{(C.16)}$$

$$T_m = \epsilon_r k_2 \cos(k_1 d) + j k_1 \sin(k_1 d) \tag{C.17}$$

$$Z_0 = \sqrt{\frac{\mu_0}{\epsilon_0}} \tag{C.18}$$

BIBLIOGRAPHY

BIBLIOGRAPHY

[1] R. F. Harrington, *Field computation by moment methods*, New York: Macmillan, 1968.

[2] P. P. Silvester and R. L. Ferrari, *Finite elements for electrical engineers*, Cambridge: Cambridge University Press, 1991.

[3] O. C. Zienkiewicz, *The finite element method: vol. 1 Basic formulation and linear problems*, London: McGraw-Hill Book Company, 4th ed., 1994.

[4] M. Krumpholtz and P. Russer, "Two-dimensional FDTD and TLM," *Int., J. of Num. Model. : Electron. Net. Dev. Fields*, vol. 7, pp. 141–153, 1994.

[5] M. Krumpholtz, C. Huber, and P. Russer, "A field theoretical comparison of FDTD and TLM," *IEEE Trans. Microwave Theory Tech.*, vol. MTT-43, pp. 1935–1950, 1995.

[6] T. Chio and D. H. Schaubert, "Hybrid 3-D finite element/MoM analysis for antennas with thin dielectric cover," *IEEE Antennas and Propagation International Symposium*, vol. 2, pp. 1270–1273, 1998.

[7] Jui-Ching Cheng, Nihad I. Dib and Linda P. B. Katehi, "Theoretical Modeling of Cavity-Backed Patch Antennas Using a Hybrid Technique," *IEEE Trans. Antennas and Propagation*, vol. 43, no. 9, pp. 1003–1013, Aug. 1995.

[8] S. G. Mallat, "Multiresolution approximation and wavelet orthonormal bases of L^2," *Trans. Amer. Math. Soc.*, vol. 3-15, pp. 69–87, Sept. 1989.

[9] G. Strang, "Wavelets and dielation equations: A brief introduction," *SIAM Rev.*, vol. 31, no. 4, pp. 614–627, Dec. 1989.

[10] S. G. Mallat, "A theory for multiresolution signal decomposition: The wavelet representation," *IEEE Trans. Pattern Anal. Machine Intell.*, vol. PAMI-7, pp. 674–693, July 1989.

[11] V. Kumar, A. Grama, A. Gupta, and G. Karypis, *Introduction to parallel computing: design and analysis of algorithums*, Redwood City: The Benjamin/Cummings Publishing Company, Inc., CA, 1994.

[12] M. Cosnard and D. Trystram, *Parallel algorithms and architectures*, Boston: PWS Publishing Company, 1995.

[13] K. K. Mei, R. Stovall, and D. Tremain, "On difference coupling methods of solving radiation problems," in *URSI Fall Meeting Digest*, Sept. 1971.

[14] P. Silvester and M. S. Hsieh, "Finite-element solution of 2-dimensional exterior field problems," *Proc. Inst. Elec. Eng.*, vol. 118, pp. 1743–1747, Dec. 1971.

[15] B. H. Mcdonald and A. Wexler, "Finite-element solution of unbounded field problems," *IEEE Trans. Microwave Theory Tech.*, vol. MTT–20, no. 12, pp. 841–847, Dec. 1972.

[16] K. K. Mei, "Unimoment method of solving antenna and scattering problems," *IEEE Trans. Antennas Propagat.*, vol. 22, pp. 760–766, Nov. 1974.

[17] M. A. Morgan and K. K. Mei, "Finite-element computation of scattering by inhomogeneous penetrable bodies of revolution," *IEEE Trans. Antennas Propagat.*, vol. 27, pp. 202–214, March 1979.

[18] S. K. Jeng and C. H. Chen, "On variational electromagnetics: theory and application," *IEEE Trans. Antennas Propagat.*, vol. 32, pp. 902–907, Sept. 1984.

[19] J.-M. Jin and V. V. Liepa, "Application of hybrid finite element method to electromagnetic scattering from coated cylinders," *IEEE Trans. Antennas Propagat.*, vol. 36, no. 1, pp. 50–54, Dec. 1988.

[20] X. Yuan, D. R. Lynch, and J. W. Strohbehn, "Coupling of finite element and moment methods for electromagnetic scattering from inhomogeneous objects," *IEEE Trans. Antennas Propagat.*, vol. 38, no. 3, pp. 386–393, March 1990.

[21] A. J. Sangster and H. Wang,"Combined FEM/MoM technique of coupling and radiating aperatures in rectangular waveguide," *IEEE Trans. Magnetics*, vol. 31, no. 3, pt. 1, pp. 1554–1557, May 1995.

[22] A. C. Polycarpou and C. A. Balanis, "Analysis of ferrite loaded cavity backed slot antennas using a hybrid FEM/MoM approach," *IEEE Antennas and Propagation International Symposium*, vol. 2, pp. 652–655, 1997.

[23] Y. Ji, J. Chen, T. H. Hubing, and J. L. Drewniak, "Application of a hybrid FEM/MoM method to a canonical PCB problem," *IEEE International Symposium on Electromagnetic Compatibility*, vol. 1, pp. 91–96, 1999.

[24] R. F. Harrington, *Time-harmonic elecromagnetic fields*, New York: McGraw-Hill, 1961.

[25] J. Jin, *The finite element method in electromagnetics*, New York: John Wiley & Sons, Inc, 2nd ed., 1993.

[26] I. Daubechies, "Orthonormal bases of compactly supported wavelets," *Comm. Pure Appl. Math.*, vol. 41, pp. 909–996, 1988.

[27] O. Rioul and M. Vetterli, "Wavelets and signal processing," *IEEE Signal Processing Magazine*, vol. 8, no. 4, pp. 14–38, Oct. 1991.

[28] R. De Vore, B. Jawerth, and B. Lucier. "Image compression through wavelet transformation coding," *IEEE Trans. on Information Theory*, vol. 38, no. 2, pp. 719–746, March 1992.

[29] E. J. Stollnitz, T. D. DeRose, and D. H. Salesin, "Wavelets for Computer Graphics: A Primer I," *IEEE Trans. on Computer Graphics and Applications*, pp. 76–84, May 1995.

[30] G. Beylkin, R. Coifman and V. Rokhlin, "Fast wavelet transformations and numerical algorithms I," *Comm. Pure Appl. Math.*, vol. 44, pp. 141–183, 1991.

[31] B. Alpert, G. Beylkin, R. Coifman and V. Rokhlin, "Wavelet-like bases for the fast solution of second-kind integral equations," *SIAM J. Sci. Comput.*, vol. 14, no. 1, pp. 159–184, Jan. 1993.

[32] B. Z. Steinberg and Y. Leviatan, "On the use of wavelet expansions in the method of moments," *IEEE Trans. Antennas and Propagation*, vol. 41, no. 5, pp. 610–619, May 1993.

[33] K. F. Sabet, J.-C. Cheng, and L. P. B. Katehi, "Efficient wavelet-based modeling of printed circuit antenna arrays," *IEE Proc. Microwave Antennas Propag.*, vol. 146, no. 4, pp. 298–304, Aug. 1999.

[34] G. Oberschmidt, K. Bubke, and A. F. Jacob, "Two-dimensional wavelet-analysis of a microstip open," *IEEE Trans. Microwave Theory Tech.*, vol. MTT–46, no. 5, pp. 558–561, May 1998.

[35] K. F. Sabet and L. P. B. Katehi, "A study of dielectric resonators based on two-dimensional fast wavelet algorithm," *IEEE Microwave and Guided Wave Lett.*, vol. 6, no. 1, pp. 19–21, Jan. 1996.

[36] K. F. Sabet and L. P. B. Katehi, "Analysis of integrated millimeter-wave and submillimeter-wave waveguides using orthonormal wavelets expansions," *IEEE Trans. Microwave Theory Tech.*, vol. MTT–42, pp. 2412–2422, Dec. 1994.

[37] G. Wang and G.-W. Pan, "Full wavel analysis of microstrip floating line sturctures by wavelet expansion method," *IEEE Trans. Microwave Theory Tech.*, vol. MTT–43, no. 1, pp. 131–142, Jan. 1995.

[38] G. Wang, G.-W. Pan, and B. K. Gilbert, "A hybrid wavelet expansions and boundary element analysis for multiconductor transmission lines in multilayered dielectric media," *IEEE Trans. Microwave Theory Tech.*, vol. MTT–43, pp. 664–675, March 1995.

[39] K. F. Sabet and L. P. B. Katehi, "Characterization of microstrip patch antennas based on the two-dimensional wavelet theory," *IEEE Antennas and Propagation International Symposium*, vol. 1, pp. 316–319, Jan. 1995.

[40] Y. Ojiro and K. Hirasawa, "Moment method analysis of a loop array using wavelet expansions," *IEEE Antennas and Propagation International Symposium*, vol. 5, pp. 1744–1747, Jan. 1998.

[41] R. L. Wagner and W. C. Chew, "A study of wavelets for the solution of electromagnetic integral equations," *IEEE Trans. Antennas and Propagation*, vol. 43, no. 8, pp. 802–810, Aug. 1995.

[42] H. Deng and H. Ling, "Fast solution of electromagnetic integral equations using adaptive wavelet packet transform," *IEEE Trans. Antennas and Propagation*, vol. 47, no. 4, pp. 674–682, Apr. 1999.

[43] Z. Baharav and Y. Leviatan "Wavelets in electromagnetics: the impedance matrix compression (IMC) method," *International journal of numerical modeling: electronic networks, devices and fields*, vol. 11, pp. 69–84, 1998.

[44] G. Oberschmidt, C. Metz, and A. F. Jacob, "Efficient simulation of microstirp circuit using adapted wavelets," *IEE Proc. Microwave Antennas Propag.*, vol. 145, no. 4, pp. 354–360, Aug. 1998.

[45] J. C. Goswami, A. K. Chan and C. K. Chui, "On solving first-kind integral equations using wavelets on a bounded interval," *IEEE Trans. Antennas and Propagation*, vol. 43, no. 6, pp. 614–622, June 1995.

[46] I. Daubechies, *Ten Lectures on Wavelets* (CBMS-NSF series in Applied Maths #61). Philadelphia: SIAM, 1992.

[47] C. K. Chui, *An Introduction to Wavelets*, Boston: Academic, 1992.

[48] A. Gibbons and P. Spirakis, "Lectures on parallel computation," *Cambridge International Series on Parallel Computation: 4*, Cambridge: Cambridge University Press, 1993.

[49] K. Hwang, *Advanced computer architecture*, New York: McGraw-Hill, Inc., 1993.

[50] D. E. Culler and J. P. Singh, *Parallel computer architecture*, San Francisco: Morgan Kaufmann Publishers, Inc., 1999.

[51] P. Messina and A. Murli, *Practical parallel computing: status and prospects*, New York: John Wiley & Sons, Inc., 1991.

[52] T. Hey and J. Ferrante, *Portability and performance for parallel processing*, New York: John Wiley & Sons, Inc., 1994.

[53] P. S. Pacheco, *A user's guide to MPI*, Department of Mathmatics, University of San Francisco, CA, 1994.

[54] Message passing interface forum, MPI: A message-passing interface standard, *International Journal of Supercomputer Applications*, vol. 8, 1994.

[55] IBM parallel enviroment for AIX: MPI programming and subroutine reference version 2, release 1, Poughkeepsie: IBM Corporation, 1995.

[56] *MPI-2 Journal of development*, Knoxville: University of Tennessee, 1997.

[57] W. Gropp et al., *MPI-the complete reference*, Cambridge: The MIT Press, 1997.

[58] NPACI Scalable Parallel Processing (SPP) system resources, NPACI.

[59] NPACI Blue horizon User Guide, NPACI, June 15, 2000.

[60] Using the NPACI IBM SPs, NPACI, May 31, 2000.

[61] Using Hewlett-Packard V2500, *CACR (Center for advance computing research) computing resources*, Pasadena: California Institute of Technology, CA.

[62] E. L. Leiss, *Parallel and vector computing: A practical introduction*, New York: McGraw-Hill, Inc., 1995.

[63] News about NPACI and SDSC community, *NPACI & SDSC Online*, vol. 4, issue 12, June 14, 2000.

[64] D. M. Davidson et al.,"Galactic MPIRE: flying through the digital galaxy," *SDSC Envision*, vol. 15, no. 4, Oct.-Dec., 1999.

[65] R. Cypher and J. L. C. Sanz, *The SIMD model of parallel computation*, New York: Springer-Verlag, 1994.

[66] R. Barrett et al., *Templates for the Solution of Linear Systems: Building Blocks for Iterative Methods*, Philadelphia: SIAM, 1994.

[67] J. JáJá, *An introduction to parallel algorithms*, Reading: Addison-Wesley Publishing Company, MA, 1992.

[68] P. M. Pardalos, A. T. Phillips, and J. B. Rosen, "Topics in parallel computing in mathmetical programming," *Applied Discrete Mathematics and Theoretical Computer Science*, New York: Science Press, vol. 2, 1994.

[69] P. L. Sullivan and D. H. Schaubert, "Analysis of an aperture coupled microstrip antenna," *IEEE trans. Antennas and Propagat.*, vol. 34, no. 8, pp. 977–984, Aug. 1986.

[70] D. M. Pozar, "Microstrip antenna aperture-coupled to a microstrip," *Electronics Letters*, vol. 21, no. 2, pp. 49–50, Jan. 1985.

[71] D. M. Pozar, *Microwave engineering*, New York: Wiley, 1998.

[72] D. M. Pozar, "Input impedance and mutual coupling of rectangular microstrip antennas," *IEEE Trans. Antennas and Propagation*, vol. 30, no. 6, pp. 1191–1196, Nov. 1982.